CHARACTERIZING THE RELATIONSHIP BETWEEN KU-BAND RADAR BACKSCATTER AND SNOW ACCUMULATION ON THE GREENLAND ICE SHEET

by

Julie Miller

A thesis submitted to the faculty of
The University of Utah
in partial fulfillment of the requirements for the degree of

Master of Science

Department of Geography

The University of Utah

December 2012

The University of Utah Graduate School

STATEMENT OF THESIS APPROVAL

The thesis of **Julie Miller**

has been approved by the following supervisory committee members:

Richard R. Forster	, Chair	**May 10, 2012** Date Approved
Philip E. Dennison	, Member	**May 10, 2012** Date Approved
Mitchell J. Power	, Member	**May 10, 2012** Date Approved

and by **George F. Hepner** , Chair of

the Department of **Geography**

and by Charles A. Wight, Dean of The Graduate School.

ABSTRACT

Recent accelerated mass loss offset by increased Arctic precipitation highlights the importance of a comprehensive understanding of the mechanisms controlling mass balance on the Greenland ice sheet. Knowledge of the spatiotemporal variability of snow accumulation is critical to accurately quantify mass balance, yet, considerable uncertainty remains in current snow accumulation estimates. Previous studies have shown the potential for large-scale retrievals of snow accumulation rates in regions that experience seasonal melt-refreeze metamorphosis using active microwave remote sensing. Theoretical backscatter models used in these studies to validate the hypothesis that observed decreasing freezing season backscatter signatures are linked to snow accumulation rates suggest the relationship is inverse and linear (dB). The net backscatter measurement is dominated by a Mie scattering response from the underlying ice-facie. Two-way attenuation resulting from a Raleigh scattering response within the overlying layer of snow accumulation forces a decrease in the backscatter measurement over time with increased snow accumulation rates.

Backscatter measurements acquired from NASA's Ku-band SeaWinds scatterometer on the QuikSCAT satellite together with spatially calibrated snow accumulation rates acquired from the Polar MM5 mesoscale climate model are used to evaluate this relationship. Regions that experienced seasonal melt-refreeze metamorphosis and potentially formed dominant scattering layers are delineated,

freeze-up and melt-onset dates identifying the freezing season are detected on a pixel-by-pixel basis, freezing season backscatter time series are linearly regressed, and a microwave snow accumulation metric is retrieved. A simple empirical relationship between the retrieved microwave snow accumulation metric (dB), σ°_{fs}, and spatially calibrated Polar MM5 snow accumulation rates (m w. e.), C, is derived with a negative correlation coefficient of R=-.82 and a least squares linear fit equation of $C = 0.03 - 0.85\Delta\sigma^{\circ}_{fs}$. Results indicate that an inverse relationship exists between decreasing freezing season backscatter decreases and snow accumulation rates; however, this technique fails to retrieve accurate snow accumulation estimates. An alternate geometric relationship is suggested between decreasing freezing season backscatter signatures, snow accumulation rates, and snowpack stratigraphy in the underlying ice-facie, which significantly influences the microwave scattering mechanism. To understand this complex relationship, additional research is required.

This thesis is dedicated to ~Mom, ~M. Taddie, ~Kaz and ~Boy

TABLE OF CONTENTS

LIST OF FIGURES

ACKNOWLEDGEMENTS

This research would not have been possible without the support of the following individuals. First, I would like to thank my advisor Dr. Rick Forster for his support and guidance. A sincere thanks to Dr. David Long who took the time to answer every question I asked, in detail. Our many discussions on microwave radar and polar ice helped me begin to understand this subject. I would like to thank Dr. Mark Drinkwater for his critical review that provided me with insight into the relationship between radar backscatter and snow accumulation and helped shape the research direction of my dissertation. Thanks to Dr. Jason Box for providing the spatially calibrated Polar MM5 data, IDL mapping code, and an occasional comment that made me laugh. Finally, I'd like to thank Dr. Mitch Power, Dr. Simon Brewer, Dr. Kathleen Nicoll, and Dr. Phil Dennison.

Enhanced Resolution QuikSCAT data were acquired from the NASA-sponsored Scatterometer Climate Record Pathfinder (http://www.scp.byu.edu/) at Brigham Young University courtesy of Dr. David Long. Additional QuikSCAT data used in this research were acquired courtesy of Dr. Kyle McDonald at JPL.

CHAPTER 1

INTRODUCTION

1.1 Snow Accumulation on the Greenland Ice Sheet

Greenland is the largest island on Earth (Figure 1). The majority of its land surface is covered by a deep, dome-shaped layer of snow and glacial ice that exceeds 3000 meters on the interior of the island. The total freshwater content of the Greenland ice sheet is substantial, with a total ice-covered area of 1.73×10^6 kilometers^2 and a total volume estimated to be 2.89×10^6 kilometers^3, equivalent to a sea level rise of 7.3 meters [*Intergovernmental Panel on Climate Change*, 2007]. The topography is characterized by steep elevation gradients at the margins rising to two separate summits, one located in central Greenland at an elevation of 3208 meters, and the second located in southern Greenland at an elevation of 2800 meters. More than half of Greenland exceeds 2000 meters, which results in a high-elevation, relatively flat surface with mountains only visible along the periphery of the ice sheet.

The high-elevation interior acts as a topographic barrier for synoptic scale atmospheric circulations occurring in the high-latitude Arctic region, influencing the genesis and intensification of cyclones that produce precipitation and control snow

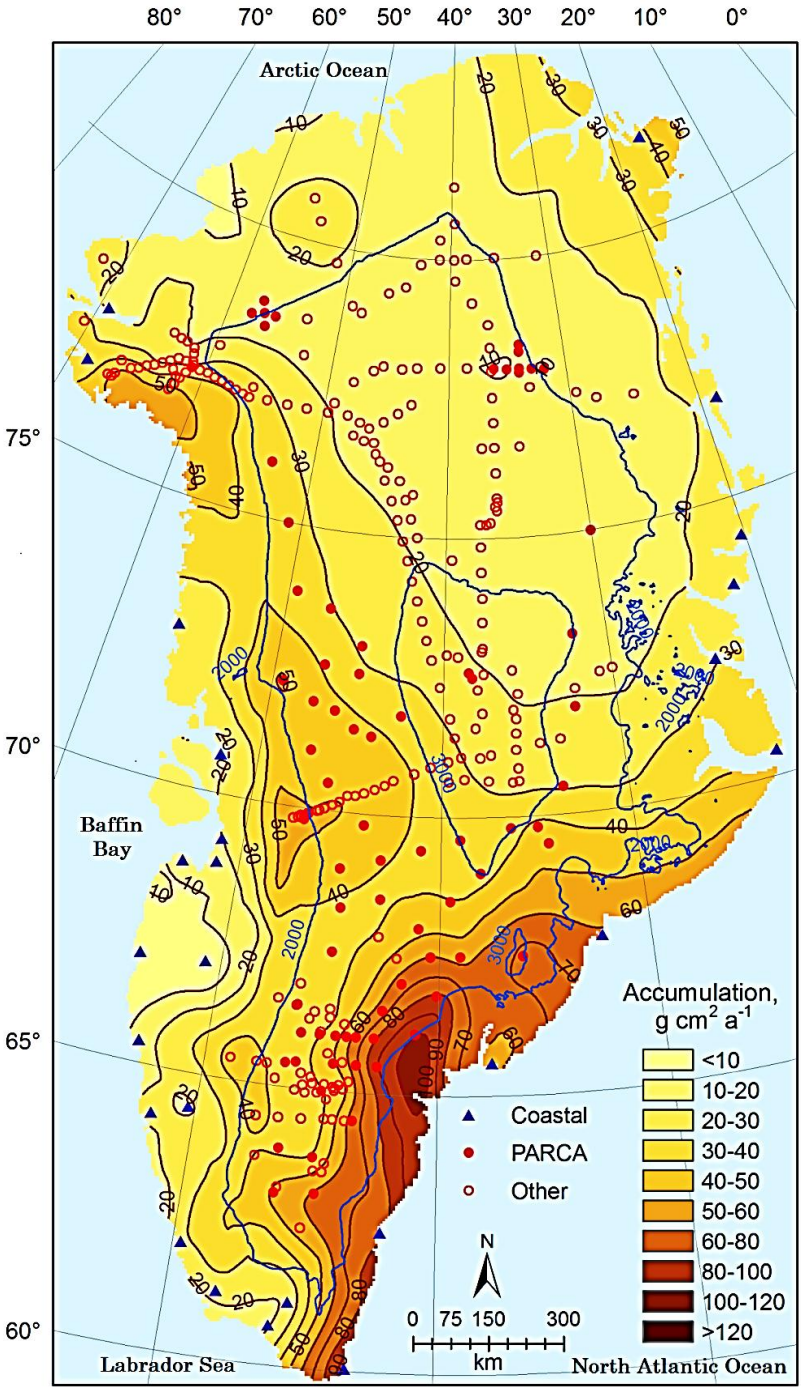

Figure 1. Snow Accumulation Rates Derived from Krigging Ice Cores
Climatological snow accumulation rates estimated by kriging in situ point measurements of snow accumulation rates (1950-2000) derived from 295 ice cores (PARCA and others) and 20 coastal meteorological stations. Elevation contours are shown at 2000 meters and 3000 meters.[*Bales et al.*, 2009]

accumulation patterns on the surface of the Greenland ice sheet [*Kristjánsson et al.*, 2009; *Moore and Renfrew*, 2005; *Serreze*, 1995; *Tsukernik et al.*, 2007]. The major weather system producing precipitation is the frontal cyclone [*Chen et al.*, 1997; *Schuenemann et al.*, 2009] and precipitation often forms as the result of interactions between cyclonic forcing, onshore flow, and topography [*Schuenemann et al.*, 2009]. Interannual spatiotemporal variability of precipitation rates, and the resulting interannual spatiotemporal variability of snow accumulation rates, is related to the position, frequency, and intensity of the storm track [*Chen et al.*, 1997].

Dominant cyclonic storm tracks producing precipitation over the Greenland ice sheet include: 1) cyclones approaching from the west via the Arctic Ocean (Figure 1) that are blocked by the high-elevation interior persist and sometimes intensify, then dissipate in Baffin Bay (Figure 1) and produce precipitation over the western half of Greenland; 2) cyclones approaching from the south or southwest via the Labrador Sea (Figure 1) that interact with the high-elevation southern tip of Greenland and produce heavy precipitation over much of the ice sheet with the highest amounts falling in the southern region; and 3) cyclones approaching from the south via the North Atlantic Ocean (Figure 1), near the Icelandic Low that forms between southern Greenland and Iceland, that do not interact with the ice sheet and produce significantly reduced precipitation [*Chen et al.,* 1997; *Schuenemann et al.,* 2009]. Winter season precipitation, the focus of this thesis, is produced as the result of south or southwest approaching cyclones associated with the North Atlantic storm track [*Schuenemann et al.,* 2009].

Large-scale snow accumulation maps [*Bales et al.*, 2001b; *Bales et al.*, 2009; *Burgess et al.*, 2010; *Ohmura and Reeh*, 1991] indicate maximum precipitation rates in the lower elevations of southeastern Greenland, moderate precipitation rates in

the higher elevations of southeastern and southwestern Greenland, and low precipitation rates in north and northeastern Greenland along the southwestern coast near Baffin Bay. Climatological snow accumulation rates estimated by *Bales et al.* [2009] are illustrated in Figure 1 The average snow accumulation rate over the Greenland ice sheet has been estimated to be ~339 mm w. eq. or 594 gigatons of mass input [*Burgess et al.*, 2010].

Using data from three atmosphere ocean global circulation models (CCCMA-CGCM3.1(T63)[1], MIROC3.2(hires)[2], and MPIECHAM5)[3] used in the Inter-governmental Panel on Climate Change (IPCC) Fourth Assessment Report [*Intergovernmental Panel on Climate Change*, 2007], *Schuenemann and Cassano* [2010] predict a northward shift in the North Atlantic storm track. This shift is expected to change synoptic scale atmospheric circulations in the high-latitude Arctic region as well as increase the frequency of cyclones delivering precipitation to the surface, resulting in a change in snow accumulation patterns on the Greenland ice sheet throughout the twenty first century.

Schuenemann and Cassano [2010] also predict precipitation increases of ~27%, influenced by increases in temperature resulting in an increased amount of precipitable water in the atmosphere, an increase in sea surface temperatures, and a decrease in Arctic sea ice. Less precipitation is expected to be produced dynamically along the southeast coast of Greenland, but an increase in precipitation is expected over the remainder of the ice sheet with the largest increases over the southwest coast of Greenland and in the eastern region.

---

[1] Canadian Centre for Climate Modeling and Analysis Coupled Global Climate Model
[2] Model for Interdisciplinary Research on Climate
[3] atmospheric general circulation model, developed at the Max Planck Institute for Meteorology

Simulations by *Hakuba et al.* [2012], using data from the global atmospheric model ECHAM5-HAM[4], also predict increases in precipitation and snow accumulation rates on the Greenland ice sheet. This study suggests increases in precipitation results from decreases in topography. Analysis of changes in synoptic scale circulation patterns indicates that flatter topographies allow synoptic scale atmospheric circulations to penetrate further into the accumulation zone[5] of the high -elevation interior, resulting in precipitation in regions where snow accumulation rates are currently minimal. Increases in mass input in the accumulation zone of the high-elevation interior by snow accumulation may potentially create a negative feedback, stabilizing the height of the Greenland ice sheet.

Hakuba et al. [2012] also suggest feedback processes between Greenland's topography, synoptic scale atmospheric circulations, and precipitation and postulate snow accumulation may play a significant role for the evolution of the mass balance of the Greenland ice sheet.

1.2 Snow Accumulation and Mass Balance

Ice sheet mass balance is defined annually by differencing mass input by snow accumulation at the surface and mass loss by ablation resulting from melt water runoff and ice discharge at the periphery [*Cuffey and Paterson*, 2010]. Recent studies indicate that over the past few decades, the net mass balance of the Greenland ice sheet has become increasingly negative [*Intergovernmental Panel on Climate Change*, 2007; *Velicogna*, 2009] and current mass loss trends have been

[4] aerosol climate modeling system
[5] the region where mass input from snow accumulation exceeds mass loss from ablation

significantly influenced by spatiotemporal variability of snow accumulation rates [*Rignot et al.*, 2011; *Sasgen et al.*, 2012].

A study by *van den Broeke et al.* [2009] calculated the net mass balance of the Greenland ice sheet using the mass budget method[6] and validated these calculations using satellite gravity observations from NASA's Gravity Recovery and Climate Experiment (GRACE) satellites[7]. Conclusions of this study indicate that over the time period 2000–2008, mass loss from the Greenland ice sheet was equally divided between mass loss at the surface (i.e., snow accumulation minus surface melting) and mass loss by ice discharge at the periphery. A net mass loss of ~1500 gigatons was estimated, equivalent to an average rate of 0.46 millimeters per year of global sea level rise. Extensive surface melting accelerated the observed mass loss rate after 2006, and the average mass loss rate increased to 0.75 millimeters per year of global seas level rise.

van den Broeke et al. [2009] also concluded that without the moderating effects of increased precipitation and refreezing of melt water within the firn layer of the lower elevations of the accumulation zone, mass loss would have been 100% higher than actually observed.

Mass input has increased in the accumulation zone of the high-elevation interior of the ice sheet as the result of increased snow accumulation rates [*Krabill et al.*, 2000; *Thomas et al.*, 2006; *Zwally et al.*, 2005; *Zwally et al.*, 2011]. Mass loss has also increased in the lower elevations of the ablation zone[8] as the result of extensive surface melting [*Bhattacharya et al.*, 2009; *Box et al.*, 2006] and the

[6] quantifies individual components of ice sheet mass balance, surface mass balance, and ice discharge
[7] twin satellites which make detailed measurements of Earth's gravity field
[8] the region where mass loss from ablation exceeds mass input from snow accumulation

acceleration of outlet glaciers [*Howat et al.*, 2007; *Rignot and Kanagaratnam*, 2006] which results in dynamic thinning [9] at the periphery of the ice sheet [*Pritchard et al.*, 2009].

Zwally et al. [2011] compared mass changes observed from 2003-2007 from NASA's Ice, Cloud and land Elevation Satellite (ICESat) laser altimetry[10], 1992-2002 ESA's European Remote Sensing Satellite (ERS) radar altimeter[11], and airborne laser altimetry, and found that from 1992-2002, the accumulation zone of the high-elevation interior experienced mass gain. However, over the time period 2003-2007, the mass gain above 2000 meters elevation decreased. This study suggests that increased surface melting and strong dynamic thinning initiated at the lower elevations of the ablation zone propagates rapidly into the accumulation zone of the high-elevation interior of the Greenland ice sheet.

Perturbation experiments by *Wang et al.* [2012] using an Anisotropic Ice Flow model (AIF)[12] agree with observations by Zwally et al. [2011] and predict that if mass loss at the lower elevations of the ablation zone ceased, the accumulation zone of the high-elevation interior would continue thinning for 300 years and would take thousands of years for full dynamic recovery.

Mass loss resulting from dynamic thinning is so poorly understood on the scale of an ice sheet that its potential contribution to sea level rise over the twenty first century remains a source of considerable uncertainty [*Bindoff et al.*, 2007].

---

[9] mass loss resulting from accelerated ice sheet flow
[10] mission for measuring ice sheet mass balance
[11] single-frequency nadir pointing radar altimeter operating at Ku band
[12] ice sheet flow model developed for anisotropic ice based on the shallow ice approximation

Understanding the processes by which mass loss is offset by mass input is of critical importance to understanding the future mass balance of the Greenland ice sheet.

1.3 Estimating Snow Accumulation Rates

Many of the uncertainties in the mass balance of the Greenland ice sheet are derived from the relative uncertainty in current snow accumulation estimates. Previous studies estimated the uncertainty in snow accumulation rates on the Greenland ice sheet at ~20-25% [*Bales et al.*, 2001a]. A recent study by *Burgess et al.* [2010] estimate uncertainty in snow accumulation rates at ~22%, with the highest uncertainty in snow accumulation rates (33% of the total 22% uncertainty) in the southeast region of the Greenland ice sheet. Uncertainty results from steep topographic gradients moving from the periphery of the ice sheet inland, which significantly influence precipitation patterns in this region [*Bales et al.*, 2009]. High snow accumulation rates in the southeast region are of sufficient magnitude to change the net mass balance during some years and dominate interannual variability in Greenland ice sheet total mass input [*Burgess et al.*, 2010].

Uncertainty in annual snow accumulation rates across the Greenland ice sheet propagates through to mass budget-based mass balance estimates and impacts interpretation of repeat-altimetry-based mass balance estimates.

1.3.1 In Situ Point Measurements of Snow Accumulation

Snow accumulation, the single mass input term in the mass balance equation, is defined as the sum of solid precipitation and retained liquid precipitation minus surface water vapor flux and blowing snow sublimation [*Box et al.* [2006]. Traditionally, to estimate snow accumulation rates on a small-scale, in

situ point measurements are used. Examples of in situ point measurements include snow accumulation estimates from snow pits acquired during early traverses by Koch-Wegener [*Koch and Wegener*, 1930], by Langway [*Langway*, 1961], by the U.S. Army Snow Ice and Permafrost Research Establishment (SIPRE) Project [*Benson*, 1962], and as part of NASA's ongoing Program for Regional Climate Assessment (PARCA), from deep ice cores acquired as part of the Greenland ice sheet Program (GISP, GISP2), from recent shallower depth firn cores acquired during the 2010 and 2011 Arctic Circle Traverse (ACT), and from automated weather stations (AWS) within the Greenland Climate Network (GC-Net) [*Steffen and Box*, 2001] and coastal meteorological stations. A detailed description of recent and historical in situ point measurements of snow accumulation rates is given in both *Ohmura and Reeh* [1991] and *Bales et al.* [2001a].

Uncertainty can be introduced into snow accumulation estimates in several ways. The first way uncertainty can be introduced into snow accumulation estimates results from differences in geophysical conditions on the ice sheet, which has been shown to impact the interpretation of spatiotemporal variability in snow accumulation rates acquired from firn and ice cores on a scale as small as a few tens of meters. A study by *Mosley-Thompson et al.* [2001] indicates that two distinct signals are contained in an in situ point measurement: 1) a climate signal resulting from atmospheric conditions (i.e., snow accumulation), and 2) glaciological noise resulting from surface undulations, which may be influenced by wind transport and the redeposition of snow (i.e., small-scale surface variations such as satrugi or large-scale variations such as dunes).

Using shallow and intermediate depth PARCA cores to assess annual spatiotemporal variability of snow accumulation rates on the Greenland ice sheet,

Mosley-Thompson et al. [2001] showed that the spatiotemporal variability of climate signals between multiple closely space cores are partially masked by glaciological noise. To separate the climate signal from glaciological noise and obtain a relatively accurate estimate of snow accumulation rates, *Mosley-Thompson et al.* [2001] suggest multiple cores must be acquired and then averaged, both spatially in the region of the drilled cores, and temporally over the length of the core time series. Most in situ point measurements, both recent and historical, are derived from single cores which can result in errors in snow accumulation rates. Further uncertainty can be introduced when estimating snow accumulation on a large-scale, when different methods are used on different cores to extract snow accumulation rates.

Given the difficulty of field work in the harsh Arctic environment, the second way uncertainty can be introduced into snow accumulation estimates results from the sparsity of in situ measurements. Spatially, in situ point measurements of snow accumulation rates have nonuniform spatial distributions, are often concentrated along linear traverses, and are generally located above 2000 meters in the accumulation zone of the high-elevation interior (Figure 1). Temporally, in situ point measurements of snow accumulation are taken at inconsistent time intervals. When estimating snow accumulation on a large-scale, error in both space and time can occur in underrepresented regions

1.3.2 Large-Scale Snow Accumulation Maps

Several methods have been used to construct large-scale mappings of snow accumulation rates on the Greenland ice sheet, each with their associated strengths and weaknesses. Initial climatological mappings used in situ point measurements of snow accumulation rates (e.g., near-surface measurements, snow pits, firn and ice

cores, coastal meteorological stations) and simple interpolation techniques to estimate the spatial variability of snow accumulation rates over a larger spatial grid [*Bales et al.*, 2001b; *Benson*, 1962; *Ohmura and Reeh*, 1991]. Subsequent climatological mappings incorporated updated in situ point measurements in these interpolations [*Ohmura et al.*, 1999], and used kriging techniques (Figure 1) [*Bales et al.*, 2001a; *Bales et al.*, 2009], as well as more advanced interpolation techniques [*Calanca et al.*, 2000; *Cogley*, 2004; *Van Der Veen et al.*, 2001]. The resulting large-scale climatological mappings of snow accumulation rates on the Greenland ice sheet are linked to in situ measurements; however, climatological mappings are limited by the original uncertainty estimates in the point data.

The spatiotemporal variability of snow accumulation rates on the Greenland Ice Sheet has also been mapped using global climate models [*Murphy et al.*, 2002; *Ohmura et al.*, 1996; *Thompson and Pollard*, 1997], as well as higher spatial resolution regional climate models [*Box et al.*, 2005; *Box et al.*, 2004; *Box et al.*, 2006]. In contrast to climatological mappings derived using interpolation techniques, snow accumulation rates derived using climate models are uniform in both in space and time; however, climate models are not linked to in situ measurements and do not capture subgrid spatial variability in snow accumulation rates resulting from surface undulations or steep topographic gradients.

The most recent technique is a hybrid of the two previously described methods. *Burgess et al.* [2010] spatially calibrated solid precipitation output (i.e., snowfall) acquired from the Fifth Generation Mesoscale Model modified for polar climates (Polar MM5) [*Bromwich et al.*, 2001; *Cassano et al.*, 2001]. The spatial calibration uses in situ point measurements of snow accumulation rates acquired from firn cores and coastal meteorological stations and is calibrated using spatial

interpolation of regionally derived linear correction functions. The resulting large-scale mapping of snow accumulation rates on the Greenland ice sheet is linked to in situ measurements and uniform in space and time; however, the calibration factors are still limited by the original uncertainty estimates in the point data. The locations of the in situ point measurements used to derive the spatial calibration and spatially calibrated Polar MM5 snow accumulation estimates by *Burgess et al.* [2010] are illustrated in Figure 2 and Figure 3, respectively.

1.4 Snow Accumulation and Active Microwave Remote Sensing

Previous studies have shown the potential for estimating snow accumulation rates on the Greenland ice sheet using active microwave remote sensing. In contrast to a climatological map or a climate model, a snow accumulation estimate derived from active microwave remote sensing represents an integrated average of in situ backscatter measurements over the area on the surface of the Earth illuminated by the antenna. This results in a potential snow accumulation estimate that can be linked to in situ measurements of snow accumulation rates that are relatively uniform in space and time, and captures the spatial variability of snow accumulation rates resulting from surface undulations or steep topographic gradients at the spatial resolution observed by the microwave instrument.

The relationship between radar backscatter and snow accumulation rates is complex, and currently not well-understood. Research has been limited to a few studies, with the majority focused on the high-elevation interior of the dry snow zone. Using the passive microwave cross polarized ratio technique (XGPR) [*Abdalati and Steffen,* 1995, 2001]. *Steffen et al.* [2004] calculated a 1979 – 2003 average dry snow zone spatial extent of ~1.28 kilometers^2, equivalent to ~74% of the total ice

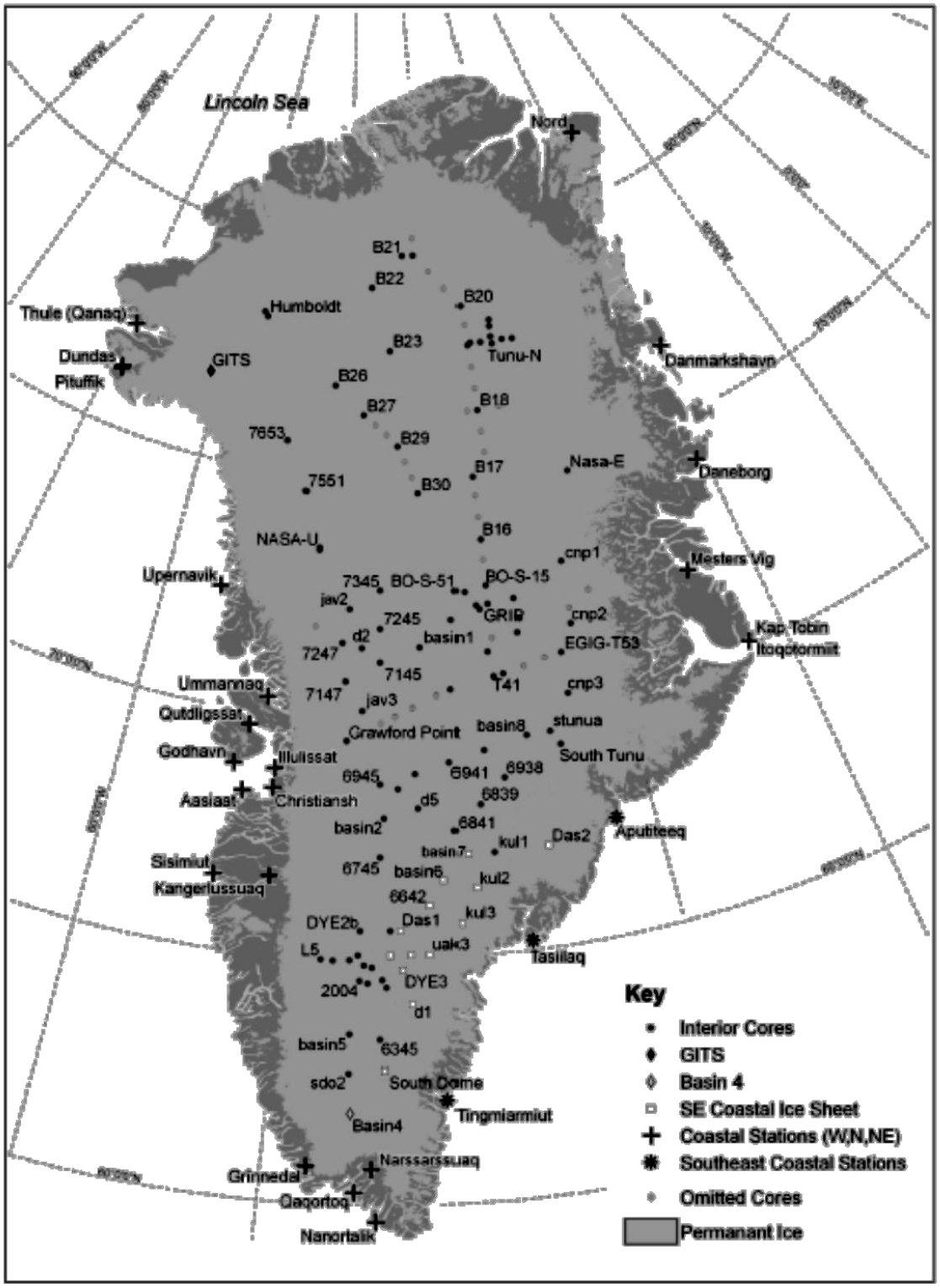

Figure 2. In Situ Point Measurements Used in Spatial Calibration
Locations of 105 cores and 28 coastal meteorological stations used in the Polar MM5 spatial calibration procedure. [*Burgess et al.*, 2010]

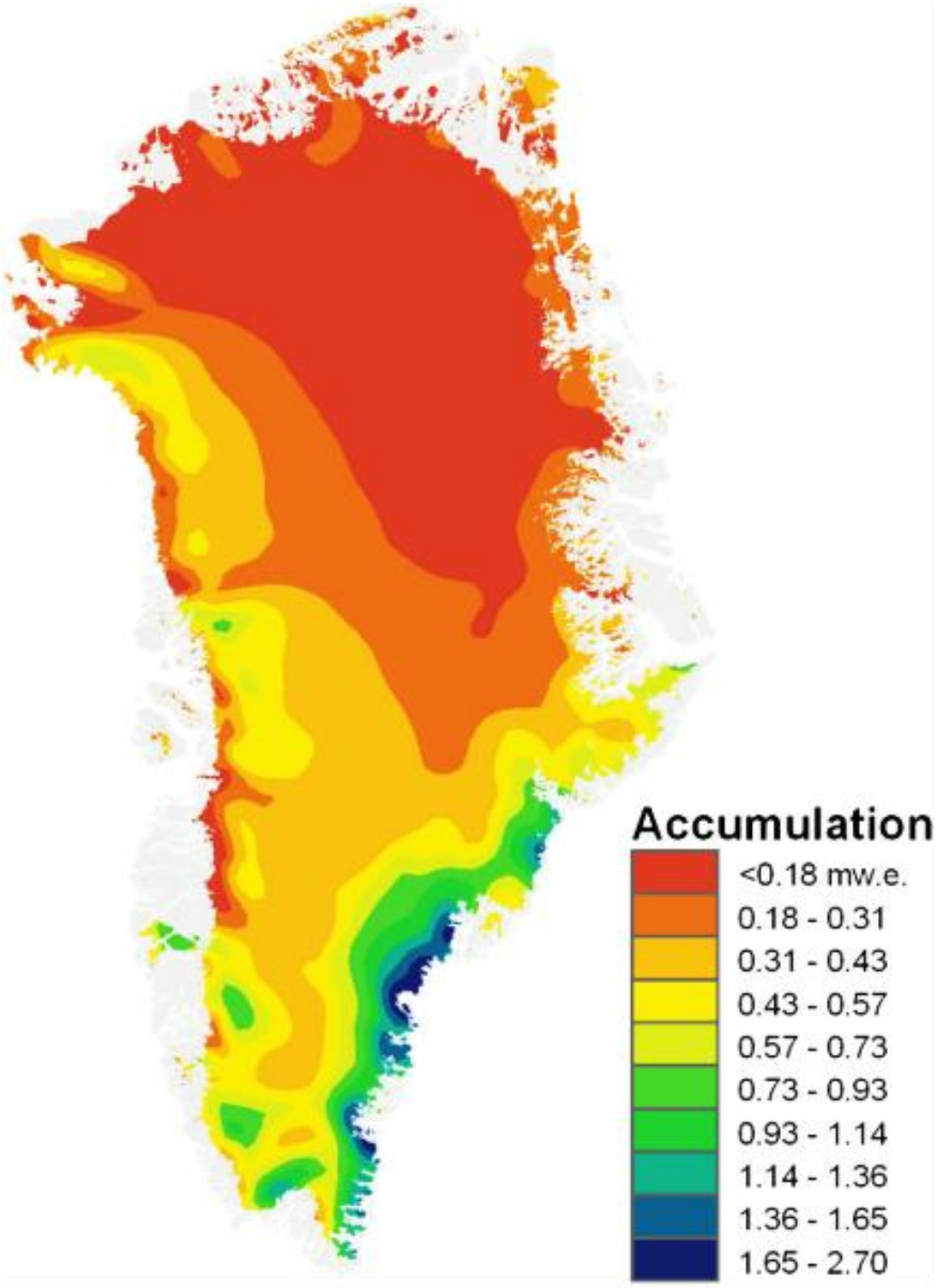

Figure 3. Spatially Calibrated Polar MM5 Snow Accumulation Rates
Climatological snow accumulation rates estimated by spatially calibrating snow accumulation data from the Polar MM5 using in situ measurements of snow accumulation rates (1958-2009) derived from 105 ice cores and 28 coastal meteorological stations (Figure 2). [*Burgess et al.*, 2010]

covered area. By definition [*Benson* 1962], this region experiences negligible seasonal surface melting and low annual snow accumulation rates (Figure 1 and Figure 3). Snowpack stratigraphy in the dry snow zone is characterized by a sequence of annual layers of snow accumulation with thicknesses proportional to snow accumulation rates.

The remaining ~26% of the Greenland ice sheet experiences seasonal melt-refreeze metamorphosis, which forms dominant scattering layers consisting of large ice-scatterers (e.g., ice layers, pipes, glands, and lenses) embedded at differing depths within a sequence of annual layers of snow accumulation. Annual snow accumulation rates in this region are variable across the ice sheet and generally increase moving from north to south as well as descending downglacier from higher elevations towards the lower elevations of the ice sheet periphery (Figure 1 and Figure 3).

The spatial extent of surface melting in some years can significantly increase, shifting the boundary between these two regions upglacier into the high-elevation interior, which decreases the spatial extent of the dry snow zone and increases the spatial extent of regions that experience seasonal melt-refreeze metamorphosis. Recent notable upglacier boundary shifts occurred during the 2002 melt season when the 1973-2003 average spatial extent of surface melting increased from 455,000 kilometers^2 to 690,000 kilometers^2, equivalent to a 65% increase [*Steffen et al.,* 2004] and during the 2012 melt season when 98.6% of the ice sheet experienced surface melting [*Nghiem et al.,* 2012].

Retrieval algorithms to estimate snow accumulation rates in the dry snow zone and in regions that experience seasonal melt-refreeze metamorphosis are based on both theoretical models and empirical relationships derived from comparisons

between backscatter signatures and in situ measurements of snow accumulation rates.

In the dry snow zone, retrieval algorithms are based on the inverse relationship between radar backscatter and snow accumulation rates, which is influenced by snow grain size. In general, larger snow grains develop when snow accumulation rates are low, resulting in relatively high backscatter measurements and smaller snow grains develop when snow accumulation rates are high, resulting in relatively low backscatter measurements.

In regions that experience seasonal melt-refreeze metamorphosis, retrieval algorithms are based on the inverse relationship between radar backscatter and snow accumulation rates, which is influenced by underlying dominant scattering layers within the snowpack. A layer of accumulating snow overlying a dominant scattering layer decreases backscatter measurements over time. In general, the rate of decrease is dependent on both snow accumulation rates and on the density of large ice-scatterers within the dominant scattering layer. High snow accumulation rates and a low density dominant scattering layer results in a relatively large backscatter decrease over time and low accumulation rates and a high density dominant scattering layer results in a relatively small backscatter decrease over time. Both relationships are inverse; however, each retrieval algorithm is based on a different physical microwave scattering mechanism.

1.5 Literature Review

Long and Drinkwater [1994] first observed the inverse relationship between Ku-band backscatter measurements acquired from NASA's first satellite-borne scatterometer aboard the Seasat-A Satellite (SASS) and snow accumulation rates

across a southwest transect of the dry snow zone of the Greenland ice sheet. *Jezek and Gogenini* [1992] observed a similar relationship in comparisons between Ku-band backscatter measurements acquired from SASS and C-band backscatter measurements acquired from ESA's SAR aboard the European Remote Sensing Satellite (ERS-1).

The inverse relationship between radar backscatter and snow accumulation rates in the dry snow zone has been investigated in further detail using both SAR and scatterometry. Differences between large-scale mappings of backscatter measurements over the Greenland ice sheet acquired from SAR and scatterometry are related to the satellite's orbital geometry and the associated radar's antenna scanning pattern and spatial response, which results in different spatial and temporal resolutions. The relatively narrow swath width of a typical SAR antenna (~100 kilometers) requires mosaicing of swaths acquired over several weeks from multiple orbital passes to compile a complete, relatively high spatial resolution (~26 meters) image mapping of backscatter measurements over the Greenland ice sheet. Studies using SAR generally use a single mosaicked image or an image pair (interferometric synthetic aperture radar (InSAR[13])) for analysis.

Typical scatterometer antennas have relatively wide swath widths (~500-1800 kilometers), which provides complete spatial coverage of the Greenland ice sheet as frequently as twice daily. Combining backscatter measurements from multiple scatterometers with overlapping orbital passes and operating at a similar frequency and polarization can increase temporal resolution [*Hicks and Long,* 2011]

---

[13] technique to generate maps of surface deformation or elevation change using differences in the phase of the electromagnetic waves returning to the satellite

(e.g., NASA's Ku-band SeaWinds scatterometer on the QuikSCAT satellite (QuikSCAT) and NASDA's Ku-Band SeaWinds scatterometer on the ADEOS-II satellite (SeaWinds) or EUMETSAT's C-band advanced scatterometer (ASCAT) on the MetOp-A and MetOp-B satellites (ASCAT-A and ASCAT-B)). The resulting image mapping of backscatter measurements over the Greenland ice sheet has a relatively coarse spatial resolution (~25-50 kilometers). This coarse spatial resolution can be improved using a resolution enhancement algorithm [*Early and Long,* 2001*; Long et al.,* 1993] as discussed in Chapter 2. Studies using scatterometry generally use time series constructed from image data for analysis. The relationships derived between radar backscatter and snow accumulation rates on the Greenland ice sheet from both SAR and scatterometer studies are the same.

Forster et al. [1999] used a coupled snow metamorphosis/backscatter model and backscatter measurements acquired from the ERS-1 SAR mosaic by *Fahnestock et al.* [1993] for analysis of the relationship between radar backscatter and snow accumulation rates in the dry snow zone of the Greenland ice sheet. Results of this study indicate a Raleigh scattering response from snow grains dominates the microwave response at high incidence angles (>30°) and further suggests backscatter measurements have increased sensitivity to changes in snow accumulation rates when the average snow accumulation rate for the region is low. *Forster et al.* [1999] concluded that an inverse relationship exists between radar backscatter and snow accumulation rates and suggests a secondary relationship with mean annual temperature. A subsequent study by *Munk et al.* [2003] extended the work by *Forster et al.* [1999] by generating a lookup table which uniquely maps backscatter measurements and mean annual temperatures to snow accumulation rates in the dry snow zone.

A study by *Drinkwater et al.* [2001a] derived empirical relationships between both backscatter measurements and the change in backscatter measurements with incidence angle and PARCA in situ point measurements of snow accumulation rates in the dry snow zone using C-band backscatter measurements from ESA's ESCAT scatterometer aboard the European Remote Sensing satellite (ERS-2) and Ku-band backscatter measurements from NASA's NSCAT scatterometer aboard the ADEOS-1 satellite. Results suggest that C-band backscatter measurements are more sensitive to snow layering and buried ice-scatterers in the boundary zone between the dry snow zone and regions that experience seasonal melt-refreeze metamorphosis given the longer wavelength and increased penetration depth, which allows for interaction with more annual layers. Ku-band backscatter measurements are more sensitive to volume scattering from recently accumulated snow, given the shorter wavelength which allows for increased interaction with individual snow grains. A slightly stronger exponential relationship is shown between the change in Ku-backscatter with incidence angle and snow accumulation rates, with an increased sensitivity to small changes in snow accumulation rates when the average snow accumulation rate for the region is low. The derived exponential relationship was tested using a coupled snow metamorphosis/backscatter model similar to *Forster et al.* [1999]. *Flach et al.* [2005] extended the work by [*Drinkwater et al.*, 2001a] and developed an inversion technique to retrieve snowpack geophysical near-surface properties (i.e., snow grain size, density, layer thicknesses, and snow accumulation rate) to be used to predict geophysical retracking errors in altimeter data and then estimate the resulting uncertainty in the altimeter elevation measurements from altimetry missions such as ESA's CryoSAT mission.

A study by *Oveisgharan and Zebker* [2007] suggests that because larger snow grain size and deeper annual layers of snow accumulation both increase backscatter measurements, to accurately model snow accumulation rates, a depth hoar must be introduced. *Oveisgharan and Zebker* [2007] introduced the first backscatter model relating both backscatter measurements and InSAR correlation measurements to snow grain size and depth hoar layer spacing to retrieve a snow accumulation rate. The model was tested in a small area of the dry snow zone using SAR data acquired from ERS-2.

The two most relevant studies to this thesis are *Wismann et al.* [1997] and *Nghiem et al.* [2005], which used scatterometer data to retrieve snow accumulation rates in regions of the Greenland ice sheet that experience seasonal melt-refreeze metamorphosis and the creation of dominant scattering layers. *Wismann et al.* [1997] first observed decreasing freezing season backscatter signatures in regions that experience seasonal melt-refreeze metamorphosis and linked this response to snow accumulation. Decreasing freezing season backscatter signatures have also been observed in Antarctica [*Bingham and Drinkwater* 2000*; Scambos et al* 2009*,* Figure S4.]. In the dry snow zone, backscatter signatures are relatively constant with small seasonal variations [*Moon,* 2012]. *Wismann et al.* [1997] used a two layer backscatter model (i.e., accumulating layer of snow overlying a fixed layer of ice-scatterers) and Monte-Carlo simulations to estimate attenuation of the EM wave or the extinction rate (absorption + scattering) of the backscatter measurement as a function of the depth of the accumulated snow layer. This model indicates the relationship between decreasing freezing season backscatter signatures and snow

accumulation rates is inverse and approximately linear in the decibel (dB)[14] domain. Using C-band backscatter measurements from ESCAT on ERS-1/2, the annual decrease in the backscatter measurement was used as a microwave snow accumulation metric and a large-scale mapping of annual snow accumulation rates was constructed. It was then visually compared to *Ohmura and Reeh* [1991] and found to be in general agreement.

Limitations identified by the study include uncertainty in the conversion of the extinction rate of the backscatter measurement to the rate of increasing snow depth and the uncertainty in snow density given the lack of in situ measurements.

The retrieval technique used by *Wismann et al.* [1997] was subsequently adapted by *Nghiem et al.* [2005]. This study derived a linear (dB) backscatter approximation [*Nghiem et al.*, 1990a] that defined decreasing freezing season backscatter signatures as a linear function of the extinction rate of the backscatter measurement and the depth of the accumulating snow layer. An extinction coefficient was derived using in situ snow height recordings from two sonic height instruments at the NASA-SE AWS in the GC-Net. Using Ku-band backscatter measurements from QuikSCAT, the derived backscatter approximation, and the derived extinction coefficient, a snow depth was calculated and used to construct a large-scale mapping of freezing season snow accumulation rates on the Greenland ice sheet.

The coarse temporal sampling of ERS-1/2 scatterometer data used by *Wismann et al.* [1997] resulted in an implicit approximation of snow accumulation

---

[14] logarithmic unit used to measure the ratio of signal power relative to a reference level

rates during the melt season. The relatively frequent temporal sampling of scatterometer data acquired from QuikSCAT requires an alternate approach. *Nghiem et al.* [2005] used fixed freezing season dates as a simple method to separate stable freezing season backscatter signatures from more complex melt season backscatter signatures resulting from the detection of liquid water content within the snowpack. When liquid water content is detected, a snow accumulation estimate is not retrievable using this technique. A limitation identified by *Nghiem et al.* [2005] is the use of fixed freezing season dates which does not provide a complete estimate of freezing season snow accumulation rates given the timing of melt events is variable pixel-by-pixel across the ice sheet. To accurately identify the freezing season in a backscatter time series, freeze-up (i.e., the final refreeze event of the melt season) and melt-onset (i.e., the initial melt event of the following melt season) dates must be detected on a pixel-by-pixel basis, which requires a more sophisticated retrieval algorithm than used by *Nghiem et al.* [2005].

A second limitation of *Nghiem et al.* [2005] is the use of a single extinction coefficient over the entire study region. Spatially, the geophysical near-surface properties of the snowpack are significantly different, influenced by atmospheric conditions, topography, latitude, and elevation. These properties control the microwave scattering mechanisms as well as the depth of penetration and the subsequent extinction of the electromagnetic wave. Thus, it is unlikely that the extinction coefficient remains constant across the entire Greenland ice sheet.

1.6 Thesis Statement and Research Contributions

This thesis characterizes the relationship between Ku-band radar backscatter and snow accumulation rates on the Greenland ice sheet using

backscatter measurements acquired from QuikSCAT together with snow accumulation rates acquired from the Polar MM5 mesoscale climate model [*Box et al.,* 2004*; Box et al.,* 2006*; Bromwich et al.,* 2001*; Cassano et al.,* 2001], spatially calibrated using a calibration technique similar to the procedure outlined in *Burgess et al.* [2010].

The inverse linear relationship between decreasing freezing season σ° signatures and snow accumulation rates in regions that experience seasonal melt-refreeze metamorphosis hypothesized by *Wismann et al.* [1997] and *Nghiem et al.* [2005] is evaluated using the microwave snow accumulation model outlined in Chapter 4. The microwave snow accumulation model is defined using a three step algorithm to retrieve a microwave snow accumulation metric: 1) regions of the Greenland ice sheet that experienced seasonal melt-refreeze metamorphosis and potentially formed dominant scattering layers are annually delineated using a microwave melt model [*Hicks and Long*, 2011], 2) freeze-up and melt-onset dates to identify stable freezing season σ° signatures are detected on a pixel-by-pixel basis using a Markov model derived from the microwave melt model [*Hicks and Long*, 2011], and 3) freezing season backscatter decreases are calculated on a pixel-by-pixel basis to retrieve a microwave snow accumulation metric for comparison with spatially calibrated Polar MM5 snow accumulation rates using a retrieval technique similar to *Wismann et al.* [1997].

A simple empirical relationship between freezing season σ° decreases and spatially calibrated Polar MM5 snow accumulation rates on the Greenland ice sheet is derived and analyzed to determine the potential for large-scale mapping of freezing season snow accumulation rates using this retrieval technique.

An improved understanding of the complex relationship between Ku-band radar backscatter and snow accumulation rates will facilitate in the development of robust retrieval techniques using theoretical and/or empirically derived active microwave snow accumulation models, which may potentially reduce the current uncertainty in both snow accumulation estimates and mass balance calculations on the Greenland ice sheet. Active microwave techniques ideally should be combined with passive microwave techniques to exploit the full potential of satellite-borne microwave instruments. Snow accumulation estimates derived from satellite-borne microwave instruments may be particularly effective where both climatological maps and climate models have considerable limitations, such as regions with high spatial variability in snow accumulation rates resulting from surface undulations or steep topographic gradients.

1.7 Organization

This thesis is organized as follows. Chapter 2 provides background on scatterometry, the backscatter measurement, microwave scattering mechanisms, and penetration depth. Chapter 3 describes the formation of dominant scattering layers in each of the Greenland ice-facies on the Greenland ice sheet. Chapter 4 outlines the microwave snow accumulation model used to retrieve a microwave snow accumulation metric, establishes a simple empirical relationship between the microwave snow accumulation metric and spatially calibrated Polar MM5 snow accumulation rates on the Greenland ice sheet, and then presents a discussion of results, conclusions, and future work.

CHAPTER 2

SCATTEROMETRY

As background information, this chapter discusses fundamental concepts of satellite-borne scatterometry including normalized radar cross-section, the antenna configuration, which determines the spatial and temporal resolution of scatterometer data, and SeaWinds on QuikSCAT from which scatterometer data for this study were acquired. Microwave scattering mechanisms and penetration depth, important to the analysis and discussion sections in Chapter 4, are also discussed.

2.1 Normalized Radar Cross-Section

Scatterometers are microwave radars that transmit pulses of electromagnetic (EM) energy at a given frequency and polarization and then measure the backscattered power received, which allows for estimation of the normalized radar cross section of a target [*Ulaby et al.*, 1982]. Satellite-borne scatterometers were originally designed to measure near-surface winds vectors (speed and direction) over the global oceans under all weather conditions [*Naderi et al.*, 1991; *Vogelzang and Stoffelen*, 2012]; however, they have proven effective tools for investigating the time-varying geophysical near-surface properties of polar ice [*Drinkwater and Lytle*, 1997; *Forster et al.*, 2001; *Hall et al.*, 2009; *Kunz and Long*, 2006; *Scambos et al.*, 2008; *Smith et al.*, 2003; *Stuart and Long*, 2011; *Swan and Long*, 2012]

The fundamental relationship between the characteristics of a microwave radar (e.g., scatterometers, SAR, altimeters), the target, and the received signal is defined by the radar equation [*Ulaby et al.*, 1982]. Normalized radar cross section, or radar backscatter, σ°, is calculated using the radar equation

$$\sigma^\circ = \frac{(4\pi)^3 R^4 L P_r}{P_t G^2 \lambda^2 A} \quad (1)$$

where R is the slant range to the target, P_t is the power transmitted by the radar at a given polarization, P_r is the backscattered power received by the radar at a given polarization, L represents the known losses of the radar, G is the antenna gain, λ is the wavelength of the transmitted EM wave, and A is the effective area of the target illuminated by the propagating EM wave.

Normalized radar cross section is a function of the direction of the transmitted EM wave incident on the target, the direction of the propagating EM wave backscattered towards the receiver, and the orientation, size, shape, and dielectric properties of the target. The direction of the incident and backscattered EM wave is defined by the respective incidence and azimuthal angles relative to north.

As observed by the radar over the area illuminated by the propagating EM wave, termed antenna footprint, the target consists of many point scatterers which can each have different scattering characteristics. The power illuminating different sections of the target may vary and scatterers may be oriented at slightly different directions from the radar as well as have differing sizes, shapes, and dielectric properties. The total power received by the radar is an integrated average of the

power received from each individual point scatterer, within penetration depth, over the antenna footprint of the microwave instrument.

2.2 Antenna Configuration

The empirically derived relationship between σ° measurements and near-surface wind vectors over the global oceans is defined by the geophysical model function which describes the relationship between both the wind and the sea surface geometry, and the interaction between EM energy and the sea [*Naderi et al.*, 1991]. For measurement of near-surface wind vectors, the geophysical model function requires frequent, simultaneous σ° measurements observed at multiple incidence and azimuthal angles [*Naderi et al.*, 1991].

The antenna is the most fundamental concept in satellite-borne scatterometer design. It determines the temporal resolution and viewing geometry (incidence and azimuth angle) of σ° measurements, and the swath width which constrains the spatial resolution. Spatial resolution is of secondary importance to spatial coverage. As a result, σ° measurements acquired from satellite-borne scatterometers are designed for relatively high temporal resolution with near daily coverage of the global oceans, and relatively low spatial resolution as described in Section 1.4. Comparisons between antenna configurations, swath widths, incidence and azimuthal angles, and spatial and temporal resolutions as well as frequencies and polarizations for each of the satellite-borne scatterometer missions are given in Figure 4.

	SASS	ESCAT	NSCAT	SeaWinds	ASCAT	Oscat
FREQUENCY	14.6 GHz	5.3 GHz	13.995 GHz	13.6 GHz	5.3 GHz	13.6 GHz
ANTENNA AZIMUTHS						
POLARIZATIONS	V-H, V-H	V ONLY	V, V-H, V	V-OUTER/H-INNER	V ONLY	V-OUTER/H-INNER
BEAM RESOLUTION	FIXED DOPPLER	RANGE GATE	VARIABLE DOPPLER	PENCIL-BEAM	RANGE GATE	PENCIL-BEAM
SCIENCE MODES	MANY	SAR, WIND	WIND ONLY	WIND/HI-RES	WIND ONLY	WIND/HI-RES
RESOLUTION (s *)	nomally 50 km	50 km	25 km	Egg: 25x35 km Slice: 6x25km	25/50 km	Egg: 30x68 km
SWATH, km	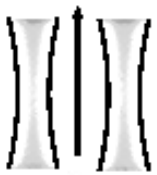					
INCIDENCE ANGLES	0° - 70°	18° - 59°	17° - 60°	46° & 54.4°	25°- 65°	49° & 57°
DAILY COVERAGE	VARIABLE	< 41 %	78 %	92 %	65 %	> 90 %
MISSION & DATES	SEASAT: 6/78 Ð 10/78	ERS-1: 92Ð96 ERS-2: 95Ð01	ADEOS-I: 8/96 Ð 6/97	QuikSCAT: 6/99-11/09 ADEOS-II: 1/02-10/02	METOP: 6/2007-	OceanSat-2: 10/09-

Figure 4. Comparisons between Satellite-borne Scatterometer Missions

Instrument comparisons between satellite borne scatterometer missions. The table is missing the recently launched (9/2012) ASCAT-B scatterometer on the MetOP-B satellite, which is identical to the currently orbiting ASCAT-A scatterometer on the MetOP-A satellite listed in the table. [http://www.scp.byu.edu/data/scattscompare.html]

Satellite-borne scatterometers have two basic antenna configurations, fan-beam and pencil-beam. Each uses a different scanning pattern to acquire σ° measurements. In the fan-beam configuration, the antenna 'fans out' at multiple incidence and azimuthal angles with beams oriented along the orbit track. In the pencil-beam configuration, the antenna rotates beams at two fixed incidence angles in a conical-scanning pattern. Simultaneous σ° measurements are acquired at multiple azimuthal angles as the scatterometer travels along the orbit track. A fan-beam scatterometer acquires σ° measurements over a wide range of incidence angles; however, a fan-beam scatterometer has a reduced spatial coverage as compared to a conical-scanning pencil-beam scatterometer. In contrast, a conical-scanning pencil-beam scatterometer acquires σ° over a wider swath width; however, a conical-scanning pencil-beam scatterometer is limited to two incidence angles.

2.3 NASA's SeaWinds Scatterometer on the QuikSCAT Satellite

NASA's SeaWinds scatterometer on the QuikSCAT satellite was launched June 1999 and operated continuously until November 2009, providing the longest continuous microwave climate record to date. SeaWinds is a Ku-band (13.4 GHz, 2.54 centimeter wavelength) microwave radar which acquired σ° measurements at multiple azimuthal angles and two fixed incidence angles of 46^0, over an inner beam swath width of 1400 kilometers at horizontal transmit and receive polarization (HH), and 54^0 over an outer beam swath width of 1800 kilometers at vertical transmit and receive polarization (VV) (Figure 5). QuikSCAT has a conical-scanning pencil-beam antenna configuration with a much wider, more continuous swath

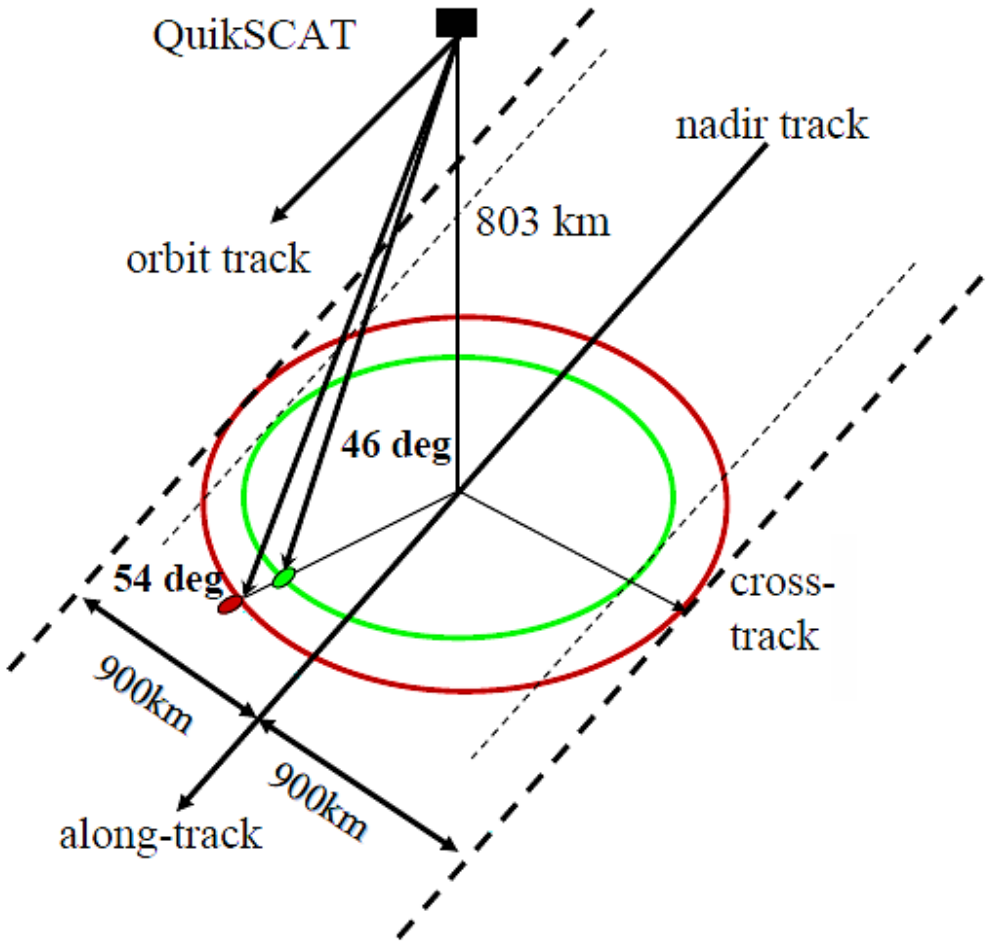

Figure 5. QuikSCAT Viewing Geometry
SeaWinds conical-scanning pencil-beam antenna pattern. [*Hicks and Long*, 2010]

width than previous scatterometer missions (Figure 4). The wide swath width provided complete spatial coverage of the polar regions twice daily and partial spatial coverage multiple times daily, in contrast to previous scatterometer missions which required multiple days for complete spatial coverage of the polar regions (Figure 4). The spatial resolution is set by the elliptical antenna footprint at ~25-35 kilometers^2 ('egg'); however, onboard range Doppler processing improves the spatial resolution to ~6-25 kilometers^2 ('slice') [*Spencer et al.*, 2000] (also Figure 4).

2.4 Scatterometer Image Reconstruction (SIR) Algorithm

The Scatterometer Image Reconstruction (SIR) algorithm [*Early and Long*, 2001; *Long et al.*, 1993] was specifically designed for resolution enhancement of satellite-borne scatterometer data. It utilizes multiple overlapping orbital passes and extracts information from the side lobes of the measurement response function to reconstruct σ° measurements at a higher spatial resolution. Images are time averaged using local time of day and separated by morning (12am-8am) and evening (4pm-12pm) orbital passes [*Hicks and Long*, 2010]. For QuikSCAT scatterometer data, it produces SIR formatted 'egg' gridded image data from the elliptical antenna footprint at a nominal spatial resolution[15] of 4.45 kilometers^2 and an effective spatial resolution[16] of ~8-10 kilometers^2, and SIR formatted 'slice' gridded image data using range gated footprints at a nominal spatial resolution of 2.225 kilometers^2 and effective spatial resolution of ~5 kilometers^2.

---

[15] spatial resolution of SIR gridded σ° measurements
[16] spatial resolution of the initial measurement response function prior to resolution enhancement

2.5 Scatterometer Data

For this study, vertically polarized, morning and evening, 'egg' gridded, σ°, measurements generated by the SIR algorithm were used. Image data mapped in a Lambert azimuthal equal area projection[17] were acquired over the complete 1999-2009 QuikSCAT mission from the NASA sponsored Scatterometer Climate Record Pathfinder Project (http://www.scp.byu.edu) at Brigham Young University (image data provided courtesy of Dr. David Long). Image data were ice masked (http://bprc.osu.edu/wiki/Jason_Box_Datasets) using a MODIS derived land surface classification which identifies permanent ice cover on the Greenland ice sheet (ice mask provided courtesy of Dr. Jason Box), then resampled at a spatial resolution of 24 kilometers for comparison with snow accumulation data acquired from the Polar MM5 mesoscale climate model. Pixels along the periphery of the ice sheet assumed to be mixed land/ice surfaces were removed. An initial Greenland ice sheet area of 1.73 X 10^6 kilometers^2 was obtained.

Annual time series were constructed for each pixel within the ice mask, alternating morning and evening σ° measurements defined by $\sigma_v^\circ(t)$. A ~12 hour time interval was obtained between samples. For each year over the time period 2000-2008, each time series contains 728 samples, for 1999 (starts DOY 200), each time series contains 328 samples, and for 2009 (ends DOY 327), each time series contains 654 samples. A total of 6806 samples were obtained over the QuikSCAT mission.

---

[17] calculated using a local Earth radius centered over the Greenland ice sheet

Two methods were used to replace missing σ° measurements. Over fixed freezing season dates DOY 306-60, the snowpack was assumed to be frozen to penetration depth and σ° signatures were observed to be relatively stable outside of the ablation zone. Missing freezing season σ° measurements within each annual time series were replaced with the average freezing season σ° value. Over fixed melt season dates DOY 61-305, σ° signatures were observed to be relatively unstable as the result of liquid water content within the snowpack. Missing melt season σ° measurements within each annual time series were replaced with the first following σ° measurement. Image data were selected to facilitate future multiple frequency comparisons between QuikSCAT, or the similar Ku-band OSCAT, and the C-band ASCAT which operates exclusively at VV with an 'egg' gridding.

2.6 Microwave Scattering Mechanisms

On the Greenland ice sheet, normalized radar cross section characterizes the relationship between the radar and time-varying geophysical near-surface properties of the snowpack. Snowpack stratigraphy in regions of the Greenland ice sheet that experience seasonal melt-refreeze metamorphosis is composed of dominant scattering layers consisting of large ice-scatterers (e.g., ice layers, pipes, glands, and lenses) with differing orientations, sizes, and shapes embedded at differing depths within a sequence of annual layers of snow accumulation each with differing snow grain sizes, densities and layer thicknesses.

There are two microwave scattering mechanisms that control the interaction between the propagating EM wave and snowpack stratigraphy, volume and surface scattering. At QuikSCAT's high incidence angles (54^0 VV and 46^0 HH), volume

scattering dominates the microwave response [*Bingham and Drinkwater,* 2000; *Drinkwater et al.*, 2001b; *Forster et al.,* 1999]. However, most σ° measurements are a combination of the two, influenced by the penetration depth.

2.6.1 Volume Scattering

When EM interaction with snowpack stratigraphy results in a volume scattering response, the scattering strength is proportional to the strength of the dielectric discontinuities within the snowpack (e.g., snow grains, ice-scatterers). The scattering pattern is determined by the density of the dielectric discontinuities as well as the orientation, size, and shape relative to the incident wavelength [*Ulaby et al.*, 1982].

2.6.2 Surface Scattering

When EM interaction with snowpack stratigraphy results in a surface scattering response, the scattering strength is proportional to the strength of the dielectric constant at the dielectric interface (e.g., air/snow surface boundary, snow grain/ice scatterer boundary, boundaries between annual layers of snow accumulation with differing densities, wet and dry snow layer interfaces). The scattering pattern is determined by the roughness of the dielectric interface relative the incident wavelength [*Ulaby et al.*, 1982].

2.7 Penetration Depth

The Ku-band penetration depth of QuikSCAT is limited to the upper layers of the snowpack and dependent on snowpack stratigraphy. Figure 6 illustrates the

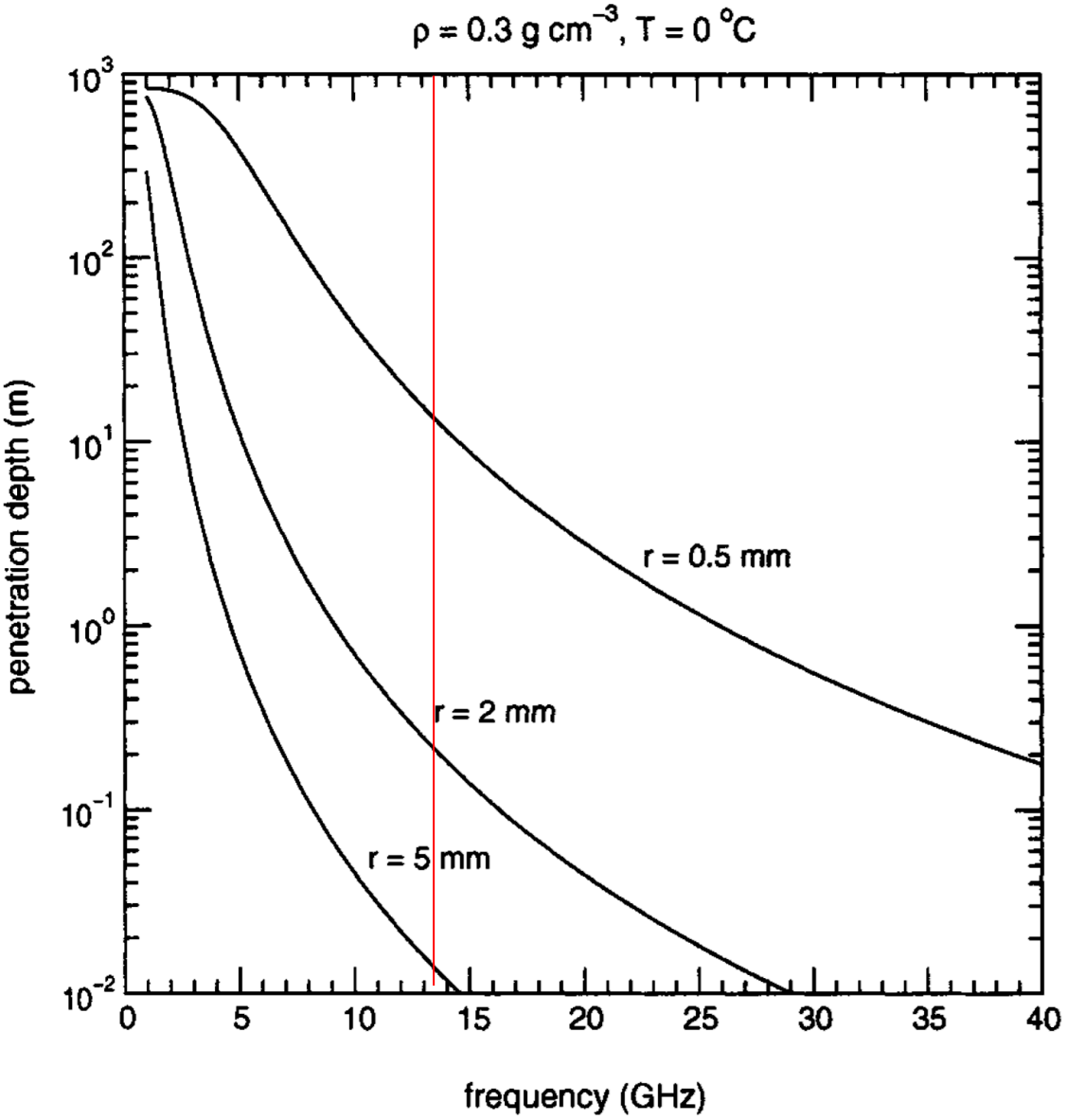

Figure 6. Theoretical Dry Snow Microwave Penetration Depths
Theoretical dry snow microwave penetration depths versus frequency as a function of density (0.3 centimeters^{-3}), temperature (0°C), and grain radii (r = 5millimeters, 2 millimeters, and 0.5 millimeters). The frequency response was computed using a Raleigh scattering model [*Drinkwater,* 1989]. The red line represents the 13.4 GHz operating frequency of QuikSCAT. Over the given frequency range, as r increases, penetration depth decreases. For QuikSCAT over the given r range, theoretical penetration depths in dry snow range from ~1 centimeter to ~10 meters. [*Bingham and Drinkwater*, 2000]

microwave response from dry snow; however, if dominant scattering layers are present within snowpack stratigraphy, microwave penetration depth is reduced.

The principal parameter controlling the penetration depth of the propagating EM wave is the extinction coefficient, κ_e, defined in units of Nepers[18] per meter (Np m^{-1}) by

$$\kappa_e = \kappa_a + \kappa_s \quad (2)$$

where κ_a is defined as the absorption coefficient (Np m-1) and κ_a is defined as the scattering coefficient (Np m-1) [*Ulaby et al.*, 1982].

Absorptive loss is controlled by the dielectric properties and temperature of the snowpack, influenced by layer thickness and density. Scattering loss is controlled by snow metamorphism, influenced by the size of the scatterers (e.g., snow grains, ice-scatterers) within the snowpack [*Drinkwater et al.,* 2001b]. *Dierking et al.* 2012 suggests that dry snow microwave penetration depths are ~6-7 meters at Ku-band.

[18] natural logarithmic unit used to measure the ratio of two signals relative to each other

CHAPTER 3

THE GREENLAND ICE-FACIES

This chapter describes the creation of dominant scattering layers in each of the Greenland ice-facies [*Benson*, 1962] on the Greenland ice sheet. Retrieval of snow accumulation rates from decreasing freezing season σ° signatures is dependent on knowledge of the EM scattering characteristics in each of the Greenland ice-facies. The formation of dominant scattering layers, as well as their EM scattering characteristics, varies both seasonally and spatially, influenced by thermal forcing and the presence or absence of liquid water content within the snowpack during the melt season which controls snow metamorphism [*Long and Drinkwater*, 1994]. The microwave response of an accumulating snow layer overlying a dominant scattering layer forms the basis for the retrieval of a microwave snow accumulation metric outlined in the microwave snow accumulation model described in Chapter 4.

3.1 The Greenland Ice-Facies

The Greenland ice sheet can be classified into four geophysical zones (i.e., dry snow zone, percolation zone, wet or soaked zone, and ablation zone) or ice-facies (Figure 7) characterized by liquid water content within the upper layers of the snowpack during the melt season [*Benson*, 1962; *Cuffey and Paterson*, 2010]. Snowpack stratigraphy in each of the Greenland ice-facies forms

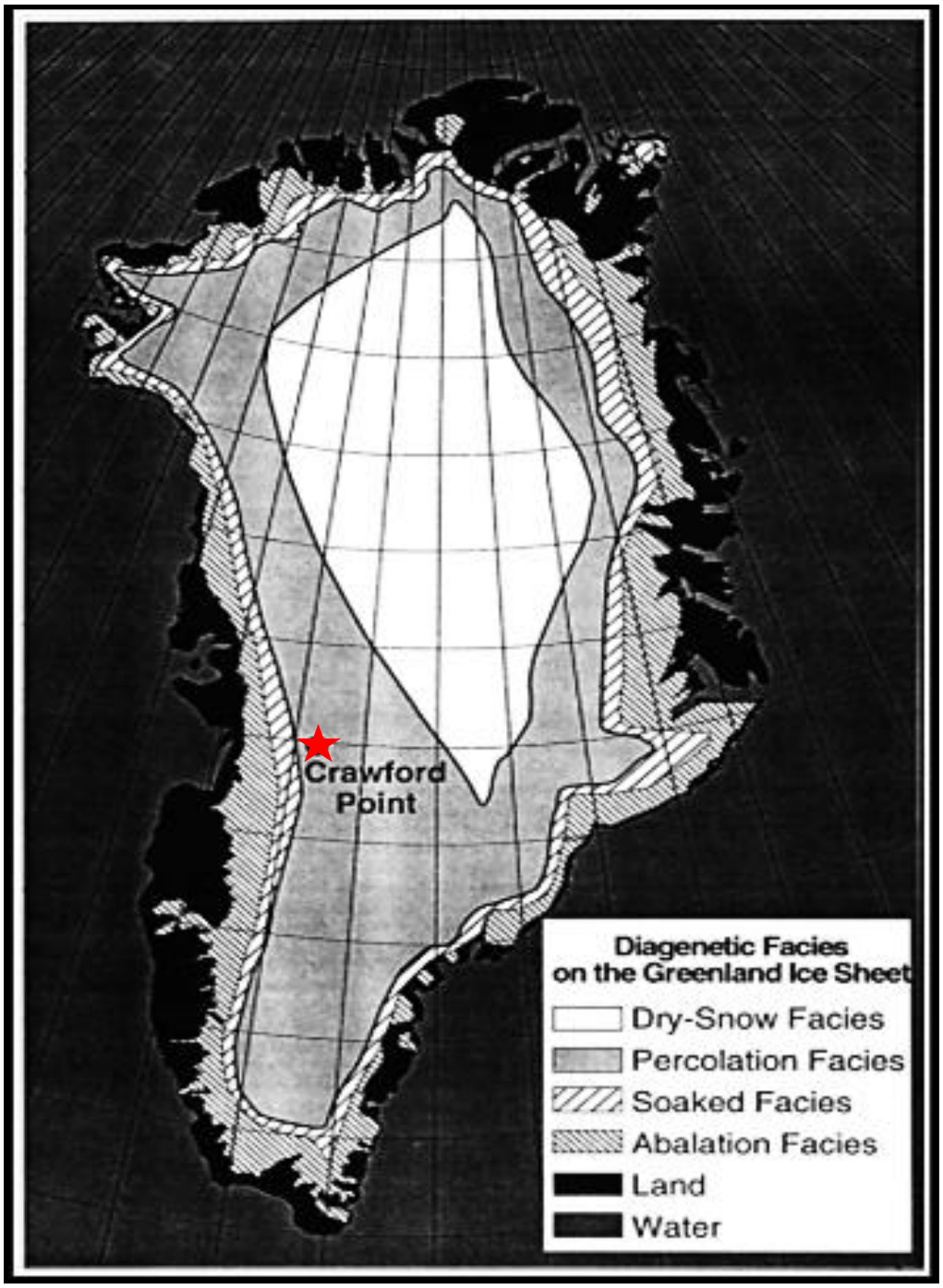

Figure 7. The Greenland Ice Facies
Ice facies of the Greenland ice sheet based on Benson [1962]. Snow pit studies at Crawford point in 1991 and 1992 indicate that this region experienced vigorous surface melting followed by downward percolation and lateral infiltration and refreezing of meltwater, which formed ice layers and pipes. Thin wind crusts and coarse-grained (1 millimeter in diameter) ice-scatterers were also observed. [*Jezek et al*, 1994]

as the result of the seasonal progression of snow accumulation at the surface followed by snow metamorphosis associated with thermal forcing. The boundaries of the Greenland ice-facies are spatially and temporally variable, influenced by atmospheric conditions, topography, latitude, and elevation.

As observed by QuikSCAT over the large-scale antenna footprint (<25 kilometers^2) within Ku-band penetration depth (<10 kilometers), a dominant scattering layer is defined by a high density of ice-scatterers that are large relative to the 2.54 centimeter incident wavelength. Dominant scattering layers significant to the microwave scattering mechanism [*Fahnestock et al.*, 1993; *Jezek et al.*, 1993; *Long and Drinkwater*, 1994; *Rignot et al.*, 1993; *Rignot*, 1995] are formed by two types of snow metamorphism: 1) dry snow metamorphosis resulting from vapor transport and sublimation, and 2) melt-refreeze metamorphism resulting from melting and subsequent refreezing processes. Over time, snow metamorphism forms a stratigraphic layering of dominant scattering layers consisting of large ice-scatterers (e.g., surface and depth hoar, bonded clusters of coalesced snow grains, ice layers, pipes, glands, and lenses) with differing orientations, sizes, and shapes embedded at differing depths within a sequence of annual layers of snow accumulation, each with differing snow grain sizes, densities, and layer thicknesses.

3.2 The Dry Snow Zone

The dry snow zone is located in the high-elevation interior of the Greenland ice sheet (Figure 7) where annual snow temperatures remain below 0˚C and liquid water content is negligible. When temperatures exceed -10˚C and steep temperature gradients exist within the upper layers of the snowpack, vapor transport and sublimation results in a dry snow metamorphic regime (i.e., kinetic) which changes

snow grain shapes, increases snow grain sizes, and increases bonding between individual snow grains. Dry snow metamorphosis forms dominant scattering layers on the surface of the snowpack in the form of surface hoar layers which consist of large needle or feather-like ice-scatterers, as well as at depth in the form of depth hoar layers which consist of large coarse-grained or faceted ice-scatterers with a base, pyramid, and prisms.

Two types of seasonally dependent depth hoar have been identified in the dry snow zone: 1) Near-surface (~10 millimeters depth) summertime depth hoar layers which form as the result of steep temperature gradients driven by solar radiation [*Alley et al.*, 1990; *Benson*, 1962], and 2) digenetic depth hoar layers which form in autumn as the result of heat and vapor flux driven by diffusion, convection, and winds *[Alley*, 1988]. Depositional depth hoar, created when surface hoar is buried at depth by snow accumulation, can form any time of the year [*Alley et al.*, 1990]. Depth hoar can have dimensions and layer thicknesses of up to several centimeters and have been traced in snow pits over hundreds of miles [*Benson*, 1962].

3.3 The Percolation Zone

The percolation zone (Figure 7) is located downglacier from the dry snow line which defines the lower boundary of the dry snow zone. When annual temperatures in this region exceed 0˚C, liquid water content is present; however, cold snow temperatures limit horizontal and vertical transport and melt water is retained within the snowpack.

Ice pipes, glands, and lenses are formed by the downward percolation of melt water at point locations where the snowpack reaches 0˚C. Lateral infiltration occurs when percolating melt water encounters a hydraulic discontinuity associated with a

fine to coarse snow grain size transition [*Pfeffer and Humphrey* 1998]. Refreezing of melt water within percolation channels forms ice pipes, and refreezing of melt water at the hydraulic discontinuity forms ice glands and lenses. Ice pipes glands, and lenses range from 2-20 centimeters wide and 10-100 centimeters long and have been observed to be spatially discontinuous with an average of a few per meter^2 [*Jezek et al.*, 1994]. An example of an ice pipe is shown in Figure 8.

When the temperature of a given mass of snow at the surface of the snowpack is raised to 0˚C, ice layers (also called 'iced firn') are formed by shallow infiltration saturation, and subsequent refreezing of melt water. Smaller snow grains have a lower melting temperature as compared to larger snow grains and preferentially melt, driven by heat flux from refreezing of larger snow grains. The melt-refreeze metamorphic regime (i.e., funicular, pendular) is dependent on the liquid water content [*Cuffey and Paterson*, 2010]. Melt-refreeze metamorphosis results in bonded clusters of coalesced snow grains with dimensions exceeding 5 millimeters, often with small ice glands and lenses found directly beneath [*Benson*, 1962]. Iced firn may have a rough surface relative to the incident wavelength, can be several millimeters to a few centimeters thick, and has been observed to be spatially continuous over several tens of meters [*Benson*, 1962]. Upglacier boundary shifts in the dry snow line can form dominant scattering layers (iced firn layers, pipes, glands, and lenses) in the upper elevations of the percolation zone which are subsequently buried by multiple annual accumulation layers when the dry snow line shifts downglacier.

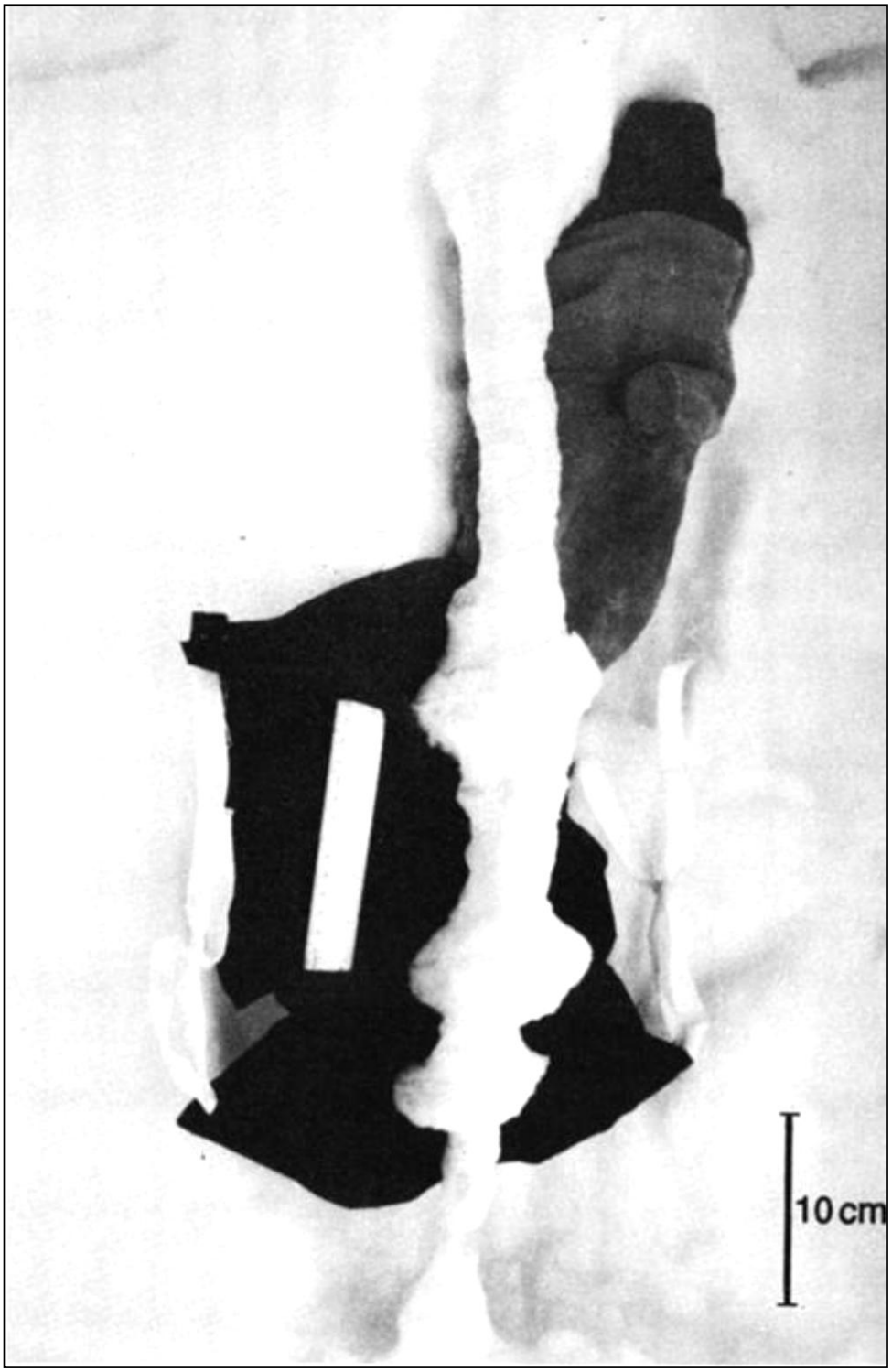

Figure 8. Ice Pipe
A 70 centimeter long ice pipe, with a diameter varying between 3 and 10 centimeters, was found in the snowpack at a depth of 1.8 meters at Crawford Point (Figure 7). Photograph by Ken Jezek. [*Rignot*, 1995]

3.4 The Wet Snow Zone

The wet snow or saturated zone (Figure 7) is located downglacier from the percolation zone. In the wet snow zone, the entire surface of the snowpack is raised to 0˚C, infiltrated with melt water, and saturated down to the previous year's annual layer of snow accumulation. This region is characterized by iced firn layers, pipes, glands, and lenses interspersed with patches of snow and firn. The superimposed ice zone (part of the saturated zone in Figure 7) is located downglacier from the snow line which defines the lower boundary of the wet snow zone. In this region, iced firn layers merge to form a continuous layer of superimposed ice which may have a rough surface relative to the incident wavelength. The lower boundary of the superimposed ice zone is defined by the equilibrium line altitude (ELA). Above the ELA, there is a net mass gain and below the equilibrium line there is a net mass loss.

3.5 The Ablation Zone

The ablation zone (Figure 7) is located downglacier from the wet snow zone below the equilibrium line, where the entire annual layer of snow accumulation is removed by ablation. This region is characterized by exposed glacial ice, cryoconite holes, and crevasses which may appear rough relative to the incident wavelength. Frozen superglacial lakes and streams may also be present and may appear smooth relative to the incident wavelength.

CHAPTER 4

MICROWAVE SNOW ACCUMULATION MODEL

This chapter outlines the microwave snow accumulation model used to retrieve a microwave snow accumulation metric from decreasing freezing season σ° signatures. An empirical relationship is derived between the retrieved microwave snow accumulation metric and spatially calibrated Polar MM5 snow accumulation rates on the Greenland ice sheet. Results of this comparison are presented and discussed, both spatially and temporally, and conclusions are drawn about the accuracy of the retrieval technique. This chapter concludes with recommendations for future work to further establish a robust, well-understood, relationship between Ku-band radar backscatter and snow accumulation rates that can potentially reduce the current uncertainty in both snow accumulation estimates and mass balance calculations on the Greenland ice sheet

4.1 Algorithm Overview

The inverse linear relationship between decreasing freezing season σ° signatures and snow accumulation rates in regions that experience seasonal melt-refreeze metamorphosis hypothesized by *Wismann et al.* [1997] and *Nghiem et al.* [2005] is evaluated using the microwave snow accumulation model outlined in the following sections. The microwave snow accumulation model is defined using a

three step algorithm to retrieve a microwave snow accumulation metric: 1) regions of the Greenland ice sheet that experienced seasonal melt-refreeze metamorphosis and potentially formed dominant scattering layers are annually delineated using a microwave melt model which calculates the melt extent and intensity using a simple two layer physical model of a melting snow surface [*Hicks and Long*, 2011] (Section 4.2), 2) freeze-up and melt-onset dates to identify stable freezing season σ° signatures are detected on a pixel-by-pixel basis using a Markov model derived from the microwave melt model [*Hicks and Long*, 2011] which classifies ice-state transitions as frozen, melting, or refreezing (Section 4.3), and 3) freezing season σ° decreases are calculated on a pixel-by-pixel basis to retrieve a microwave snow accumulation metric for comparison with spatially calibrated Polar MM5 snow accumulation rates on the Greenland ice sheet using a retrieval technique similar to *Wismann et al.* [1997] (Section 4.4).

A simple empirical relationship between freezing season σ° decreases and spatially calibrated Polar MM5 snow accumulation rates on the Greenland ice sheet is derived and analyzed to determine the potential for large-scale mapping of freezing season snow accumulation rates using this retrieval algorithm (Section 4.5). Azimuthal modulation of σ° measurements, identified by *Ashcraft and Long* [2006a], may influence freezing season σ° decreases; however, it is neglected in this study.

4.2 Delineating Regions Forming Dominant Scattering Layers

This section outlines the microwave melt model used in the snow accumulation model. Background information on the microwave response to melting and refreezing processes within the snowpack is provided, and an example of a melt

and refreeze event as observed over the Greenland ice sheet by QuikSCAT is illustrated and discussed. Annual masks delineating regions of the Greenland ice sheet that experienced seasonal melt-refreeze metamorphosis and potentially formed dominant scattering layers are defined using a microwave melt model.

4.2.1 Background

Liquid water content, m_v, is the most important parameter affecting the microwave response over the Greenland ice sheet. The introduction of m_v into an initially dry snowpack by melting is controlled by solar radiation at the surface and atmospheric conditions, such as warm air advection associated with southern approaching storm systems or warm ocean fronts [*Hall et al.,* 2009; *Wang et al.*, 2007]. *Steffen et al.* [2004] suggest that timing and duration are also significant. During the melting process, heat flux propagates from the surface of the snowpack downward by conduction to colder, subsurface snow, firn, and ice layers [*Cuffey and Paterson*, 2010].

When m_v is detectable over the antenna footprint within the penetration depth of the satellite-borne microwave instrument, σ° measurements are controlled by surface scattering at the dielectric interface of the wet layer [*Ulaby et al.*, 1982] and closely follow changes in m_v in the top few centimeters of the snowpack [*Hicks and Long*, 2011]. Increasing m_v results in rapid relative increases in the imaginary part of the dielectric constant, ϵ'', which drastically changes the EM scattering characteristics. Even initial wetting of the snowpack with m_v= 0.5% can increase ϵ'' by an order of magnitude, which decreases penetration depth by the same ratio [*Ulaby et al.*, 1982]. Subsurface penetration can be limited to a single wavelength

[Rott and Sturm, 1991], resulting in σ° measurements that are significantly reduced during melt events by absorption and extinction of the EM wave at the dielectric interface of the wet layer.

The refreezing process is complex, controlled by the thermodynamic properties of the snowpack, as well as by atmospheric conditions such as strong gusting winds, temperature fluctuations, and snow accumulation which can drive steep temperature gradients within the upper layers of the snowpack. During the refreezing process, the downward propagation of heat flux by conduction to deeper, colder, subsurface snow, firn, and ice layers continues. However, near-surface heat flux is variable and may continue to propagate downward into the snowpack at a slower rate, or may propagate upward by convection and radiation. Heat flux propagation from the surface of the snowpack into the atmosphere may result in the formation of a refrozen dry surface layer overlying a wet subsurface layer [*Ashcraft and Long*, 2005; *Hall et al.*, 2009; *Hicks and Long*, 2011; *Matzler and Wismann,* 1994], which allows for subsurface penetration and volume scattering within the refrozen dry surface layer before absorption and extinction of the EM wave at the dielectric interface of the wet subsurface layer.

During refreeze events, m_v decreases, rapidly decreasing ϵ'', which increases σ° measurements. The net increase in σ° measurements is dependent on the EM scattering characteristics of the snowpack, which determines the microwave scattering mechanism. Snowpack stratigraphy may consist of a wet layer of decreasing m_v which gradually increases σ° measurements, or a refrozen dry surface layer overlying a wet subsurface layer, which abruptly increases σ° measurements. If a new dominant scattering layer is formed during refreezing, σ° measurements

can significantly and abruptly increase as the result of increased volume scattering from large ice-scatterers, exhibited as a step response in the σ° signature.

In terms of the σ° signature, the melt season is defined when m_v is present within the snowpack. During the melt season, σ° signatures are unstable, characterized by erratic transitions between the detection of melt and refreeze events interspersed with intermittent periods of stability when m_v is not detectable and the snowpack is frozen to penetration depth. Snow is accumulating at the surface; however, consistent decreasing σ° signatures are not observed and a microwave snow accumulation metric is not explicitly retrievable. The freezing season is defined from the final refreeze event of the melt season, termed freeze-up, to the initial melt event of the following melt season, termed melt-onset. During the freezing season, the snowpack is frozen to penetration depth, σ° signatures are stable, and consistent decreasing freezing season σ° signatures are observed.

Figure 9 illustrates the melting and refreezing processes in a spatial context, as observed by QuikSCAT in 2002. These are vertically polarized, morning orbital pass, enhanced resolution 'slice' image data generated by the SIR algorithm. The anomalous melt event is associated with the intrusion of a high pressure ridge from the North Atlantic Ocean which resulted in warm air advection and strong southerly flow [*Wang et al.* 2007]. Figure 9 A and F represent the microwave response during the freezing season prior to and following the 2002 melt season when the snowpack was frozen to penetration depth and σ° signatures were stable. Figure 9 B, C, D, and E represent melt and refreeze events during the 2002 melt season. White represents high σ° values resulting from volume scattering within snowpack stratigraphy in regions that experienced seasonal melt refreeze

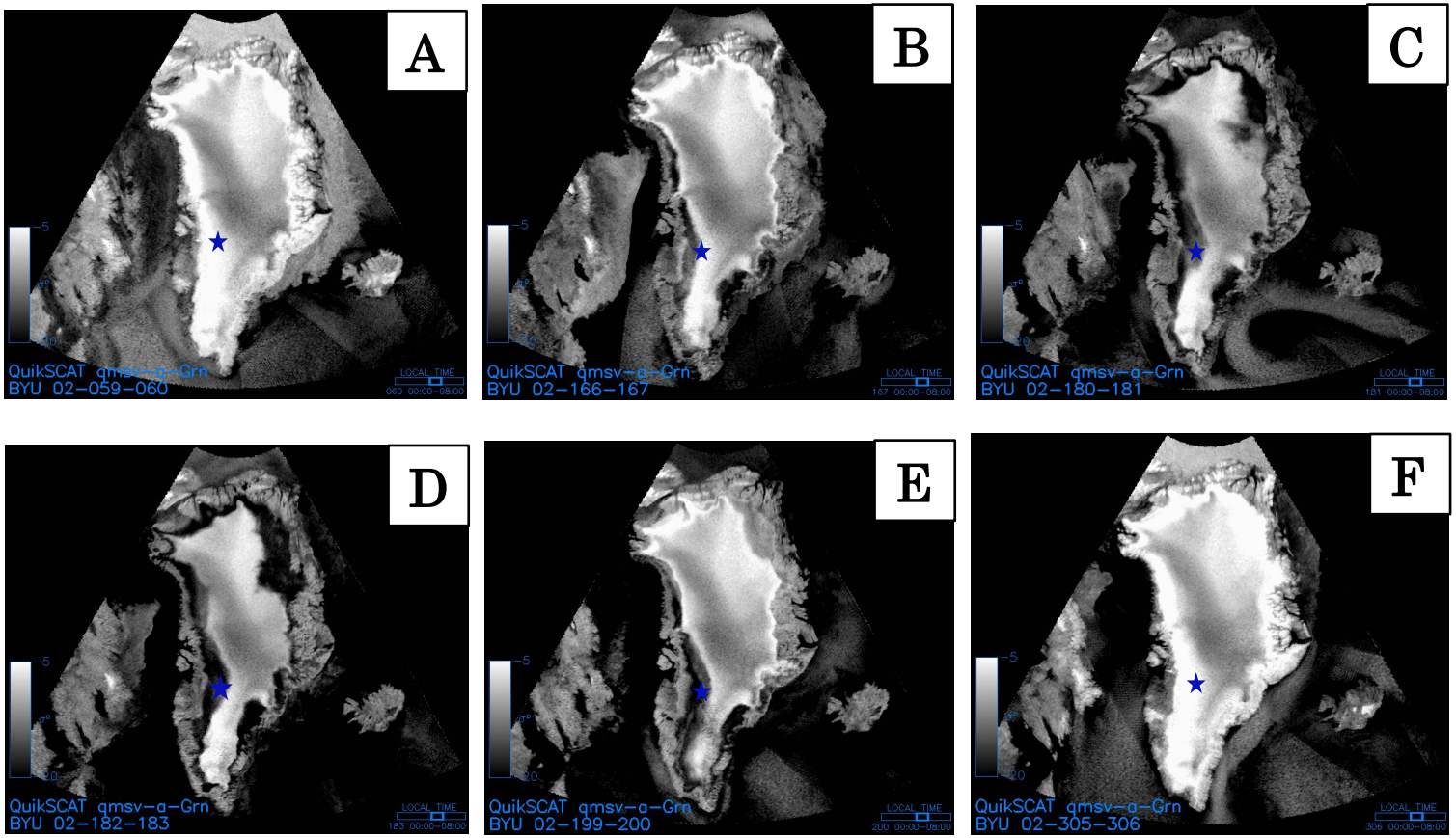

Figure 9. QuikSCAT Times Series of 2002 Melt and Refreeze Events

Melting and refreezing processes on the Greenland ice sheet during the anomalous 2002 melt season as seen by a satellite borne scatterometer. The blue star represents the location of Crawford Point. Images were acquired from the NASA sponsored Scatterometer Climate Record Pathfinder Project at Brigham Young University provided courtesy of Dr. David. Long. [http://www.scp.byu.edu]

metamorphosis and formed dominant scattering layers (percolation, wet snow, and ablation zones). Grey represents decreased σ° values resulting from increased attenuation of the EM wave by increased volume scattering from snow grains within the dry layer (dry snow zone). Black represents low σ° values resulting from surface scattering in regions where m_v is present within the snowpack (percolation, wet snow, and ablation zones). The EM wave is absorbed and attenuated within the wet layer.

Of particular note is the presence of m_v in the higher elevations of the northeastern dry snow zone, illustrated in Figure 9 C and D. A significant upglacier shift in the dry snow line was followed by the formation of a dominant scattering layer. Given low snow accumulation rates in this region (Figure 1 and Figure 3), this dominant scattering layer remained within penetration depth and influenced σ° signatures for several years following the melt event. Increased volume scattering within the snowpack from large ice-scatterers in the northeastern dry snow zone is observed in comparisons between Figure 9 A and F as increases in σ° values.

4.2.2 Microwave Melt Model

Given the sensitivity of microwaves to m_v within the snowpack, several microwave melt models have been developed for both passive [*Abdalati and Steffen*, 1995, 1997] and active [*Ashcraft and Long*, 2006a; *Hicks and Long*, 2011; *Nghiem et al.*, 2001; *Wismann,* 2000] satellite-borne microwave instruments.

For this study, the Integrated Melt Severity Index (IMSI) [*Hicks and Long*, 2011] was used to detect the presence of m_v within the snowpack during the melt season and annually delineate regions of the Greenland ice sheet that experienced

seasonal melt-refreeze metamorphosis and potentially formed dominant scattering layers. The IMSI is derived from the Q-α microwave melt model [*Ashcraft and Long*, 2006a] which is a technique based on thresholding a QuikSCAT, Q, signal, $q(t)$, based on the net attenuation, α, of $q(t)$ within a wet surface layer. Q-α utilizes a simple two layer physical model of a melting snowpack to separate a σ° measurement into a contribution from a wet surface layer and an attenuated contribution from a dry subsurface layer. IMSI (I_χ) is defined in units of Np by

$$I_\chi = \sum_{k=1}^{M(t)} \chi\,(t_k)\,\Delta t \tag{3}$$

where $M(t)$ is the total number of σ° measurements within a time series where m_v is detected, Δt is the time interval between σ°measurements, and $\chi(t_k)$ is the time dependent melt severity index, MSI.

The MSI is equivalent to the parameterized net attenuation within a wet surface layer and a dry subsurface layer as described by the two layer physical model and used to detect the time-varying amount of m_v present at each σ° measurement within a time series. MSI, $\chi(t)$, is defined in units of Np by

$$\chi(t) = \frac{q(t)cos\theta_{wet}}{20\ log_{10}\,e} \tag{4}$$

transmission angle through the wet surface layer. The transition between frozen and

is based on a threshold of q_0 = 3dB [*Ashcraft and Long*, 2006a] corresponding to a wet surface layer with m_v = 1.0%, a melt depth of 2.4 centimeters, a grain size of r = 0.75 millimeters, and density p_s = 0.4 grams/centimeter^3, which is consistent with observed geophysical near-surface properties of the snowpack on the Greenland Ice Sheet [*Benson*, 1962]. Melt is detected and $\chi(t)$ calculated, when the threshold is exceeded, $q(t) > q_0$.

4.2.3 Microwave Melt Model Limitations

Hicks and Long [2011] identify three limitations in the microwave melt models ability to measure the intensity of melt events: 1) noise corrupts the σ° measurement which may result in a bias in χ, 2) σ° contributions from all layers are combined into a single bulk parameter, σ°_{dry}, which may vary if stratified layers are altered during the melt season, and 3) neglecting σ°_{wet} (i.e., the estimated σ° measurement from a completely wet layer) in the original parameterization of the two layer physical model may result in a dependence on snowpack stratigraphy and saturation during strong melt events.

The study also noted the microwave melt model was designed for application to snow and firn layers rather than glacial ice. Melt intensity estimates in the ablation zone are therefore invalid. Melt intensity is not used in this study, as the microwave melt model is simply used to identify the presence of m_v during the melt season. Therefore, the limitations do not adversely affect the results of the microwave snow accumulation model and are neglected.

4.2.4 Scatterometer Data for Microwave Melt Model

Annual σ° time series were constructed from image data acquired over the time period 1999-2009 alternating vertically polarized, morning and evening, enhanced resolution, 'egg' gridded, σ° measurements, defined by $\sigma^\circ_v(t)$. Vertically polarized σ° measurements have previously been used to detect the presence of m_v within the snowpack [*Ashcraft and Long*, 2006a; *Bhattarachya*, 2009; *Hicks and Long*, 2011; *Nghiem et al*, 2001].

During initial testing of the microwave melt model using annual $\sigma^\circ_v(t)$, false melt detections were frequently observed in the lower elevations of the percolation zone in southeastern Greenland. This region experiences snow accumulation rates (Figure 1 and Figure 3) which can result in freezing season σ° decreases exceeding the melt threshold of q_0 = 3dB. Alternate σ° time series were constructed over fixed melt season dates DOY 61-305, defined by $\sigma^\circ_{v,melt}(t)$, and then tested using the microwave melt model. Over the majority of the Greenland ice sheet changes in both the spatial extent and intensity of melt were insignificant. In the lower elevations of the percolation zone in southeastern Greenland, false melt detections were minimized. Therefore, $\sigma^\circ_{v,melt}(t)$ were used in the microwave melt model.

4.2.5 Estimation of Backscatter Value from a Dry Snow Surface

An estimated σ°value for a completely dry snow surface, $\sigma^\circ_{v\,dry}$ was calculated using a least squares linear regression of $\sigma^\circ_v(t)$ for fixed freezing season dates DOY 306-60, before and following the melt season over the time period 1999-2009. Most σ° signatures over this time period were observed to remain relatively stable outside of the ablation zone and the snowpack was assumed to be frozen to penetration

depth. A minimum σ° value was calculated for $\sigma_v^\circ(t)$ for the time period before the melt season $\sigma_{v,min}^\circ$, and a maximum σ° value was calculated for $\sigma_v^\circ(t)$ for the time period following the melt season, $\sigma_{v\,max}^\circ$. To obtain an estimated value for $\sigma_{v,dry}^\circ$, $\sigma_{v,min}^\circ$ and $\sigma_{v,max}^\circ$ were averaged.

4.2.6 Microwave Melt Model Masks

Annual IMSI-derived binary masks, $I_{\chi,mask}$, delineating regions that experienced seasonal melt-refreeze metamorphosis and potentially formed dominant scattering layers were constructed as follows. The dry snow zone was defined in the strict sense of *Benson* [1962], by pixels where negligible annual melt was experienced. If negligible annual melt was detected by the microwave melt model, $I_\chi = 0$, then $I_{\chi,mask} = 0$. The melt zone includes the percolation, wet snow, and ablation zones and is defined by pixels where annual melt was experienced. If annual melt was detected by the microwave melt model, $I_\chi > 0$, then $I_{\chi,mask} = 1$.

Upglacier boundary shifts in the dry snow line can result in the formation of dominant scattering layers which are subsequently buried by multiple annual accumulation layers when the dry snow line shifts downglacier. Low snow accumulation rates in the high-elevation interior allow these dominant scattering layers to remain within penetration depth and control the microwave response for several years, resulting in decreasing σ° signatures occurring in years that do not experience melt-refreeze metamorphosis.

To simplify the microwave snow accumulation model and constrain the microwave snow accumulation metric to annual freezing seasons, a pixel must experience melt as defined by the microwave melt model, $I_{\chi,mask} = 1$, the year prior

and the year following the retrieval of a stable freezing season σ° signature. It is observed that there are a significant number of multiyear decreasing σ° signatures present within QuikSCAT scatterometer data. However, retrieval of these additional pixels requires a more sophisticated algorithm and are therefore neglected in this study.

4.3 Identifying Stable Freezing Season Backscatter Signatures

This section outlines the Markov model used in the snow accumulation model. Freeze-up and melt-onset dates to identify stable freezing season σ° signatures are detected on a pixel-by-pixel basis using the Markov model. Stable freezing season σ° signatures are used in the third step of the retrieval algorithm to calculate a microwave snow accumulation metric.

4.3.1 Markov Model

To detect freeze-up and melt-onset dates and identify stable freezing season σ° signatures, a constrained one step Markov chain model [*Hicks and Long*, 2011] was used. Based on a set of transition thresholds and the previous ice-state, the Markov model classifies three ice-state transitions: frozen, melting, and refreezing. The initial ice-state, $M(t_n)$, is given by

$$M(t_n) = \begin{cases} 0 : frozen \\ 1 : melting \\ 2 : refreezing \end{cases} \quad (5)$$

Three decision rules define transitions from the initial ice-state, $M(\,t_n)$, at time t_n, to the next ice-state, $M_i(t_{n+1})$, in the next time-step, t_{n+1}, where i = 0, 1, 2 represents the next ice-state, $M_i(t_{n+1})$, in the next time-step, t_{n+1}, where i = 0, 1, 2 represents frozen, melting, and refreezing ice-states, respectively.

The transition from a frozen ice-state is strictly to a melting ice-state. The decision rule for the transition from a frozen ice-state to a melting ice-state, $M_0(t_{n+1})$, in the next time-step, t_{n+1}, is given by

$$M_0(\,t_{n+1}) \;=\; \begin{cases} 0 \;:\; q(t) \,<\, q_0 \\ 1 \;:\; q(t) \,\geq\, q_0 \end{cases} \tag{6}$$

where $q(t) = \sigma^{\circ}_{dry} - \sigma^{\circ}(t)$ represents the deviation of $\sigma^{\circ}(t)$ from the estimated σ° measurement from a completely dry layer, σ°_{dry}, as described in Section 4.2.2. The transition threshold, q_0 = 3dB, between a frozen ice-state and melting ice-state is determined by the net attenuation within a wet surface layer as described by a simple two layer physical model of a melting snowpack [*Ashcraft and Long*, 2006a].

Once the initial transition from a frozen ice-state to a melting ice-state is detected, the same decision rule is used for transitions to a (continued) melting ice-state or a refreezing ice-state. Transitions between refreezing and melting ice-states are identified by increasing or decreasing m_v within the snowpack. The decision rule for melting or refreezing ice-state transitions, $M_{1,2}(\,t_{n+1})$, in the next time-step, t_{n+1}, is given by

$$M_{1,2}(t_{n+1}) \;=\; \begin{cases} 0 \;:\; q_2 \,\leq\, q(t) < q_1 \\ 1 \;:\; q(t) \,\geq\, q_1\,, r(t) \leq r_0 \\ 2 \;:\; q(t) \,\geq\, q_1\,, r(t) > r_0 \end{cases} \tag{7}$$

where a melt to refreeze metric is defined by $r(t_n) = \sigma^\circ(t_n) - \sigma^\circ(t_{n-1})$ with a transition threshold of r_0 = 0.5 dB. Transitions back to a frozen ice-state are determined using an increased transition threshold of q_1 = 1.0 dB.

Melt-onset, t_{melt}, is defined at the σ° measurement prior to the first transition from a frozen ice-state to a melting ice-state. Given that transitions directly from a melting ice-state to a frozen ice-state were frequently observed without an intermediate refreezing ice-state, freeze-up, t_{freeze}, is defined at the σ° measurement following the last transition from a melting or refreezing ice-state to frozen ice-state. The freezing season, Δt_{fs}, is defined by $\Delta t_{fs=} t_{freeze} - t_{melt}$

4.3.2 Scatterometer Data for Markov Model

As in the microwave melt model, $\sigma^\circ_{v,melt}(t)$ and $\sigma^\circ_{v,dry}$ over the time period 1999-2009 were used in the Markov model. Given that annual σ° time series are a fixed length, the relationship between the freezing season and the melt season is inverse and influenced by atmospheric conditions, topography, latitude, and elevation. Longer freezing seasons result in shorter melt seasons and shorter freezing season result in longer melt seasons. In general, the longest freezing seasons occur in the high-elevation interior, near the dry snow line, and decrease descending downglacier towards the ice sheet periphery.

4.4 Retrieval of a Microwave Snow Accumulation Metric

This section outlines the snow accumulation model. Background information and a time series example of the microwave response of a layer of accumulating snow overlying a fixed dominant scattering layer, which forms the basis for the

retrieval algorithm, are provided. Freezing season σ° decreases in regions of the Greenland ice sheet that experienced seasonal melt-refreeze metamorphosis and potentially formed dominant scattering layers are calculated on a pixel-by-pixel basis using stable freezing season σ° time series. A microwave snow accumulation metric is retrieved for comparison with spatially calibrated Polar MM5 snow accumulation rates on the Greenland ice sheet in Section 4.5.

4.4.1 Background

Retrieval of a microwave snow accumulation metric from freezing season σ° decreases is derived from the retrieval technique first used by *Wismann et al.* [1997] and then subsequently adapted by *Nghiem et al.* [2005]. Theoretical backscatter models used by *Wismann et al.* [1997] and *Nghiem et al.* [1990b] to validate the hypothesis that observed decreasing freezing season σ° signatures are linked to snow accumulation rates suggest the relationship is inverse and linear(dB).

The theoretical relationship between Ku-band radar backscatter and snow accumulation rates in regions of the Greenland ice sheet that experience seasonal melt-refreeze metamorphosis and form dominant scattering layers is based on the simple two layer model illustrated in Figure 10.

A propagating EM wave crosses the air snow surface boundary, which is smooth and relatively transparent to the EM wave at Ku-band, and negligible surface scattering occurs [*Drinkwater et al.*, 2001a]. As the EM wave continues to propagate downward towards the dominant scattering layer, it encounters snow grains which are small relative to the incident wavelength and is attenuated by absorption and a Raleigh scattering response within the layer of accumulating snow.

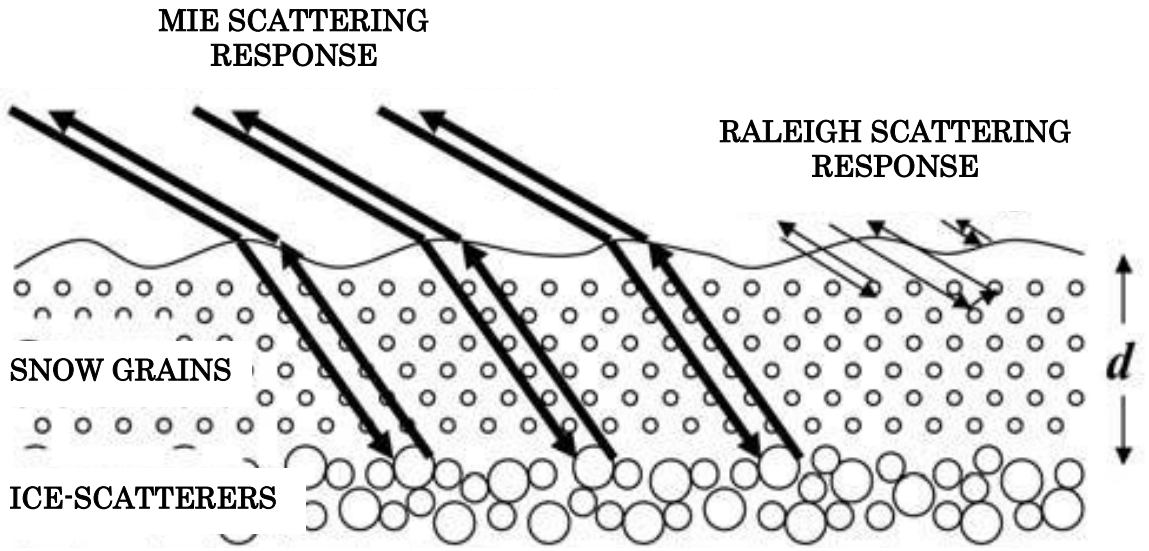

Figure 10. Microwave Scattering from a Snow Covered Ice Layer
Microwave scattering from an accumulating snow layer overlying a fixed dominant scattering layer consisting of ice-scatters that are large relative to the incident wavelength. [*Nghiem et al.*, 2005]

Once the EM wave reaches the dominant scattering layer the microwave scattering mechanism changes from a Raleigh scattering response to Mie scattering response when it encounters ice-scatterers which are large relative to the incident wavelength. The net σ° measurement dominated by Mie scattering response from the underlying ice-facie. Two-way attenuation resulting from a Raleigh scattering response within the overlying a layer of snow accumulation forces a decrease in the σ° measurement over time with increased snow accumulation rates.

4.4.2 Calculating Freezing Season Backscatter Decreases

Freezing season σ° decreases are calculated on a pixel-by-pixel basis to retrieve a microwave snow accumulation metric. Stable freezing season σ° time

series are linearly regressed from freeze-up, t_{freeze}, to melt-onset, t_{melt}, with fit line equation defined in units of dB by

$$\Delta\sigma^{\circ}_{fs} = \quad \sigma^{\circ}\left(t_{freeze}\right) - \sigma^{\circ}(t_{melt}) \tag{8}$$

where the microwave snow accumulation metric, $\Delta\sigma^{\circ}_{fs}$, is defined as the total freezing season σ° decrease from t_{freeze} to t_{melt} and assumed to represent the change in cumulative snow depth in m w.e accumulated over the time interval Δt_{fs}.

4.4.3 Limitations of the Microwave Snow Accumulation Model

Without question, the outlined microwave snow accumulation model is an oversimplification of the complex relationship between radar backscatter and snow accumulation rates on the Greenland ice sheet. One limitation identified is the premise that the underlying dominant scattering layer remains fixed during the freezing season. The snowpack is actually changing, by densification as well as by dry snow metamorphosis. While the dominant scattering layer is incompressible, snow grains are compacted over time, which reduces the dielectric contrast between the dominant scattering layer and the layer of snow accumulation. *Wismann et al.* [1997] suggested that the effect of densification on freezing season σ° decreases is likely small. The effect of dry snow metamorphosis, however, may be significant [*Bingham and Drinkwater,* 2000]. The formation of depth or surface hoar layers increases σ° values by increasing the Mie scattering response within the dominant scattering layer which offsets decreases in σ° values by snow accumulation. The question remains, to what extent is dry snow metamorphosis controlling the

observed freezing season σ° decreases and to what extent is snow accumulation controlling the observed response (*personal communication, Dr, Mark Drinkwater*)?

4.4.4 Scatterometer Data for Snow Accumulation Model

Each of the two previous studies used different polarizations to retrieve a microwave snow accumulation metric. *Wismann et al.* [1997] used vertically polarized σ° measurements acquired from the C-band ESCAT, which operates exclusively at VV. QuikSCAT, however, operates at both HH and VV. Horizontally polarized σ° measurements acquired from QuikSCAT over the time period 1999-2003 were used by [*Nghiem et al.*, 2005] on the basis that observed decreasing freezing season σ° signatures displayed an increased response. It has also been suggested that horizontally polarized σ° measurements are more sensitive to the formation of dominant scattering layers.

It was observed in this study that horizontally polarized σ° measurements acquired from QuikSCAT over the complete 1999-2009 time series also displayed an increased response in the form of slightly larger freezing season σ° decreases and slightly larger step responses in σ° signatures, indicating the formation of new dominant scattering layers. Given that the relationship between radar backscatter and snow accumulation is currently not well-understood, it is unknown whether an increased response will result in increased accuracy in the microwave snow accumulation metric.

For this study, vertically polarized, enhanced resolution, 'egg' gridded, σ° measurements were used for two reasons: 1) to simplify the microwave snow accumulation model by using a single polarization in each of the three steps of the

retrieval algorithm, and 2) to facilitate future multiple frequency comparisons between QuikSCAT, or the similar Ku-band OSCAT, and the C-band ASCAT which operates exclusively at VV with an 'egg' gridding. Multiple frequency, multiple incidence angle retrievals acquired from satellite borne scatterometers with overlapping orbital passes offers the potential to gain an increased understanding of the extinction coefficient, given differences in penetration depth associated with differences in wavelength, and differences in path length through the snowpack associated with differences in incidence angle.

On the basis of the previous discussion, the microwave snow accumulation metric was retrieved using, annual σ° time series constructed from image data acquired over the time period 1999-2009. Time series were constructed alternating vertically polarized, morning and evening, enhanced resolution, 'egg' gridded, σ° measurements defined by $\sigma_v^\circ(t)$. Regions that experienced seasonal melt-refreeze metamorphosis and the potential formation of dominant scattering layers were defined spatially by the microwave melt model, using $I_{\chi,mask}$, and temporally by the Markov model using t_{freeze} and t_{melt}. Year 1999 and 2000 were not considered in this analysis because of an error in the algorithm that gave inaccurate snow accumulation estimates, but should be considered in future research.

Example time series of $\sigma_v^\circ(t)$ and $M(t)$ over the time period 1999-2009 for a pixel in the percolation zone in southwestern Greenland containing Crawford Point (Figure 7) are given in Figure 11 A and B. Backscatter time series are vertically polarized, morning and evening, enhanced resolution, 'slice', σ° measurements generated by the SIR algorithm. Blue and green arrows in $\sigma_v^\circ(t)$ identify $\Delta\sigma_{fs}^\circ$. The green arrow identifies a multiyear snow accumulation signature. The red arrow in.

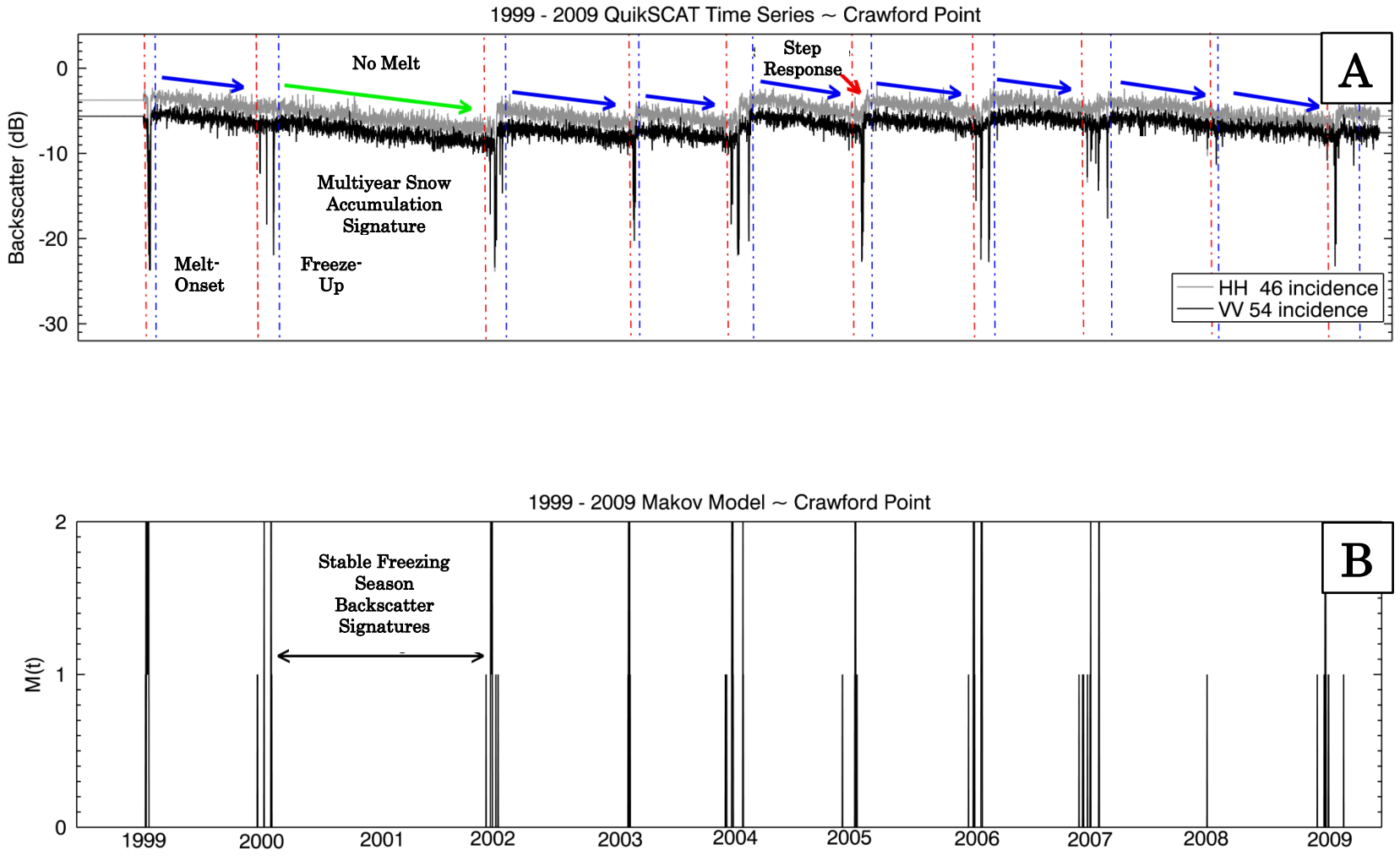

Figure 11. QuikSCAT Backscatter Time Series and Markov Time Series
Time series of $\boldsymbol{\sigma^{\circ}_{v}(t)}$(A) and $\boldsymbol{M(t)}$(B) for a pixel in the southwestern percolation zone containing Crawford Point.

$\sigma_v^\circ(t)$ identifies a step response indicating the formation of a new dominant scattering layer. The blue and red dotted lines in $\sigma_v^\circ(t)$ identify freeze-up and melt-onset as detected by the Markov model and identified by the black arrow in $M(t)$

4.5 Microwave Snow Accumulation Metric vs. Snow Accumulation Rates

This section provides a pixel-by-pixel comparison between the microwave snow accumulation metric retrieved using the microwave snow accumulation model and snow accumulation rates on the Greenland ice sheet acquired from the Polar MM5 mesoscale climate model and spatially calibrated. Construction of snow accumulation rates and the calibration procedure are provided. A simple empirical relationship is derived and results of this comparison are analyzed to determine the potential for large-scale mapping of freezing season snow accumulation rates using the retrieval technique.

4.5.1 Snow Accumulation Data

For comparison with the microwave snow accumulation metric, spatially calibrated Polar MM5 snow accumulation rates were constructed from monthly Polar MM5 solid precipitation output (provided courtesy of Dr. Jason Box). Snow accumulation, C, is defined in units of m w. e. by

$$C = P_{solid} + P_{liquid} + Q_S + E \tag{9}$$

where P_{solid} is defined as solid precipitation, P_{liquid} is defined as retained liquid precipitation, Q_S is defined as surface water vapor flux, and E is defined as blowing snow sublimation [*Box et al*, 2006].

Burgess et al. [2010] spatially calibrated annual Polar MM5 P_{solid} output using snow accumulation data from 133 in situ sites (Figure 2) acquired from four sources: 1) NASA Program for Arctic and Regional Climate Assessment (PARCA) ice cores [*Bales et al.*, 2001a; *Hanna et al.*, 2005; *Mosley-Thompson et al.*, 2001], 2) recent non-PARCA cores [*Hanna et al.*, 2005], 3) coastal meteorological station data [*Ohmura et al.*, 1999], and 4) pre-PARCA cores tabulated by *Bales et al.* [2001a]. For this study, monthly P_{solid} output from the Polar MM5 [Box et al., 2004, Box et al., 2006; Bromwich et al., 2001; Cassano et al, 2001] over the time period 1999-2009 was acquired. Locations of in situ point measurements of snow accumulation are shown in Figure 3. P_{solid} output was originally run with a 24-kilometer^2 horizontal grid resolution and mapped in a polar stereographic projection. The annual spatial calibration derived in [*Burgess et al.*, 2010] was applied (courtesy of Dr. Jason Box) to monthly P_{solid} output with the given annual regression constant divided by 12, which assumes that the correction offset does not vary with month. Q_S and E are implicitly accounted for in the calibration procedure [*Burgess et al.*, 2010]. P_{liquid} is neglected, however, and was estimated to comprise less than 1% of net snow accumulation [Box et al., 2004].

Spatially calibrated monthly Polar MM5 snow accumulation data were mapped in a Lambert azimuthal equal area projection[19] and then resampled in a SIR formatted 'egg' gridding with a final resolution of 24 kilometers^2. Resampling to the enhanced resolution of the scatterometer data provided no additional snow accumulation information, so the lower resolution was chosen for comparisons. Data

[19] calculated using a local Earth radius centered over the Greenland ice sheet

were ice masked (http://bprc.osu.edu/wiki/Jason_Box_Datasets) using a MODIS derived land surface classification which identifies permanent ice cover on the Greenland ice sheet (ice mask provided courtesy of Dr. Jason Box) and then expanded into twice daily estimates by dividing the total monthly snow accumulation rate by the total number of days in each month multiplied by two, resulting in the same temporal resolution as the microwave snow accumulation metric

Regions that experienced seasonal melt-refreeze metamorphosis and the potential formation of scattering layers were defined spatially by the microwave melt model, using $I_{\chi,mask}$, and temporally by the Markov model using t_{freeze} and t_{melt}, both calculated using $\sigma_v^\circ(t)$. A cumulative snow depth in m w.e accumulated from t_{freeze} to t_{melt} was approximated pixel-by-pixel, by summing spatially calibrated monthly Polar MM5 snow accumulation rates over Δt_{fs}.

Given the averaging scheme and the monthly temporal resolution of the Polar MM5 snow accumulation data, the expansion procedure may result in a bias if a large snowfall event occurs prior to t_{freeze} or following t_{melt} within a given month. This bias was assumed present, but likely small. For this general comparison, expanded, spatially calibrated Polar MM5 snow accumulation rates were assumed a reasonable estimate for C.

4.5.2 Empirical Relationships

Annual comparisons were made between freezing season σ° decreases, $\Delta\sigma_{fs}^\circ$, in units of dB (Figure 12), and spatially calibrated Polar MM5 snow accumulation

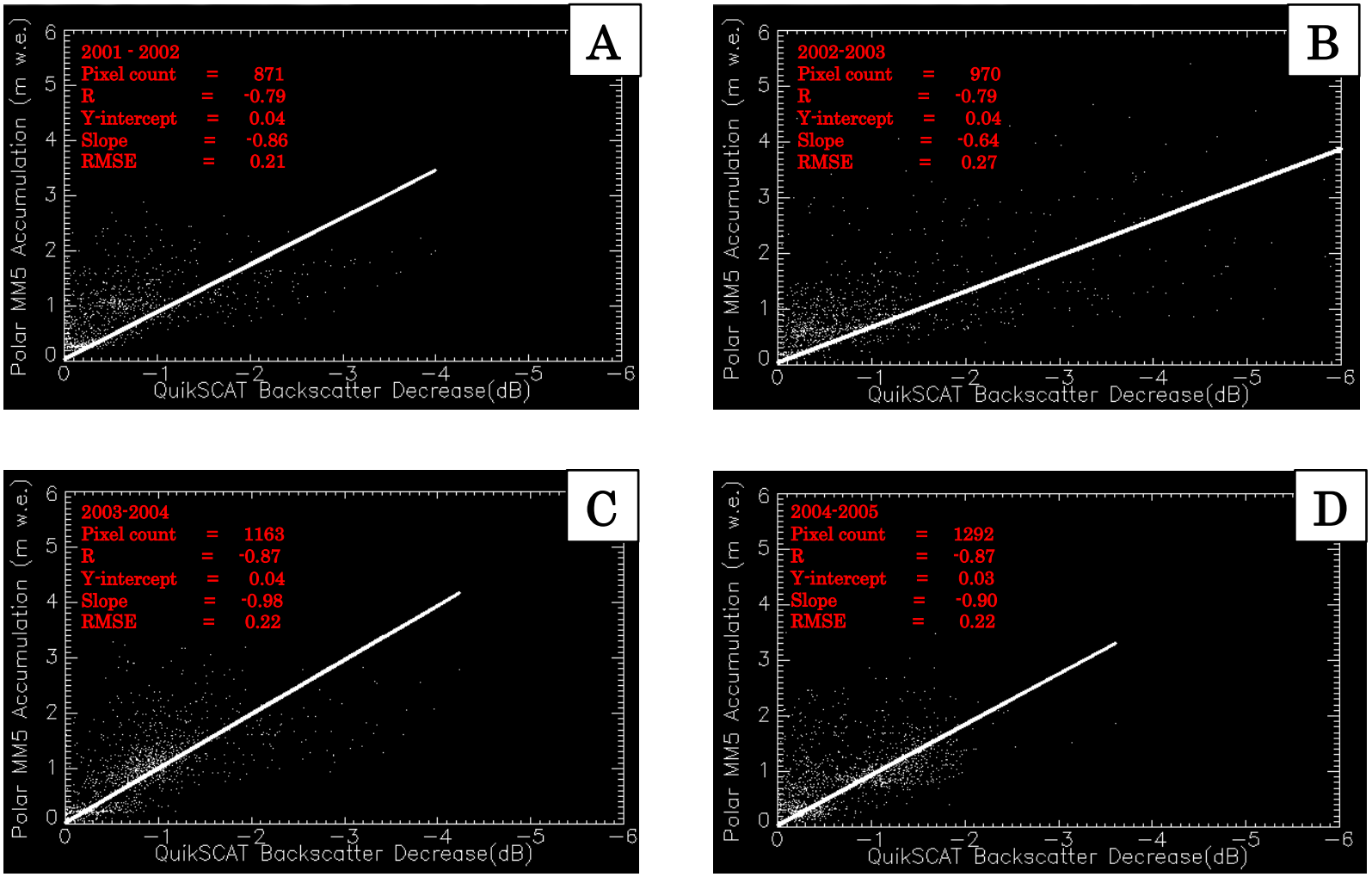

Figure 12. Microwave Snow Accumulation Metric vs. Snow Accumulation Rates
Scatterplots $\Delta\sigma^{\circ}_{fs}$ versus C (2001-2009).

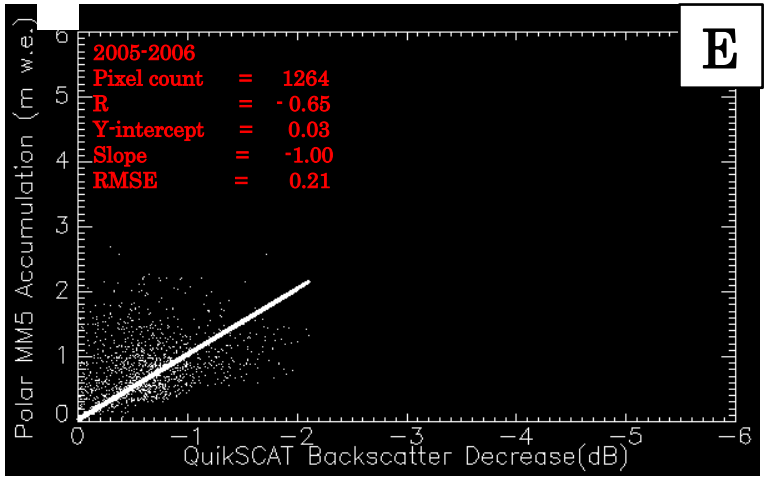

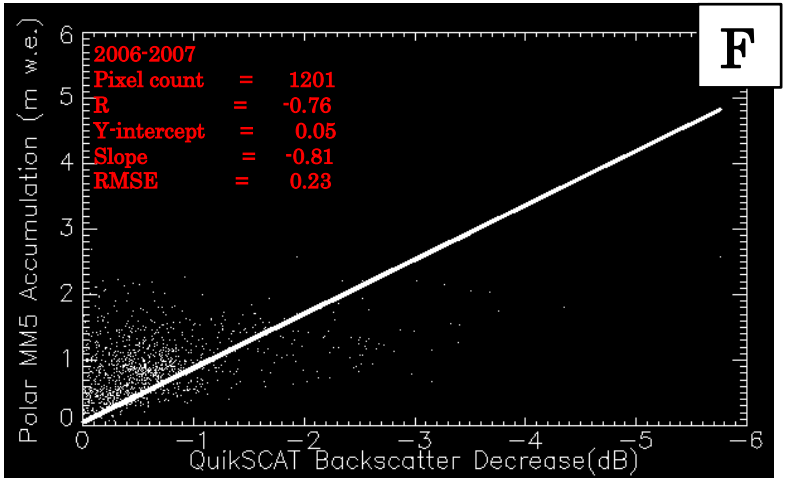

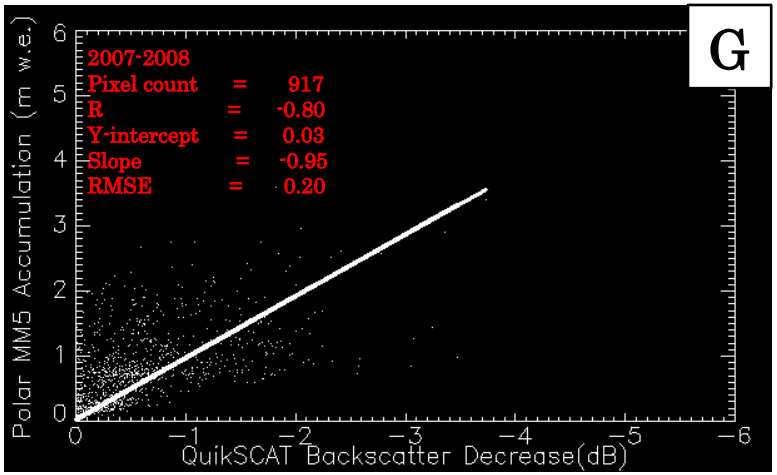

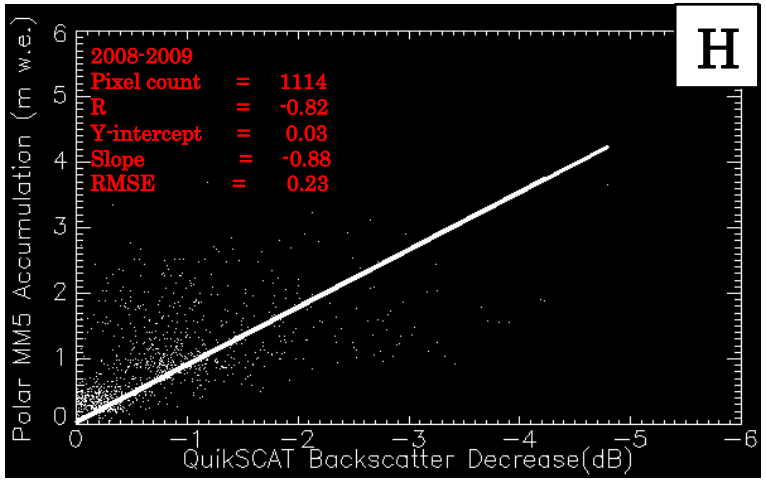

Figure 12. Continued

rates, C, in units of m w.e., for each year in the 2001-2009 QuikSCAT time series. A reasonably strong inverse linear relationship exists between each of the compared data sets for all years defined by least squares linear fit lines in each of the Figures 12 A-H. The total initial masked ice sheet area was 1.73 x 10^6 kilometers^2 equivalent to 2768pixels, subsequently annually reduced to the number of pixels in$I_{\chi,mask}$. The number of comparison points obtained for $\Delta\sigma^\circ_{fs}$ for each year ranged from 871 to 1292 samples, corresponding to respective areas of 7.60 x 10^6 kilometers^2 to 8.10 X 10^6 kilometers^2. Correlation coefficient values ranged from -0.76 to -0.89, and RMS errors ranged from 0.20 to 0.27 m w.e. The regression residual range was -4.25 to 2.52 m w.e

The fit line intercepts remained relatively stable, and ranged from 0.02 m w.e to 0.05 m w.e, suggesting the linear model is well calibrated for low $\Delta\sigma^\circ_{fs}$ values versus low C values corresponding to the northeastern percolation, wet snow, and ablation zones and the southwestern ablation zone. Clustering near the fit line was observed in Figures 12 C, D, G, and H. This result is similar to the Greenland ice sheet dry snow zone study by *Forster et al.* [1999] which suggests σ° measurements have increased sensitivity to changes in snow accumulation rates when the average snow accumulation rate is low. More recent Antarctic ice sheet dry snow zone studies by *Dierking et al.* [2012] and *Rotschky et al.* [2006] show similar results. The linear model is also well calibrated for moderate $\Delta\sigma^\circ_{fs}$ values versus moderate C values corresponding to the higher elevation southeastern percolation zone. Clustering near the fit line was observed in Figures 12 C, F, and H.

Fit line slopes ranged from -0.64 to 1.00 m w.e. / $\Delta\sigma^\circ_{fs}$ controlled by two types of regionally dependent model biases which produced significant calibration errors:

1) low to moderate $\Delta\sigma^{\circ}_{fs}$ values versus high C values which correspond to the southwestern wet snow zone and the lower elevation southeastern percolation zone (northern), and 2) high $\Delta\sigma^{\circ}_{fs}$ values versus low to moderate C values which correspond to the lower elevation southeastern percolation zone (southern). High C values and low to moderate $\Delta\sigma^{\circ}_{fs}$values resulted in larger negative fit line slopes (Figure 12 E). High $\Delta\sigma^{\circ}_{fs}$ values and low C values resulted in smaller negative fit line slopes (Figure 12 F). These two model biases are likely linked to snow accumulation rates, as well as snowpack stratigraphy in the underlying ice-facie which significantly influences the microwave scattering mechanism.

The largest RMS error of 0.27 and the upper and lower limit of the residual range correspond to Figure 12 B. The 2002-2003 freezing season was anomalous, characterized by a relatively high pressure system over the Norwegian Sea and a relatively low pressure system southeast of the high-elevation southern tip of Greenland. This blocking pattern resulted in a synoptic scale atmospheric circulation pattern that delivered abnormally large and frequent storms to southeastern Greenland and produced increased precipitation along the southeastern coast. Fewer southwestern storms and precipitation shadow effects produced relatively low precipitation in southwestern Greenland [*Box et al.*, 2005]. The scatterplot shown in Figure 12 B displays a large spread in the comparison points which results in two distinct differences between Figure 12 B and the other scatterplots in the 2001-2009 QuikSCAT time series, Figures 12 A, C, D, E, F, G, and H. The first difference is related to $\Delta\sigma^{\circ}_{fs}$ values exceeding ~4.5 dB versus C values ranging from ~1.0 m w.e. to ~5.0 m w.e. The second difference is related to C values exceeding ~4.0 m w.e versus $\Delta\sigma^{\circ}_{fs}$ values ranging from ~0.1 dB to ~6.0 dB.

These comparison points correspond to the region of the precipitation anomaly, southeastern wet snow zone and lower elevation percolation zone.

On the basis of the observed relationships in Figures 12 A-H, two additional comparisons were made between $\Delta\sigma^{\circ}_{fs}$ and C (Figure 13): 1) comparisons between all samples (Figure 13 A), and 2) comparisons between all points in all years in the QuikSCAT time series except the anomalous 2002-2003 freezing season, equivalent to 9013 samples (Figure 13 B). The second comparison resulted in a slightly higher negative correlation coefficients value (-0.81 to -0.82) and a slightly smaller slope (-0.92 to -0.85 m w.e. / $\Delta\sigma^{\circ}_{fs}$), y-intercept (0.04 to 0.03 m w.e) and RMS error (0.22 to 0.21) and a reduced residual range (-4.25 to 2.52 m w.e to -2.24 to 2.07 m w.e.).

On this basis, a simple linear model was derived to retrieve a snow accumulation estimate using all points in all years in the QuikSCAT 2001-2009 time series, excluding the anomalous 2002-2003 freezing season. The inverse linear relationship is defined by the least squares linear fit line with an equation given by

$$\mathrm{C} = 0.03 - 0.85\Delta\sigma^{\circ}_{fs} \tag{10}$$

Snow accumulation rates were estimated over the time period 2001 – 2009 using the linear model defined by equation 10, and $\Delta\sigma^{\circ}_{fs}$ calculated using $\sigma^{\circ}_{v}(t)$. Mapped comparisons between QuikSCAT-derived snow accumulation estimates and spatially calibrated Polar MM5 snow accumulation estimates are shown in Figure 14 A-H. Mapped regression residuals calculated using equation 10 are shown in Figure 15.

.

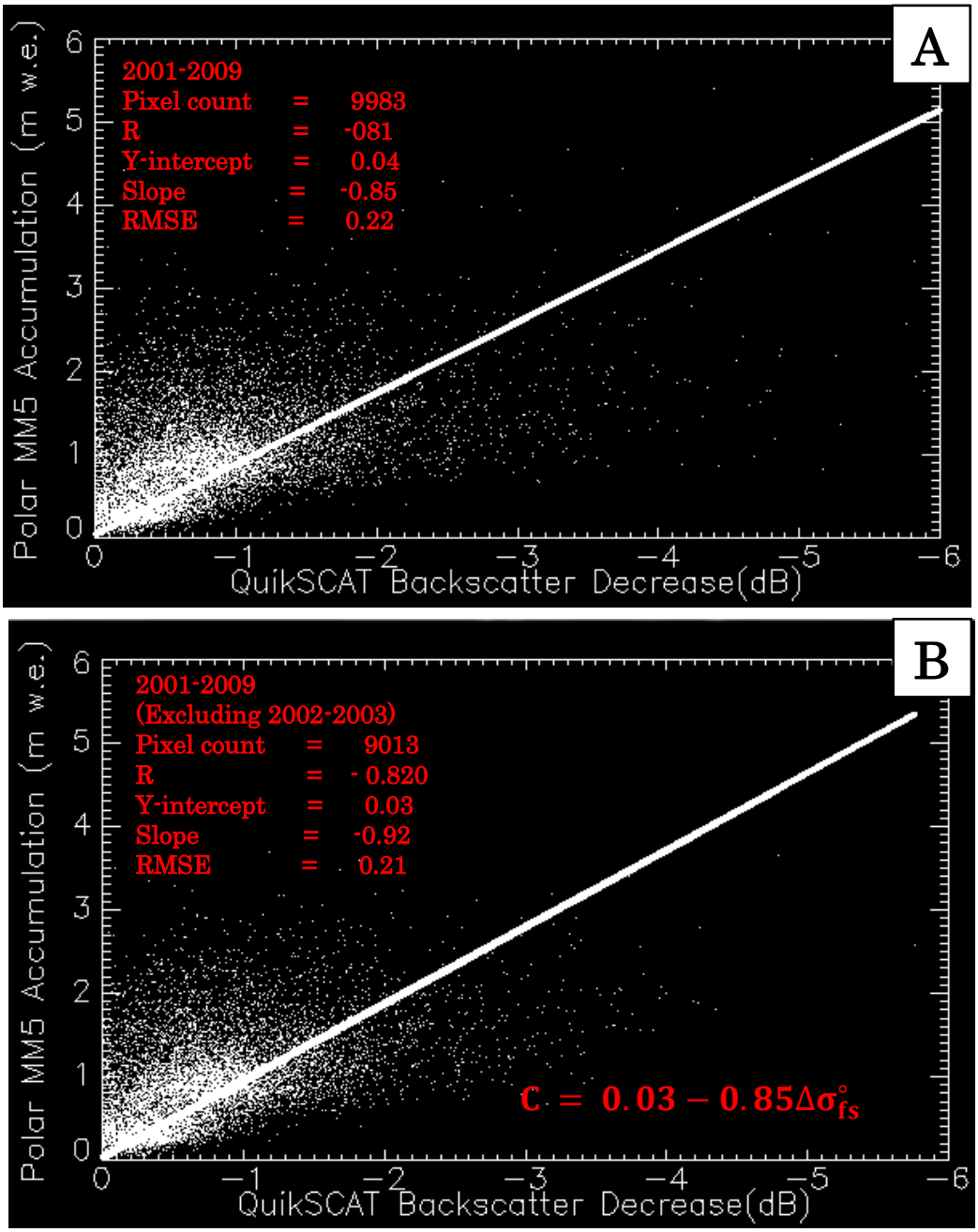

Figure 13. Scatterplot Comparison
Scatterplot comparison between all points in all years in the 2001-2009 QuikSCAT time series (A), and comparisons between all points in all years in the QuikSCAT time series excluding the anomalous 2002-2003 freezing season (B). The microwave snow accumulation model is defined by the linear equation C.

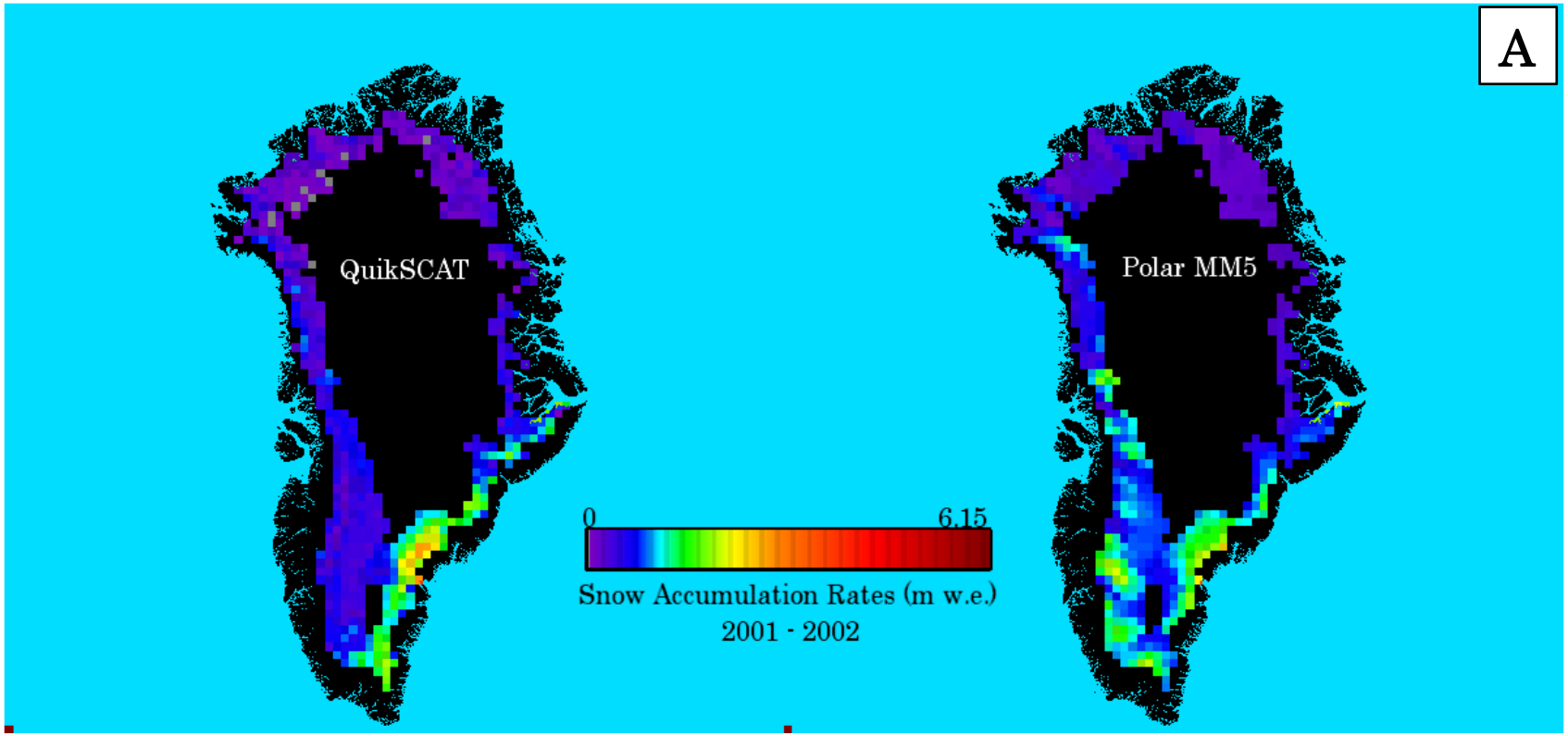

Figure 14. Microwave Snow Accumulation Model vs. Polar MM5
Comparisons between microwave snow accumulation model and spatially calibrated Polar MM5 snow accumulation rates.

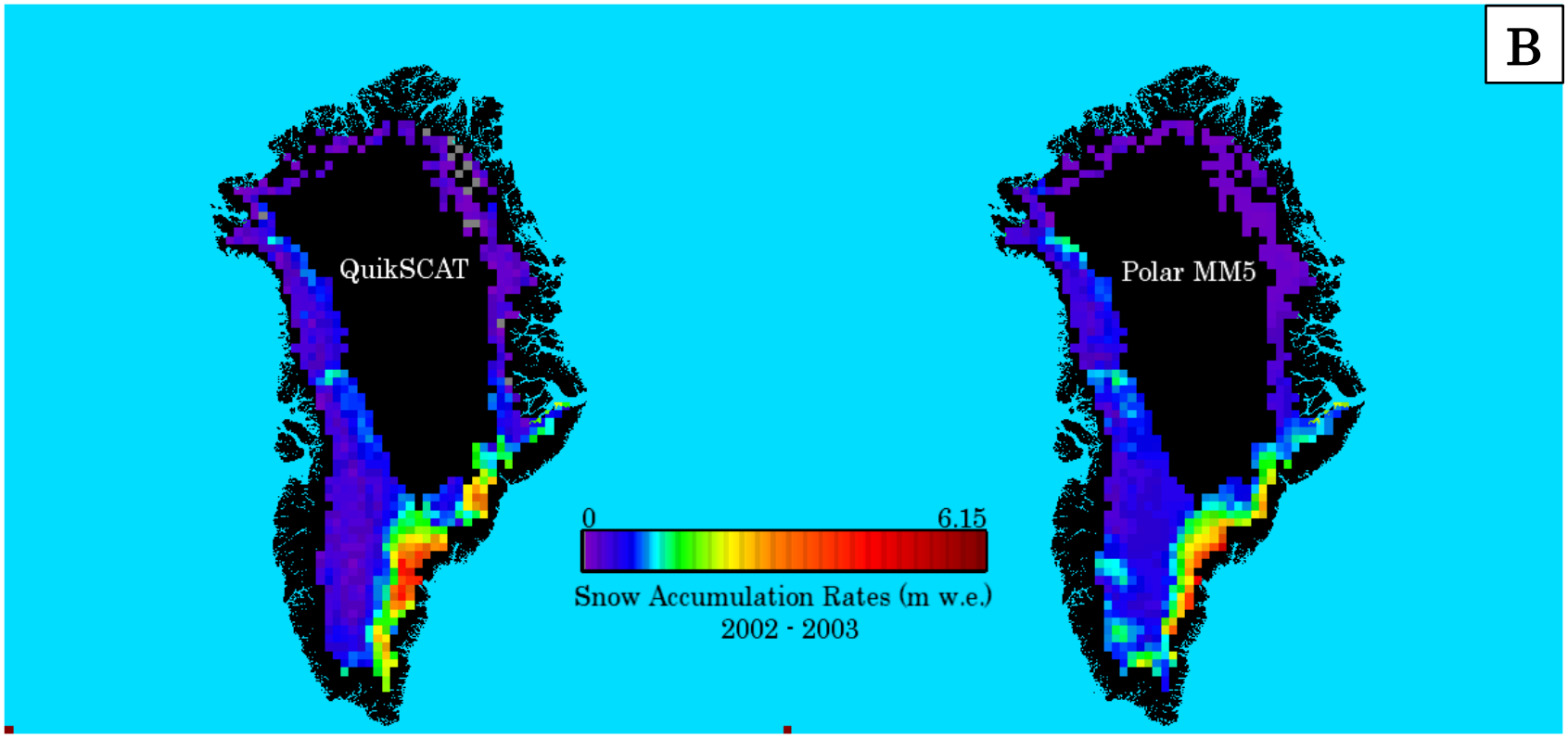

Figure 14. Continued

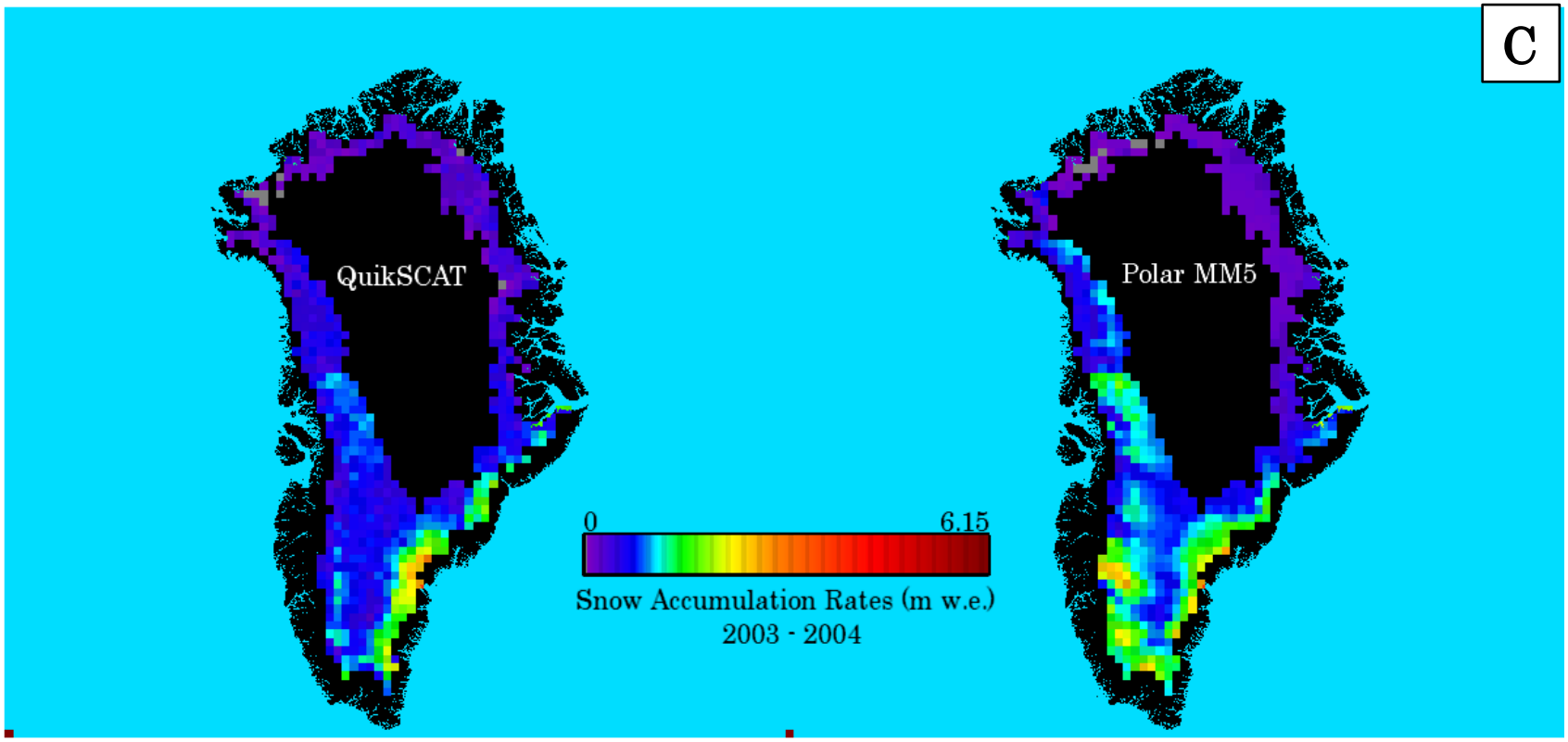

Figure 14. Continued

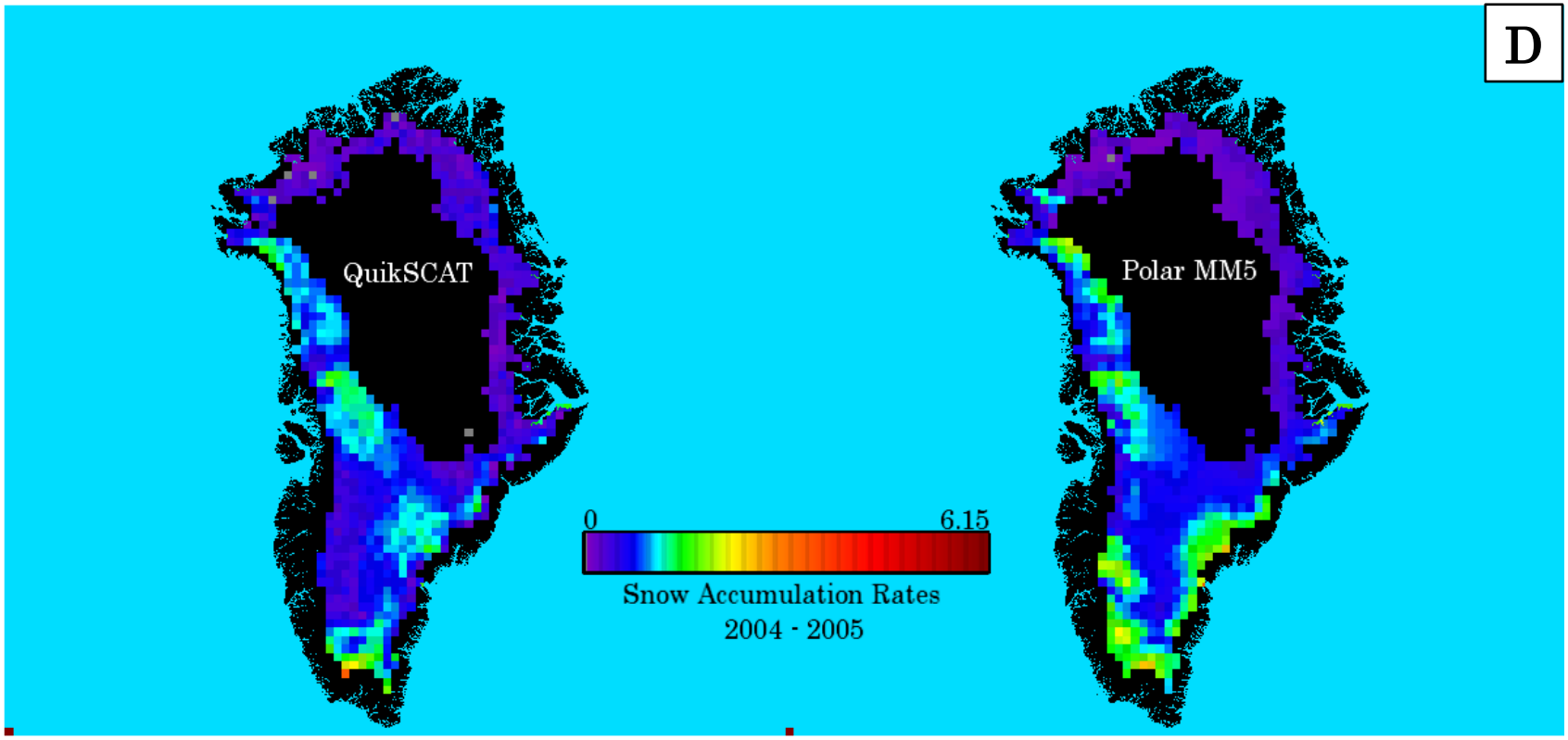

Figure 14. Continued

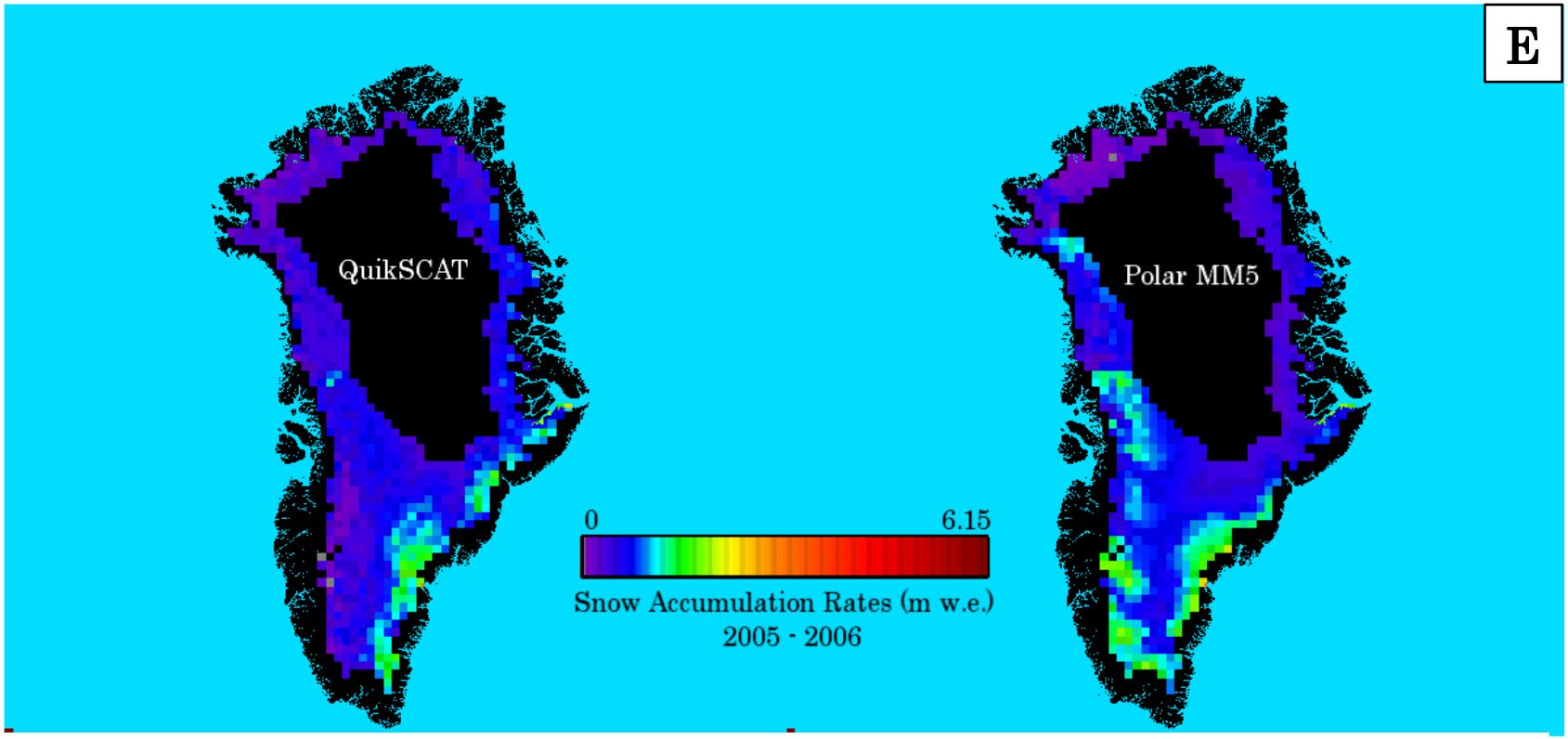

Figure 14. Continued

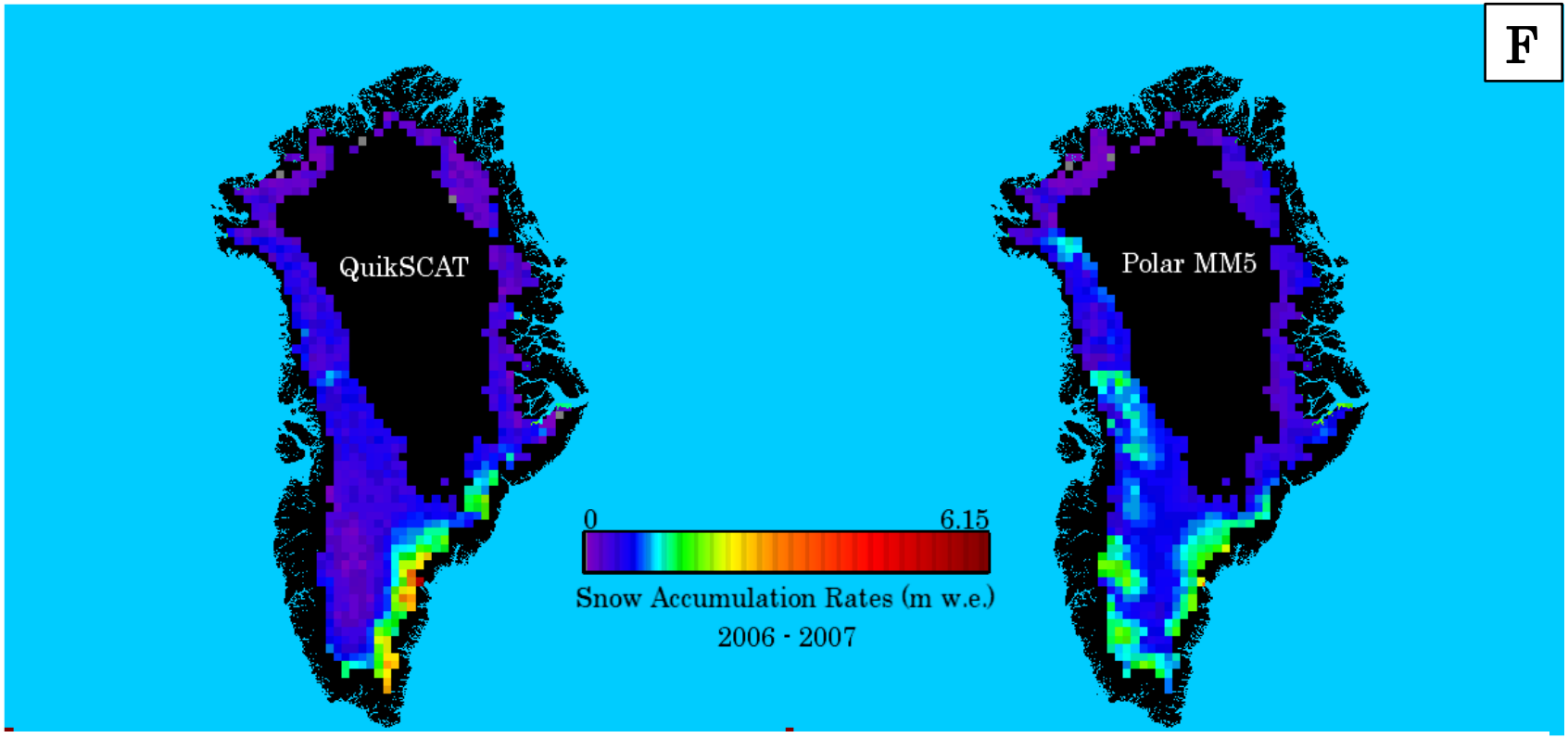

Figure 14. Continued

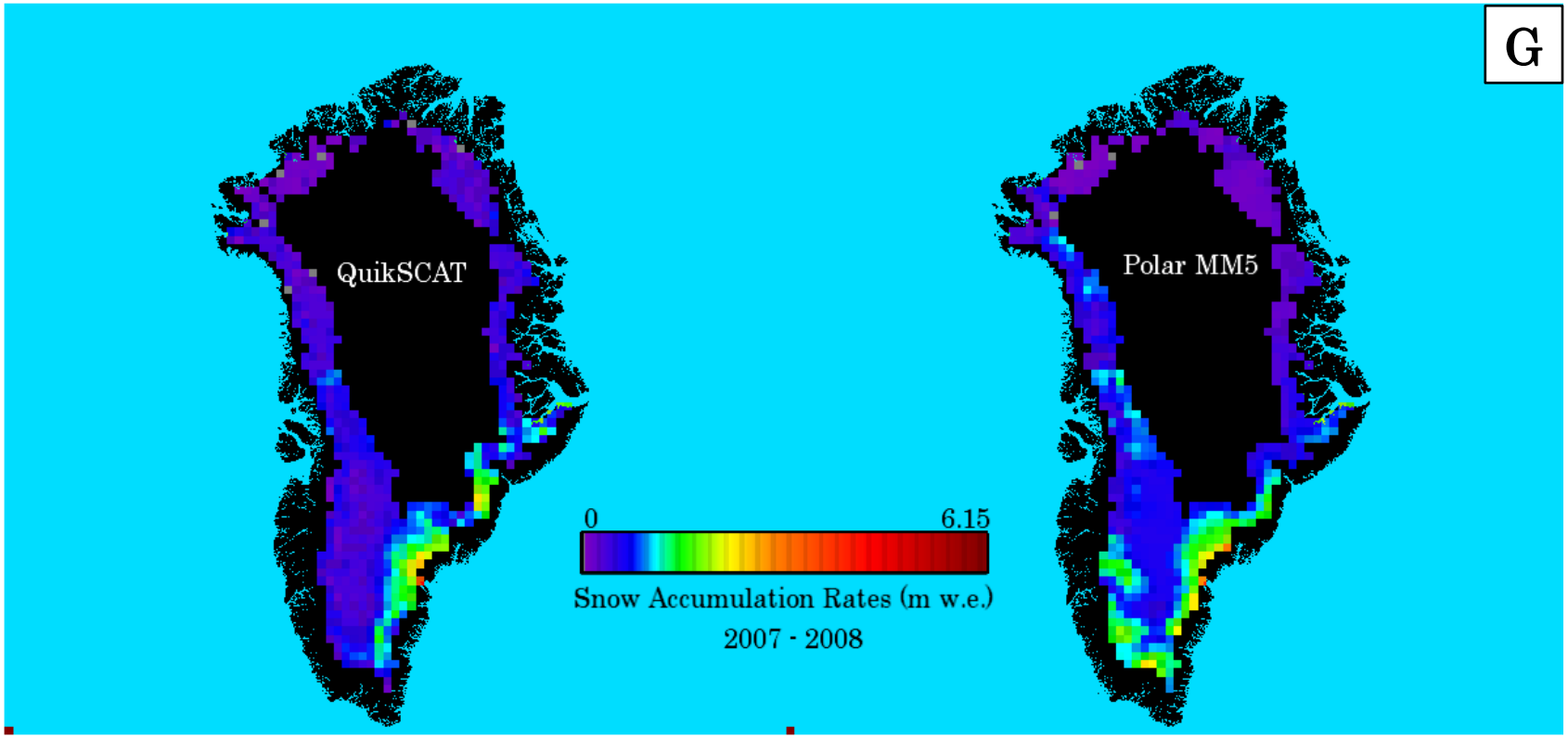

Figure 14. Continued

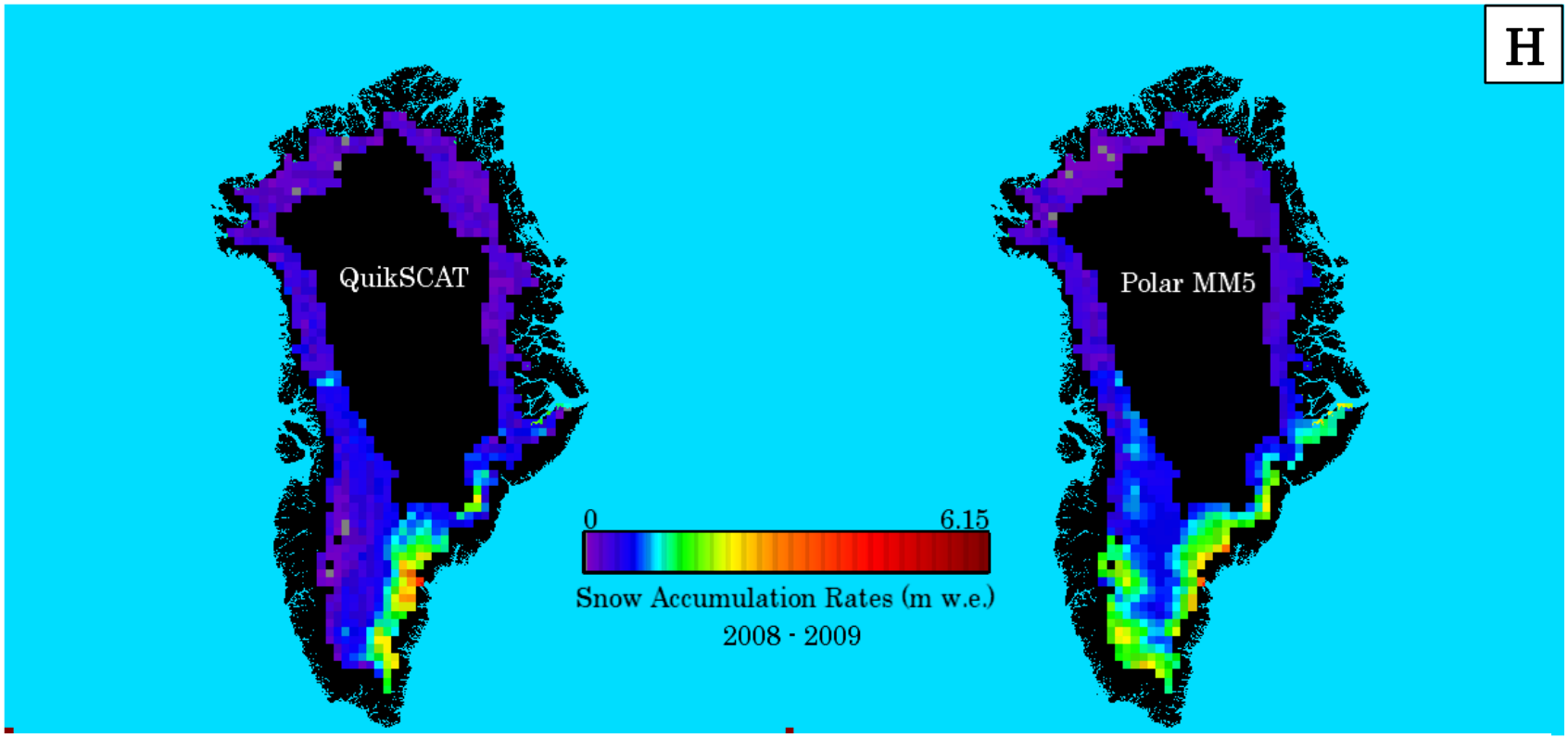

Figure 14. Continued

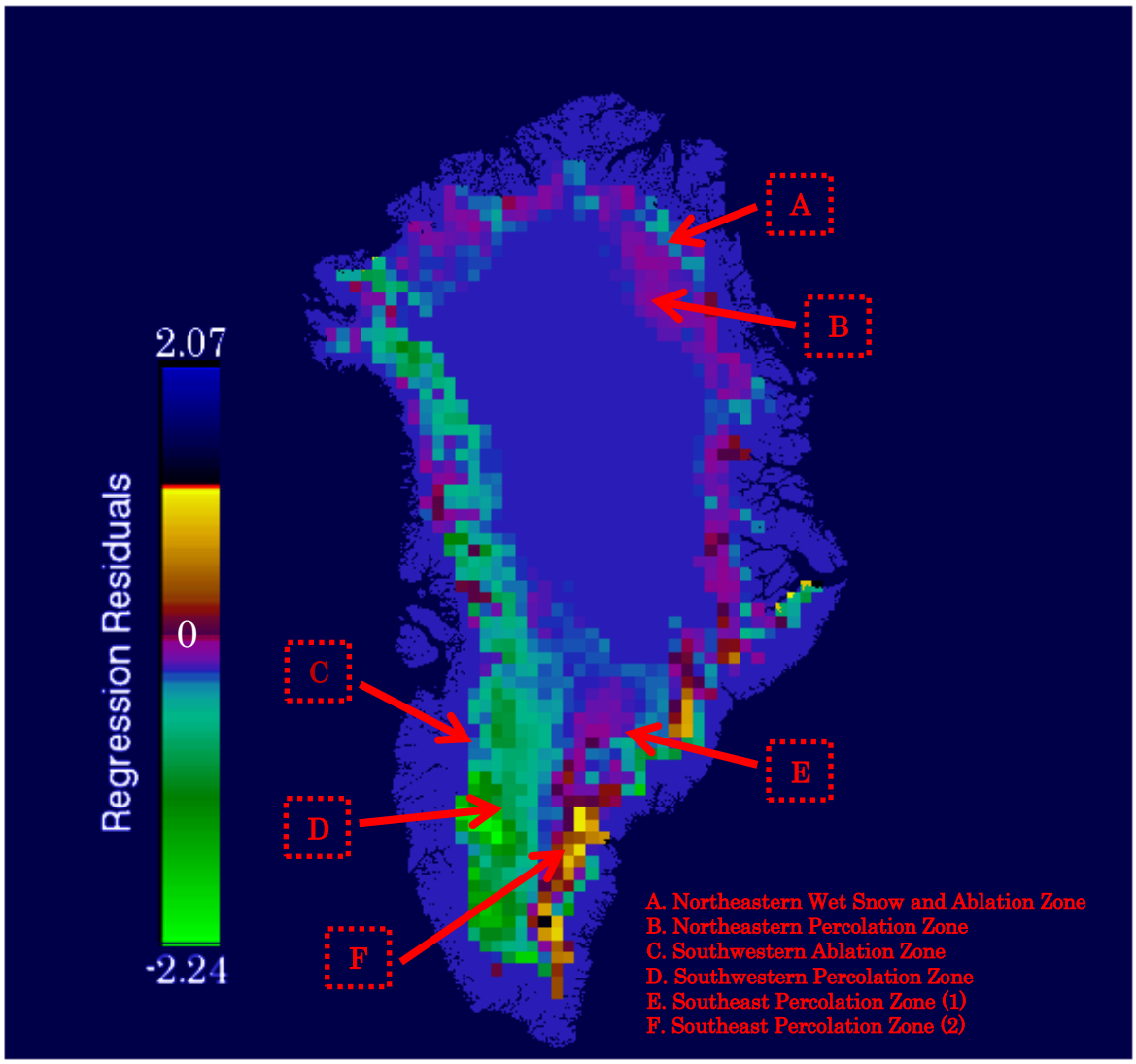

Figure 15. Microwave Snow Accumulation Model Regression Residuals
Positive and negative regression residuals calculated from the microwave snow accumulation model representing overestimates and underestimates in snow accumulation rates in the percolation zone, the wet snow zone, and ablation zone.

4.6. Northeastern Ablation Zone and Wet Snow Zone

The northeastern wet snow and ablation zones are characterized by small positive residual values which result in small overestimates in the cumulative snow depth (m w. e.) in this region, defined by C (Figure 15 A). Differences between the northeastern wet snow zone and the northeastern ablation zone are observed within σ° signatures; however, residuals calculated in the two ice-facies are similar. The underlying ice-facie in the northeastern ablation zone is characterized by a dominant scattering layer consisting of glacial ice, with glacial features such as, cryoconite holes and crevasses which may appear rough relative to the incident wavelength. Frozen superglacial lakes and streams, which may appear smooth relative to the incident wavelength, are also present. The underlying ice-facie in the northeastern wet snow zone is characterized by a dominant scattering layer formed by melt-refreeze metamorphosis, which may also appear rough relative to the incident wavelength. In the higher elevations of the wet snow zone, iced firn layers, ice pipes, ice glands, and ice lenses are interspersed with patches of snow and firn [*Cuffey and Paterson*, 2010]. Downglacier from the snow line, iced firn layers merge to form a continuous layer of superimposed ice [*Cuffey and Paterson*, 2010]. The overlying layer of snow accumulation in this region likely has relatively large mean snow grain sizes resulting from low annual snowfall rates (Figure 1 and Figure 3). Exposure at the surface followed by dry snow metamorphosis changes snow grain shapes, increases snow grain sizes, and increases bonding between individual snow grains [*Cuffey and Paterson*, 2010].

A Mie scattering response from the underlying high density dominant scattering layer is assumed. Surface scattering may contribute to the net response if

the surface of the ice-facie is sufficiently rough relative to the incident wavelength. A specular surface scattering response, which reflects the EM wave away from the scatterometers antenna, may also contribute to the net response in the ablation zone if the ice-facie is sufficiently smooth relative to the incident wavelength. Larger mean snow grain sizes likely contribute to an increased Raleigh scattering response from the overlying layer of snow accumulation. Given that in the ablation zone, the entire annual layer of snow accumulation is removed by ablation, penetration depth is limited to the current year's annual layer of snow accumulation. In the wet snow zone, penetration depth is also likely limited to the current year's annual layer of snow accumulation by the high density of large ice-scatterers in the underlying dominant scattering layer as well as by large mean snow grain sizes within the annual layer of snow accumulation.

4.7 Northeastern Percolation Zone

Moving upglacier from the northeastern wet snow and ablation zone to the northeastern percolation zone, positive residual values increase which results in increases in the overestimation of C in this region (Figure 15 B). The transition from a spatially continuous higher density underlying ice-facie of wet snow zone ice-scatterers to a spatially discontinuous lower density underlying ice-facie of percolation zone ice-scatterers likely contributes to the increases in overestimates. The underlying ice-facie in the northeastern percolation zone is characterized by a dominant scattering layer consisting of ice layers, ice pipes, ice glands, and ice lenses with differing orientations, sizes, and shapes embedded at differing depths within a sequence of annual layers of snow accumulation, each with differing snow

grain sizes, densities, and layer thicknesses. Similar to the northeastern ablation and wet snow zone, the overlying layer of snow accumulation in this region likely has relatively large mean snow grain sizes resulting from low annual snowfall rates. Stratification may also occur within the sequence of annual layers of snow accumulation if vapor transport and sublimation results in a dry snow metamorphosis and surface of depth hoar layers are formed during the freezing season.

As compared to the northeastern ablation and wet snow zones, a decreased Mie scattering response from the underlying lower density dominant scattering is assumed. Surface scattering may contribute to the net response if the surface of the ice-facie is sufficiently rough relative to the incident wavelength. Surface scattering from dielectric interfaces between stratified layers may also contribute to the net response by reflecting the EM wave away from the scatterometers antenna [*West et al.*, 1996]. Similar larger mean snow grain sizes likely result in a similar Raleigh scattering response from the overlying layer of snow accumulation. Penetration depth likely increases, resulting from a decrease in the density of ice-scatterers within the snowpack, potentially, within multiple annual layers of snow accumulation.

4.8 Southwestern Ablation Zone

Similar to the northeastern wet snow and ablation zones, the southwestern ablation zone is characterized by positive residual values which result in the overestimation of C in this region (Figure 15 C). The underlying ice-facie in the southwestern ablation zone is characterized by a dominant scattering layer of glacial

ice with cryoconite holes, crevasses, and frozen superglacial lakes and streams. The overlying layer of snow accumulation in this region likely has relatively large mean snow grain sizes resulting from low annual snowfall rates (Figure 1 and Figure 3).

A Mie scattering response from the high density underlying dominant scattering layer is assumed and surface scattering may contribute to the net response if the surface of the ice-facie is sufficiently rough or smooth relative to the incident wavelength. Larger mean snow grain sizes likely contribute to an increased Raleigh scattering response from the overlying layer of snow accumulation. Penetration depth is limited to the current year's annual layer of snow accumulation.

4.9 Southwestern Wet Snow Zone

Moving upglacier from the southwestern ablation zone to the southwestern wet snow zone, residual values make a sign change from positive to negative which results in the underestimation of C in this region. Negative residual values increase with increasing snow accumulation rates, resulting in the increased underestimation of C (Figure 15 D). The transition from an underlying ice-facie of glacial ice to an underlying layer of wet snow zone scatterers likely contributes to the residual value sign change. Similar to the northwestern wet snow zone, the underlying ice-facie in the southwestern wet snow zone is characterized by a dominant scattering layer consisting of iced firn layers, ice pipes, ice glands, ice lenses, and superimposed ice. Snow grain sizes within the overlying layer of snow accumulation in this region likely range from relatively large mean snow grain sizes in regions with low snowfall rates to relatively small mean grain sizes in regions

with higher snowfall rates (Figure 1 and Figure 3). Stratification may also occur within the snowpack.

As compared to the southwestern ablation zone, an increased Mie scattering response from the underlying high density dominant scattering layer is assumed. Surface scattering may contribute to the net response if the surface of the ice-facie is sufficiently rough, or if stratification occurs within the snowpack. Variable mean snow grain sizes likely contribute to a variable Raleigh scattering response from the overlying layer of snow accumulation. The Raleigh scattering response is increased in regions that experience relatively low snow accumulation rates. As regional snow accumulation rates increase and mean snow grain sizes decrease, the Raleigh scattering response decreases and sensitivity to the overlying layer of snow accumulation is reduced. Penetration depth is likely limited to the current year's annual layer of snow accumulation by the high density of large ice-scatterers in the underlying dominant scattering layer as well as by large mean snow grain sizes within the annual layer of snow accumulation.

4.10 Southeast Percolation Zone (1)

Similar to the northeastern percolation zone, the southeastern percolation zone (1) is characterized by negative residual values which result in the underestimation of C in this region. Negative residual values increase with increasing snow accumulation rates, resulting in the increased underestimation of C (Figure 15 E). The underlying ice-facie in the southeastern percolation zone is characterized by a dominant scattering layer of ice layers, ice pipes, ice glands, and ice lenses within a sequence of annual layers of snow accumulation. The overlying

layer of snow accumulation in this region likely has relatively small mean snow grain sizes resulting from high snowfall rates (Figure 1 and Figure 3). Stratification, however, may occur within the snowpack during the freezing season, increasing the mean snow grain size.

A Mie scattering response from the underlying high density dominant scattering layer is assumed and surface scattering may contribute to the net response if the surface of the ice-facie is sufficiently rough, or if stratification occurs within the snowpack. Smaller mean snow grain sizes likely contribute to a Raleigh scattering response with reduced sensitivity to the overlying layer of snow accumulation. As snow accumulation rates increases, the sensitivity of the Raleigh scattering response decreases. Penetration depth is likely limited to the current year's annual layer of snow accumulation by the high density of large ice-scatterers in the underlying dominant scattering layer.

4.11 Southeast Percolation Zone (2)

Moving upglacier from the southeastern percolation zone (1) to the southeastern percolation zone (2), residual values make a sign change from positive to negative, which results in the overestimation of C in this region. Positive residual values increase with increasing snow accumulation rates, resulting in the increased underestimation of C (Figure 15 F). The underlying dominant scattering layer transitions from higher density ice-scatterers in the southeastern percolation zone (1) to lower density ice-scatterers in the southeastern percolation zone (2) of percolation zone ice-scatterers, which likely contributes to underestimates. The

overlying layer of snow accumulation in this region likely has relatively small mean snow grain sizes, which increase if stratification occurs.

As compared to the southeastern percolation zone (1), a decreased Mie scattering response from the underlying lower density dominant scattering layer is assumed. Surface scattering may contribute to the net response if the surface of the ice-facie is sufficiently rough, or if stratification occurs within the snowpack. Similar snow accumulation rates and larger snow grain sizes likely result in a Raleigh scattering response with reduced sensitivity to the overlying layer of snow accumulation. Penetration depth likely increases, resulting from a decrease in the density of ice-scatterers within the snowpack, potentially, within multiple annual layers of snow accumulation.

4.12 Conclusions and Future Work

Results of the microwave snow accumulation model presented in Chapter 4 demonstrate that a reasonably strong inverse linear relationship exists between decreasing freezing season σ° signatures and spatially calibrated Polar MM5 snow accumulation rates in regions of the Greenland Ice Sheet that experience seasonal melt-refreeze metamorphosis and form dominant scattering layers, with a calculated correlation coefficient of -0.82 and a mean RMS error of 0.22 m w.e. However, while the general spatiotemporal variability of snow accumulation on the Greenland ice sheet is observed in Figure 14 A-H, this retrieval technique fails to retrieve accurate snow accumulation rates.

Regression residuals indicate that decreasing freezing season σ° signatures are a function of snow accumulation rates as well as snowpack stratigraphy in the

underlying ice-facie. Both positive and negative residuals, corresponding to overestimates and underestimates in snow accumulation rates, increase with increasing snow accumulation rates, suggesting σ° measurements have increased sensitivity to changes in snow accumulation rates when the average snow accumulation rate for the region is low. This is likely the result of an increased Raleigh scattering response from larger mean snow grain sizes. Penetration depth is reduced, which decreases volume scattering, attenuation, and extinction of the EM wave within the layer of snow accumulation, which subsequently increases the σ° measurement, resulting in smaller freezing season σ° decreases. As mean snow grain sizes decrease with increased snow accumulation rates, the sensitivity of the σ° measurement to changes in snow accumulation rates also decreases. This is likely the result of a decreased Raleigh scattering response from smaller mean snow grain sizes. Penetration depth is increased, resulting in increased volume scattering, attenuation, and extinction of the EM wave within the layer of snow accumulation, which subsequently decreases the σ° measurement, resulting in larger freezing season σ° decreases.

The relationship between freezing season σ° signatures and snow accumulation rates is further controlled by differences in the density of the underlying dominant scattering layer, which influences the Mie scattering response, and to a lesser extent, differences in surface roughness, which influences the surface scattering response.

In regions with higher density underlying scattering layers, the spread in comparison points ranges from lower to moderate $\Delta\sigma^\circ_{fs}$ values, as well as from lower to higher C values (Figure 13 B). A higher density underlying dominant scattering

layer results in increases in the Mie scattering response, which decreases penetration depth and increases the σ° measurement. This is assumed to further reduce sensitivity to the overlying layer of snow accumulation, resulting in smaller freezing season σ° decreases. In general, the least accurate snow accumulation estimates are in the southwestern wet snow zone and the lower elevation southeastern percolation zone, which are characterized by higher snow accumulation rates and higher density underlying dominant scattering layers.

In regions assumed to have lower density underlying scattering layers, the spread in residual errors is concentrated within the tail of the comparison points, high $\Delta\sigma^\circ_{fs}$ versus moderate C values. Lower density underlying dominant scattering layers increase penetration depth, which subsequently decreases the Mie scattering response and decreases the σ° measurement. This is assumed to further increase sensitivity to the overlying layer of snow accumulation, resulting in larger freezing season σ° decreases. In general, the most accurate snow accumulation estimates are in the northeastern percolation, wet snow, and ablation zones and the higher elevation percolation zone which are characterized by lower snow accumulation rates and lower density underlying dominant scattering layers. It is observed that annually and interannually these generalized relationships vary, which is likely dependent on annual and interannual changes in snowpack stratigraphy. Time-varying changes in snowpack stratigraphy during the freezing season may be particularly significant to the scattering mechanism. To understand the complex relationship between freezing season backscatter signatures, snow accumulation rates, and snowpack stratigraphy in the underlying ice-facie, additional research is required.

While *Wismann et al.* [1997] and *Nghiem et al.* [2005] hypothesized the relationship between σ° and snow accumulation may be inverse and linear based on a simple backscatter model, an alternate geometric relationship is hypothesized between decreasing freezing season σ° signatures, snow accumulation rates, and snowpack stratigraphy in the underlying ice-facie which varies with time (*personal communication, Dr. Mark Drinkwater, Dr. David Long*).

A potential next step to a microwave snow accumulation metric is the delineation of ice-facie boundaries. The Greenland ice sheet is sensitive to the climate of the high-latitude Arctic region. Climatic change influences synoptic scale atmospheric circulations which control the spatiotemporal variability of snow accumulation rates, and surface melting which forms dominant scattering layers in each of the ice-facies. Ice-facie boundary shifts represent the large-scale response of the Greenland ice sheet to these changes. Distinct σ° signatures in each of the ice-facies were observed in this study, suggesting σ° measurements are sensitive to time-varying stratigraphic changes within the snowpack. This has previously been observed in Greenland ice sheet studies using both scatterometry [*Long and Drinkwater*, 1994] and SAR [*Fahnestock et al.*, 1993]. While several methods to delineate the dry snow line have been established using scatterometry [*Drinkwater et al.*, 2001b], an effective method to delineate the boundaries of the percolation, wet snow, and ablation zones currently remains undefined.

Of critical importance to surface mass balance studies is the position of the ELA, which separates the accumulation zone from the ablation zone, and the wet snow zone from the ablation zone. Upglacier boundary shifts in the ELA suggest mass gain, and downglacier boundary shifts suggest mass loss. Backscatter

measurements were observed to decrease transitioning between the lower boundary of the wet snow zone, which is characterized by a dominant scattering layer of superimposed ice, and the ablation zone, which is characterized by a dominant scattering layer of glacial ice with increased surface roughness. Decreases in the σ° measurement likely result from reflection the EM wave away from the scatterometers antenna in the ablation zone. A scatterometry derived ice-facie boundary delineation is potentially significant for surface mass balance studies, as well as in the context of the retrieval of an active snow accumulation metric.

To separate distinct microwave signatures and delineate ice-facie boundaries, as well as to delineate regions in each of the ice-facies that exhibit distinct microwave scattering characteristics, several methods are suggested: 1) a delineation using a basic clustering algorithm such as K-means, 2) a delineation using a statistical technique such as principle component analysis (PCA) or the similar Karhunen–Loève (KL) transform as recently suggested by [*Moon*, 2012], or 3) a more sophisticated technique such as the SAR algorithm outlined by [*Liu et al.*, 2005], modified for scatterometer data. Once delineation is achieved, the retrieval technique outlined in this thesis can be used to derive empirical relationships within each of the ice-facies.

A second potential next step is to derive an empirical relationship between radar backscatter and snow accumulation rates, which includes a metric for snowpack stratigraphy in the underlying ice-facie. Similar to the technique used to retrieve a microwave snow accumulation metric from observed decreasing freezing season σ° signatures, a metric for time-varying changes in the density of the underlying ice-facie can be retrieved from observed melt season step responses

suggested to represent the formation of dominant scattering layers. Larger step responses indicated a more significant change in snowpack stratigraphy.

Multiple frequency, multiple incidence angle retrievals acquired from satellite-borne scatterometers with overlapping orbital passes (e.g., Ku-band QuikSCAT, or the similar Ku-band OSCAT, and the C-band ASCAT) offer the potential to gain an increased understanding of the extinction coefficient, given differences in penetration depth associated with differences in wavelength, and differences in path length through the snowpack associated with differences in incidence angle.

A more sophisticated next step would be an approach similar to *Drinkwater et al.* [2001b]. This study derived and compared two relationships between radar backscatter and snow accumulation rates in the dry snow zone of the Greenland ice sheet: 1) an empirical relationship derived from comparisons between the change in σ° measurements with incidence angle and in situ snow accumulation rates ([*Drinkwater et al.,* 2001b], Figure 1D), and 2) a theoretical relationship derived from a coupled snow metamorphosis /backscatter model ([*Drinkwater et al.,* 2001b], Figure 3D).

Comparisons between the two previously described empirical relationships at Ku- and C- band, and a coupled snow metamorphosis/two layer backscatter model with variable parameters including, frequency and incidence angle, properties of the overlying snow layer (including snow grain sizes, densities, and layer thicknesses), and the density of the underlying dominant scattering layer (including orientation, sizes, and shapes of ice-scatterers) may yield further insight into the extinction

coefficient, and the relationship between freezing season backscatter decreases and snow accumulation rates within each of the ice-facies on the Greenland ice sheet.

REFERENCES

Abdalati, W., and K. Steffen (1997), Snowmelt on the Greenland ice sheet as derived from passive microwave satellite data, *Journal of Climate*, *10*(2), 165-175.

Abdalati, W., and K. Steffen (2001), Greenland ice sheet melt extent: 1979-1999, *Journal of Geophysical Research D: Atmospheres*, *106*(D24), 33983-33988.

Alley, R. B. (1988), Concerning the deposition and diagenesis of strata in polar firn, *Journal of Glaciology*, *34*(118), 283-290.

Alley, R. B., E. S. Saltzman, K. M. Cuffey, and J. J. Fitzpatrick (1990), Summertime formation of depth hoar in central Greenland, *Geophysical Research Letters*, *17*(13), 2393-2396.

Ashcraft, I., and D. G. Long (2006a), Comparison of methods for melt detection over Greenland using active and passive microwave measurements, *International Journal of Remote Sensing*, *27*(12), 2469-2488.

Ashcraft, I. S., and D. G. Long (2005), Observation and characterization of radar backscatter over Greenland, *IEEE Transactions on Geoscience and Remote Sensing*, *43*(2), 225-237.

Bales, R. C., J. R. McConnell, E. Mosley-Thompson, and B. Csatho (2001a), Accumulation over the Greenland ice sheet from historical and recent records, *Journal of Geophysical Research D: Atmospheres*, *106*(D24), 33813-33825.

Bales, R. C., J. R. McConnell, E. Mosley-Thompson, and G. Lamorey (2001b), Accumulation map for the Greenland Ice Sheet: 1971-1990, *Geophysical Research Letters*, *28*(15), 2967-2970.

Bales, R. C., Q. Guo, D. Shen, J. R. McConnell, G. Du, J. F. Burkhart, V. B. Spikes, E. Hanna, and J. Cappelen (2009), Annual accumulation for Greenland updated using ice core data developed during 2000-2006 and analysis of daily coastal meteorological data, *Journal of Geophysical Research D: Atmospheres*, *114*(6).

Benson, C. (1962), Stratigraphic Studies in the Snow and Firn of the Greenland Ice Sheet *Rep.*, 120 pp, Hanover, N. H.

Bhattacharya, I., K. C. Jezek, L. Wang, and H. Liu (2009), Surface melt area variability of the Greenland ice sheet: 1979-2008, *Geophysical Research Letters*, *36*(20).

Bindoff, N. L., et al. (2007), Observations: Oceanic Climate Change and Sea Level. In: Climate Change 2007: The Physical Science Basis. Contribution of Working Group I to the Fourth Assessment Report of the Intergovernmental Panel on Climate Change [Solomon, S., D. Qin, M. Manning, Z. Chen, M. Marquis,K.B. Averyt, M. Tignor and H.L. Miller (eds.)]. edited, Cambridge University Press, Cambridge, United Kingdom and New York, NY, USA.

Bingham, A. W., and M. R. Drinkwater (2000), Recent changes in the microwave scattering properties of the Antarctic ice sheet, *IEEE Transactions on Geoscience and Remote Sensing*, *38*(4 II), 1810-1820.

Box, J., L. Yang, J. Rogers, D. Bromwich, L. S. Bai, K. Steffen, J. Stroeve, and S. H. Wang (2005), Extreme precipitation events over Greenland: Consequences to ice sheet mass balance.

Box, J. E. (2005), Greenland ice sheet surface mass-balance variability: 1991-2003, *Annals of Glaciology*, *42*, 90-94.Box, J. E., D. H. Bromwich, and L. S. Bai (2004), Greenland ice sheet surface mass balance 1991-2000: Application of Polar MM5 mesoscale model and in situ data, *Journal of Geophysical Research D: Atmospheres*, *109*(16), D16105 16101-16121.

Box, J. E., D. H. Bromwich, B. A. Veenhuis, L. S. Bai, J. C. Stroeve, J. C. Rogers, K. Steffen, T. Haran, and S. H. Wang (2006), Greenland ice sheet surface mass balance variability (1988-2004) from calibrated polar MM5 output, *Journal of Climate*, *19*(12), 2783-2800.

Bromwich, D. H., Y. Li, Q. S. Chen, L. S. Bai, and E. N. Cassano (2001), Modeled precipitation variability over the Greenland ice sheet *Journal of Geophysical Research D: Atmospheres*, *106*(24), 33891-33908.

Burgess, E. W., R. R. Forster, J. E. Box, E. Mosley-Thompson, D. H. Bromwich, R. C. Bales, and L. C. Smith (2010), A spatially calibrated model of annual accumulation rate on the Greenland Ice Sheet (1958-2007), *Journal of Geophysical Research F: Earth Surface*, *115*(2).

Calanca, P., H. Gilgen, S. Ekholm, and A. Ohmura (2000), Gridded temperature and accumulation distributions for Greenland for use in cryospheric models, *Annals of Glaciology*, *31*, 118-121.

Cassano, J. J., J. E. Box, D. H. Bromwich, L. Li, and K. Steffen (2001), Evaluation of Polar MM5 simulations of Greenland's atmospheric circulation, *Journal of Geophysical Research D: Atmospheres*, *106*(D24), 33867-33889.

Chen, Q. S., D. H. Bromwich, and L. Bai (1997), Precipitation over Greenland retrieved by a dynamic method and its relation to cyclonic activity, *Journal of Climate*, *10*(5), 839-870.

Cogley, J. G. (2004), Greenland accumulation: An error model, *Journal of Geophysical Research D: Atmospheres*, *109*(18), D18101 18101-18115.

Cuffey, K. M., and W. S. B. Paterson (2010), The physics of glaciers. 4rd edition, *The physics of glaciers. 4rd edition*.

Dierking, W., S. Linow, and W. Rack (2012), Toward a robust retrieval of snow accumulation over the Antarctic ice sheet using satellite radar, *Journal of Geophysical Research D: Atmospheres*, *117*(9).

Drinkwater, M. R., and S. D. Argus (1989), LIMEX'87: international experiment in the Labrador Sea marginal ice zone, *Polar Record*, *25*(155), 335-342.

Drinkwater, M. R., and V. I. Lytle (1997), ERS-1 radar and field-observed characteristics of autumn freeze-up in the Weddell Sea, *Journal of Geophysical Research*, *102*(C6), 12593-12608.

Drinkwater, M. R., D. G. Long, and A. W. Bingham (2001), Greenland snow accumulation estimates from satellite radar scatterometer data, *Journal of Geophysical Research D: Atmospheres*, *106*(D24), 33935-33950.

Early, D. S., and D. G. Long (2001), Image reconstruction and enhanced resolution imaging from irregular samples, *IEEE Transactions on Geoscience and Remote Sensing*, *39*(2), 291-302.

Fahnestock, M., R. Bindschadler, R. Kwok, and K. Jezek (1993), Greenland ice sheet surface properties and ice dynamics from ERS-1 SAR imagery, *Science*, *262*(5139), 1530-1534.

Flach, D. J., K. C. Partington, C. Ruiz, E. Jeansou, and M. R. Drinkwater (2005), Inversion of the surface properties of ice sheets from satellite microwave data, *IEEE Transactions on Geoscience and Remote Sensing*, *43*(4), 743-752.

Forster, R. R., K. C. Jezek, J. Bolzan, F. Baumgartner, and S. P. Gogineni (1999), Relationships between radar backscatter and accumulation rates on the Greenland ice sheet, *International Journal of Remote Sensing*, *20*(15-16), 3131-3147.

Forster, R. R., D. G. Long, K. C. Jezek, S. D. Drobot, and M. R. Anderson (2001), The onset of Arctic sea-ice snowmelt as detected with passive- and active-microwave remote sensing, *Annals of Glaciology*, *33*, 85-93.

Hakuba, M. Z., D. Folini, M. Wild, and C. Schr (2012), Impact of Greenland's topographic height on precipitation and snow accumulation in idealized simulations, *Journal of Geophysical Research D: Atmospheres*, *117*(9).

Hall, D. K., S. V. Nghiem, C. B. Schaaf, N. E. DiGirolamo, and G. Neumann (2009), Evaluation of surface and near-surface melt characteristics on the Greenland ice sheet using MODIS and QuikSCAT data, *Journal of Geophysical Research F: Earth Surface*, *114*(4).

Hanna, E., P. Huybrechts, I. Janssens, J. Cappelen, K. Steffen, and A. Stenhens (2005), Runoff and mass balance of the Greenland ice sheet: 1958-2003, *Journal of Geophysical Research D: Atmospheres*, *110*(13).

Hicks, B. R., and D. G. Long (2010), Standard BYU QuikSCAT and SeaWInds Land /ICe Image Products*Rep.*, Brigham Young University Microwave Earth Remote Sensing Laboratory.

Hicks, B. R., and D. G. Long (2011), Inferring Greenland melt and refreeze severity from SeaWinds scatterometer data, *International Journal of Remote Sensing*, *32*(23), 8053-8080.

Howat, I. M., I. Joughin, and T. A. Scambos (2007), Rapid changes in ice discharge from Greenland outlet glaciers, *Science*, *315*(5818), 1559-1561.

Intergovernmental Panel on Climate Change (2007), Contribution of Working Group I to the Fourth Assessment Report of the Intergovernmental Panel on Climate Change, 2007 [Solomon, S., D. Qin, M. Manning, Z. Chen, M. Marquis,K.B. Averyt, M. Tignor and H.L. Miller (eds.)]. edited, Cambridge University Press, Cambridge, United Kingdom and New York, NY, USA.

Jezek, K. C., and P. Gogenini (1992), Microwave remote sensing of the Greenland ice sheet *Remote Sensing Society Newletter IEEE Transactions on Geoscience and Remote Sensing*(85), 6-10.

Jezek, K. C., P. Gogineni, and M. Shanableh (1994), Radar measurements of melt zones on the Greenland Ice Sheet, *Geophysical Research Letters*, *21*(1), 33-36.

Koch, J. P., and A. Wegener (1930), Wissenschaftliche Ergebnisse der da.nischen Expedition nach Dronning Louises-Land und quer uber das Inlandeis von Nordgronland 19 12- 13, *Medd. Gronl*, *75*.

Krabill, W., W. Abdalati, E. Frederick, S. Manizade, C. Martin, J. Sonntag, R. Swift, R. Thomas, W. Wright, and J. Yungel (2000), Greenland Ice Sheet: High-elevation balance and peripheral thinning, *Science*, *289*(5478), 428-430.

Kristjánsson, J. E., S. Thorsteinsson, and B. Røsting (2009), Phase-locking of a rapidly developing extratropical cyclone by Greenland's orography, *Quarterly Journal of the Royal Meteorological Society*, *135*(645), 1986-1998.

Kunz, L. B., and D. G. Long (2006), Melt detection in antarctic ice shelves using scatterometers and microwave radiometers, *IEEE Transactions on Geoscience and Remote Sensing*, *44*(9), 2461-2468.

Langway, C. C. (1961), Accumulation and temperature on the inland ice of northern Greenland, 1959 *Journal of Glaciology*, *3*, 1017-1044.

Liu, H., L. Wang, and K. C. Jezek (2005), Delineation of dry and melt snow zones in Antarctica using microwave remote sensing data, Seoul.

Long, D. G., and M. R. Drinkwater (1994), Greenland ice-sheet surface properties observed by the Seasat-A scatterometer at enhanced resolution, *Journal of Glaciology*, *40*(135), 213-230.

Long, D. G., J. Hardin, and T. Whiting (1993), Resolution enhancement of spaceborne scatterometer data, *IEEE Transactions on Geoscience and Remote Sensing*, *31*(3), 700-715.

Mätzler, C., and A. Wiesmann (1999), Extension of the microwave emission model of layered snowpacks to coarse-grained snow, *Remote Sensing of Environment*, *70*(3), 317-325.

Moon, K. R. (2012), Investigations of the dry snow zone of the Greenland ice sheet using QuikSCAT, Brigham Young University, Microwave Earth Remote Sensing (MERS) Lab.

Moore, G. W. K., and I. A. Renfrew (2005), Tip jets and barrier winds: A QuikSCAT climatology of high wind speed events around Greenland, *Journal of Climate*, *18*(18), 3713-3725.

Mosley-Thompson, E., J. R. McConnell, R. C. Bales, Z. Li, P. N. Lin, K. Steffen, L. G. Thompson, R. Edwards, and D. Bathke (2001), Local to regional-scale variability of annual net accumulation on the Greenland ice sheet from PARCA cores, *Journal of Geophysical Research D: Atmospheres*, *106*(D24), 33839-33851.

Munk, J., K. C. Jezek, R. R. Forster, and S. P. Gogineni (2003), An accumulation map for the Greenland dry-snow facies derived from spaceborne radar, *Journal of Geophysical Research D: Atmospheres*, *108*(9), ACL 8-1 ACL 8-12.

Murphy, B. F., I. Marsiat, and P. Valdes (2002), Atmospheric contributions to the surface mass balance of Greenland in the HadAM3 atmospheric model, *Journal of Geophysical Research D: Atmospheres*, *107*(21), XV-XVI.

Naderi, F. M., M. H. Freilich, and D. G. Long (1991), Spaceborne radar measurement of wind velocity over the ocean--An overview of the NSCAT scatterometer system, *Proceedings of the IEEE*, *79*(6), 850-866.

Nghiem, S. V., J. A. Kong, and R. T. Shin (1990a), Study of polarimetric response of sea ice with layered random medium model, Publ by IEEE, College Park, MD, USA.

Nghiem, S. V., M. Borgeaud, J. A. Kong, and R. T. Shin (1990b), Polarimetric remote sensing of geophysical media with layer random medium model, *Polarimetric remote sensing*, 1-73.

Nghiem, S. V., K. Steffen, R. Kwok, and W. Y. Tsai (2001), Detection of snowmelt regions on the Greenland ice sheet using diurnal backscatter change, *Journal of Glaciology*, *47*(159), 539-547.

Nghiem, S. V., K. Steffen, G. Neumann, and R. Huf (2005), Mapping of ice layer extent and snow accumulation in the percolation zone of the Greenland ice sheet, *Journal of Geophysical Research F: Earth Surface*, *110*(2).

Nghiem, S. V., D. K. Hall, T. L. Mote, M. Tedesco, M. R. Albert, K. Keegan, C. A. Shuman, N. E. DiGirolamo, and G. Neumann (2012), The extreme melt across the Greenland ice sheet in 2012, *Geophysical Research Letters*, *39*(20).

Ohmura, A., and N. Reeh (1991), New precipitation and accumulation maps for Greenland, *Journal of Glaciology*, *37*(125), 140-148.

Ohmura, A., M. Wild, and L. Bengtsson (1996), Present and future mass balance of the ice sheets simulated with GGM, *Annals of Glaciology*, *23*, 187-193.

Ohmura, A., P. Calanca, M. Wild, and M. Anklin (1999), Precipitation accumulation and mass balance of the Greenland Ice sheet, *Z. Gletscherkd. Glazialgeol.*, *35*(1), 1-20.

Oveisgharan, S., and H. A. Zebker (2007), Estimating snow accumulation from InSAR correlation observations, *IEEE Transactions on Geoscience and Remote Sensing*, *45*(1), 10-20.

Pfeffer, W. T., and N. F. Humphrey (1998), Formation of ice layers by infiltration and refreezing of meltwater, *Annals of Glaciology*, *26*, 83-91.

Pritchard, H. D., R. J. Arthern, D. G. Vaughan, and L. A. Edwards (2009), Extensive dynamic thinning on the margins of the Greenland and Antarctic ice sheets, *Nature*, *461*(7266), 971-975.

Rignot, E. (1995), Backscatter model for the unusual radar properties of the Greenland ice sheet, *Journal of Geophysical Research*, *100*(E5), 9389-9400.

Rignot, E., and P. Kanagaratnam (2006), Changes in the velocity structure of the Greenland Ice Sheet, *Science*, *311*(5763), 986-990.

Rignot, E., I. Velicogna, M. R. Van Den Broeke, A. Monaghan, and J. Lenaerts (2011), Acceleration of the contribution of the Greenland and Antarctic ice sheets to sea level rise, *Geophysical Research Letters*, *38*(5).

Rignot, E. J., S. J. Ostro, J. J. Van Zyl, and K. C. Jezek (1993), Unusual radar echoes from the Greenland ice sheet, *Science*, *261*(5129), 1710-1713.

Rotschky, G., W. Rack, W. Dierking, and H. Oerter (2006), Retrieving snowpack properties and accumulation estimates from a combination of SAR and a scatterometer measurements, *IEEE Transactions on Geoscience and Remote Sensing*, *44*(4), 943-955.

Rott, H., and K. Sturm (1991), Microwave signature measurements of Antarctic firn, Publ by IEEE, Espoo, Finl.

Sasgen, I., M. van den Broeke, J. L. Bamber, E. Rignot, L. S. Sørensen, B. Wouters, Z. Martinec, I. Velicogna, and S. B. Simonsen (2012), Timing and origin of recent regional ice-mass loss in Greenland, *Earth and Planetary Science Letters*, *333-334*, 293-303.

Scambos, T., R. Ross, R. Bauer, Y. Yermolin, P. Skvarca, D. Long, J. Bohlander, and T. Haran (2008), Calving and ice-shelf break-up processes investigated by proxy: Antarctic tabular iceberg evolution during northward drift, *Journal of Glaciology*, *54*(187), 579-591.

Scambos, T., H. A. Fricker, C. C. Liu, J. Bohlander, J. Fastook, A. Sargent, R. Massom, and A. M. Wu (2009), Ice shelf disintegration by plate bending and hydro-fracture: Satellite observations and model results of the 2008 Wilkins ice shelf break-ups, *Earth and Planetary Science Letters*, *280*(1-4), 51-60.

Schuenemann, K. C., and J. J. Cassano (2010), Changes in synoptic weather patterns and Greenland precipitation in the 20th and 21st centuries:1. Evaluation of late 20th century simulations from IPCC models, *Journal of Geophysical Research D: Atmospheres*, *114*(20).

Schuenemann, K. C., J. J. Cassano, and J. Finnis (2009), Synoptic forcing of precipitation over greenland: Climatology for 1961-99, *Journal of Hydrometeorology*, *10*(1), 60-78.

Serreze, M. C. (1995), Climatological aspects of cyclone development and decay in the arctic, *Atmosphere - Ocean*, *33*(1), 1-23.

Smith, L. C., Y. Sheng, R. R. Forster, K. Steffen, K. E. Frey, and D. E. Alsdorf (2003), Melting of small Arctic ice caps observed from ERS scatterometer time series, *Geophysical Research Letters*, *30*(20), CRY 2-1 - CRY 2-4.

Spencer, M. W., C. Wu, and D. G. Long (2000), Improved Resolution Backscatter Measurments with the SeaWinds Scatterometer *IEEE Transactions on Geoscience and Remote Sensing*, *38*(1), 89-104.

Steffen, K., and J. Box (2001), Surface climatology of the Greenland ice sheet: Greenland Climate Network 1995-1999, *Journal of Geophysical Research D: Atmospheres*, *106*(D24), 33951-33964.

Steffen, K., S. V. Nghiem, R. Huff, and G. Neumann (2004), The melt anomaly of 2002 on the Greenland Ice Sheet from active and passive microwave satellite observations, *Geophysical Research Letters*, *31*(20), L20402 20401-20405.

Stuart, K. M., and D. G. Long (2011), Tracking large tabular icebergs using the SeaWinds Ku-band microwave scatterometer, *Deep-Sea Research Part II: Topical Studies in Oceanography*, *58*(11-12), 1285-1300.

Swan, A. M., and D. G. Long (2012), Multiyear Arctic Sea Ice Classification Using QuikSCAT, *IEEE Transactions on Geoscience and Remote Sensing*.

Thomas, R., E. Frederick, W. Krabill, S. Manizade, and C. Martin (2006), Progressive increase in ice loss from Greenland, *Geophysical Research Letters*, *33*(10).

Thompson, S. L., and D. Pollard (1997), Greenland and Antarctic mass balances for present and doubled atmospheric CO 2 from the GENESIS version-2 global climate model, *Journal of Climate*, *10*(5), 871-900.

Tsukernik, M., D. N. Kindig, and M. C. Serreze (2007), Characteristics of winter cyclone activity in the northern North Atlantic: Insights from observations and regional modeling, *Journal of Geophysical Research D: Atmospheres*, *112*(3).

Ulaby, F. T., R. K. Moore, and A. K. Fung (1982), Microwave remote sensing: active and passive. Volume II. Radar remote sensing and surface scattering and emission theory, *Microwave remote sensing: active and passive. Volume II. Radar remote sensing and surface scattering and emission theory.*

van den Broeke, M., J. Bamber, J. Ettema, E. Rignot, E. Schrama, W. J. D. Van Berg, E. Van Meijgaard, I. Velicogna, and B. Wouters (2009), Partitioning recent Greenland mass loss, *Science*, *326*(5955), 984-986.

Van Der Veen, C. J., D. H. Bromwich, B. M. Csatho, and C. Kim (2001), Trend surface analysis of Greenland accumulation, *Journal of Geophysical Research D: Atmospheres*, *106*(D24), 33909-33918.

Vogelzang, J., and A. Stoffelen (2012), Scatterometer wind vector products for application in meteorology and oceanography, *Journal of Sea Research*.

Wang, L., M. Sharp, B. Rivard, and K. Steffen (2007), Melt season duration and ice layer formation on the Greenland ice sheet, 2000-fs2004, *Journal of Geophysical Research F: Earth Surface*, *112*(4).

Wang, W., J. Li, and H. J. Zwally (2012), Dynamic inland propagation of thinning due to ice loss at the margins of the Greenland ice sheet, *Journal of Glaciology*, *58*(210).

West, R. D., D. P. Winebrenner, L. Tsang, and H. Rott (1996), Microwave emission from density-stratified Antarctic firn at 6 cm wavelength, *Journal of Glaciology*, *42*(140), 63-76.

Wismann, V. (2000), Monitoring of seasonal snowmelt on Greenland with ERS scatterometer data, *IEEE Transactions on Geoscience and Remote Sensing*, *38*(4 II), 1821-1826.

Wismann, V., D. P. Winebrenner, K. Boehnke, and R. J. Arthern (1997), Snow accumulation on Greenland estimated from ERS scatterometer data, IEEE, Singapore, Singapore.

Zwally, H. J., M. B. Giovinetto, J. Li, H. G. Cornejo, M. A. Beckley, A. C. Brenner, J. L. Saba, and D. Yi (2005), Mass changes of the Greenland and Antarctic ice sheets and shelves and contributions to sea-level rise: 1992-2002, *Journal of Glaciology*, *51*(175), 509-527.

Zwally, H. J., et al. (2011), Greenland ice sheet mass balance: Distribution of increased mass loss with climate warming; 2003-07 versus 1992-2002, *Journal of Glaciology*, *57*(201), 88-102.